Development of a Thermoelectric Characterization Platform for Electrochemically Deposited Materials

Von der Fakultät Maschinenwesen

der Technischen Universität Dresden

zur Erlangung des akademischen Grades

Doktoringenieur
(Dr. -Ing.)

genehmigte
DISSERTATION

von
Vida Barati

eingereicht am: 10.06.2020
Disputation am: 03.12.2020
Erstgutachter: Prof. Dr. Kornelius Nielsch
Zweitgutachter: Prof. Dr. Alexander Eychmüller
Drittgutachter: Prof. Dr.-Ing. Michael Beitelschmidt
Fachbetreuerin: Dr. habil. Gabi Schierning

Druckjahr: 2020

To My Husband, Yousef, for his indefinite love, patience and support.

Juni 2020

Erklärung der Urheberschaft

Hiermit versichere ich, dass ich die vorliegende Arbeit ohne unzulässige Hilfe Dritter und ohne Benutzung anderer als der angegebenen Hilfsmittel angefertigt habe; die aus fremden Quellen direkt oder indirekt übernommenen Gedanken sind als solche kenntlich gemacht.

Weitere Personen waren an der geistigen Herstellung der vorliegenden Arbeit nicht beteiligt. Insbesondere habe ich nicht die Hilfe eines kommerziellen Promotionsberaters in Anspruch genommen. Dritte haben von mir keine geldwerten Leistungen für Arbeiten erhalten, die in Zusammenhang mit dem Inhalt der vorgelegten Dissertation stehen.

Die Arbeit wurde bisher weder im Inland noch im Ausland in gleicher oder ähnlicher Form einer anderen Prüfungsbehörde vorgelegt und ist auch noch nicht veröffentlicht worden.

Diese Promotionsordnung der Fakultät Maschinenwesen vom 1. Juli 2001 wird anerkannt.

Vida Barati

Contents

List of Figures

List of Tables

Acknowledgements

The path towards this thesis with all experiences has been followed by people who deserve a thank you.

My first thanks go to my supervisor, Prof. Dr. Kornelius Nielsch for his constant support and encouragement. I would like to sincerely thank my scientific adviser Dr. Gabi Schierning and her wonderful group members, Dr. Heiko Reith, Dr. Nicolas Perez and Dr. Ulrike Wolff for their guidance, support and patience. I'm specially indebted to Dr. Gabi Schierning who has given me the chance to join the thermoelectric group and encouraged me in any stage of my PhD. I am also grateful to Dr. Javier Garcia Fernandez and Dr. Heiko Reith for allotting the time to guide me and help me whenever I needed with their constructive discussions and exchange of experiences. I would like to express my sincere gratitude to my PhD committee, Prof. Dr. Kornelius Nielsch, Prof. Dr. Alexander Eychmüller and Prof. Dr.-Ing. Michael Beitelschmidt for devoting the time to review my PhD thesis and for their invaluable feedback.

I also thank all members of PD Dr. Andy Thomas's group for their helpful and friendly collaboration, especially Kevin Geichendorf for his smart advises and support regarding measurement setup and Michaela Lammel who has synthesized the passivation layer with atomic layer deposition. I also thank Lennart Wilkens, Alexander Kunzmann and Alejandra Ruiz de Clavijo for their cooperative teamwork and collaborations they made to my work.

I also want to thank my groupmates and colleagues in thermoelectric group and at IFW institute who have created a delightful and vibrant environment to collaborate. David Alberto Lara Ramos, Aditya Dutt, Daniel Dzekan, Samaneh Bayesteh, Lauritz Schnatmann, Constantin Wolf, Dietmar Berger and other wonderful colleagues who cannot be listed in one paragraph. I am grateful to Heidrun Stein, Ronald Uhlemann and Tom Sieger for their technical support.

I acknowledge the financial support from the European Union (EU) and the Free State of Saxony through the European Regional Development Fund (ERDF) (SAB GroTEGx, grant no. 100245375).

I am also thankful to Ziba Zanganeh, Alaleh Mirhajivarzaneh, Fatemeh Rajabasadi and Monica Fernandez Barcia for the funny and unforgettable time during coffee breaks and lunch time.

Very special thanks belong to my parents, Pouran and Bahman for supporting and motivating me in my endeavour, my lovely sister Diba and funny brother Pouria and of course my extended family, Mahnaz, Zahra, Younes and Mostafa. Thank you all for your patience and support throughout this journey.

Finally, I would like to thank my husband Yousef, best friend and companion, who has not only helped me to get a better understanding of the physical concepts but encouraged and pushed me whenever I needed in each step of my PhD. Thank you for standing patiently by my side and providing me with best conditions so that I could fulfill my dreams and finish my PhD journey which was not possible without your support.

Abstract

In this thesis, I developed a transport device for a full zT characterization of micro-scaled thermoelectric materials synthesized by the electrochemical deposition technique. The device enables the simultaneous determination of the in-plane electrical conductivity, Seebeck coefficient and thermal conductivity whilst removing the impact of the seed layer as well as the substrate.

To prepare the device, I applied a combination of photolithography and micro-structuring techniques along with etching processes. These techniques provided a suspended thermoelectric material on a free-standing membrane.

A characterization procedure was presented for the transport device to determine thermoelectric properties. Each single transport parameter was measured under a defined configuration setup and dedicated boundary conditions. Temperatures were measured using resistance thermometers located on the membrane. For thermal conductivity measurement, I applied a one-dimensional analytical steady-state method to evaluate the temperature distribution along the sample which was confirmed using three-dimensional finite element simulations. In addition, the simulations provided information about the accuracy of the measurement as well as parasitic heat losses dissipated through resistance thermometers.

To validate the transport device, I showed the temperature dependent thermoelectric properties of $Co_{75}Ni_{25}$ as n-type and Sb as p-type thick films within the developed transport device. The measured properties of the thick films were compared with those obtained for bulk samples and thin films. Hereby, the validity of the developed transport device could be demonstrated.

Finally, I investigated the impact of the geometry on the performance of an electrochemically fabricated micro-thermoelectric generator using finite element simulation. In the course of the geometry optimization of the device, the impact of the dimension and the packing density of thermoelectric elements on the performance of the generator was studied by analyzing the interplay of its electrical and thermal fluxes.

Zusammenfassung

In dieser Dissertation habe ich ein Transport-Device für eine vollständige zT Charakterisierung von mikro-skaligen thermoelektrischen Materialien entwickelt, welche durch elektrochemische Abscheidungstechnik synthetisiert wurden. Das Device ermöglicht die gleichzeitige Bestimmung der elektrischen Leitfähigkeit, des Seebeck Koeffizienten, und der Wärmeleitfähigkeit in der Ebene, während der Einfluss der zur Herstellung benötigten elektrisch leitenden Schicht, sowie des Substrats beseitigt werden.

Zur Fertigungs des Devices habe ich eine Kombination von Fotolithografie und Mikro-Strukturierungstechniken zusammen mit Ätzprozessen angewendet. Dadurch ist es möglich ein auf einer freistehenden Membran suspendiertes thermoelektrisches Material zu erhalten.

Für das Tranport-Device wurde ein Charakterisierungsverfahen zur Bestimmung der thermoelektrischen Eigenschaften von elektrochemisch abgeschiedenen Materialien entwickelt. Jeder einzelne Transportparameter wurde unter einem definierten Konfigurations-Setup und speziellen Randbedingungen gemessen. Temperaturen wurden durch die Verwendung von Widerstandsthermometern gemessen, welche sich auf der Membran befanden. Für die Messung der Wärmeleitfähigkeit habe ich eine eindimensionale, analytische, stationäre Methode eingesetzt, um die Temperaturverteilung entlang der Probe auszuwerten. Diese Methode wurde mit Hilfe von dreidimensionalen Finite-Elemente Simulationen bestätigt. Darüber hinaus lieferten die Simulationen Informationen über die Genauigkeit der Messungen, sowie über parasitäre Wärmeverluste, die an den Widerstandsthermometern auftreten.

Zur Validierung des Transport-Devices habe ich die temperaturabhängigen thermoelektrischen Eigenschaften von Dickfilmen, $Co_{75}Ni_{25}$ als n-Typ und Sb als p-Typ, mit Hilfe des entwickelten Devices gemessen. Die gemessenen Eigenschaften der Dickfilme wurden mit denen verglichen, welche für Bulk-Proben und Dünnfilme erhalten wurden. Auf diese Weise konnte die Validität des Transport-Devices nachgewiesen werden.

Abschließend habe ich den Einfluss der Geometrie auf die Leistung eines elektrochemisch hergestellten mikro-thermoelektrischen Generators mit Hilfe einer Finite-Elemente Simulation untersucht. Im Rahmen der Geometrieoptimierung des Devices wurde der Einfluss der Dimension und der Packungsdichte von thermoelektrischen Elementen auf die Leistung des Generators durch die Analyse der Wechselwirkung von elektrischen und thermischen Flüssen im Device untersucht.

1. Introduction

1.1. Motivation

Thermoelectricity describes the interaction between heat flux and electricity which can be operated either in the way a temperature gradient generates electricity known as power generator or in the reverse way where an electrical current provides Peltier heating and cooling [1–5]. Thermoelectricity may be applied for developing sustainable and green energy recovery and utilization. Micro thermoelectric devices (µTEDs) hold a tremendous potential as highly accurate and responsive means in a range of applications, including, thermal management [6, 7], biomedical devices [8–10], cooling of power electronics [11, 12], the internet of Things devices [13] and body powered wearable electronics [14, 15]. Due to their characteristic short lengths and small cross-sections, these µTEDs as opposed to large generators or coolers can be integrated into electronic devices enabling specific advantages namely good reliability, fast response time and light body weight [16, 17]. Furthermore, they can generates electricity using a tiny temperature gradient like human body temperature while handling heat fluxes up to several hundred $\mathrm{W\,cm^{-3}}$ [18, 19]. Compared with nano-scaled thermoelectric devices, µTEDs are of interest due to the low electrical resistance as well as high attainable densities of heat flux and cooling power [12].

Many researches have been devoted to determine the figure of merit zT as an essential performance-related quantity which is defined by Seebeck coefficient, electrical conductivity and thermal conductivity. This has led to the development of new and challenging characterization techniques [20–25]. The optimization of the performance of thermoelectric (TE) materials, however, has been one of the challenges when seeking for high efficient TE materials with micro-and nano-scaled geometry. This especially counts for thick films which are synthesized by electrochemical deposition (ECD) technique. ECD technique refers to the form of fabrication route for applications of µTEDs which has a number of advantages compared to other deposition technologies such as sputtering, evaporation or chemical vapor deposition. This technique is cost-effective, highly scalable, it does not need vacuum technique and is compatible with micro-electromechanical system (MEMS) and complementary metal-oxide semiconductor (CMOS) back-end technology [26].

Nonetheless, characterization of TE thick films prepared using ECD technique has always been a challenge due to the existence of an electrically conductive seed layer. In ECD technique, the desired thick film is deposited onto an electrically conductive seed layer which causes a short circuit to the in-plane electrical field. This makes the unambiguous characterization of the material difficult to achieve.

To determine the zT value, there exist various types of characterization methods applied for nano- and micro-scaled films experimentally. One of the common approaches is to measure the single transport coefficients in a separate setup which is usually performed using different samples [27, 28]. Only few approaches enable the simultaneous characterization of the transport coefficients on a single sample [20–22]. The Harman method, for instance allows a convenient way to achieve the cross-plane zT values of thin films [23–25]. In this method, zT is measured as the ratio of Seebeck voltage and electrical Joule voltage by applying a current to the TE sample. An applied current generates a temperature gradient through the sample which is due to the Joule and Peltier effects. Consequently, the total voltage consists of electrical voltage of Ohm 's law and Seebeck voltage. The electrical voltage vanishes instantaneously by terminating the current, while the Seebeck voltage decreases slowly due to heat dissipation and capacity of TE material [23, 25]. However, this method does not enable independent measurement of each single transport property.

Another full zT characterization of nano-scaled film was presented by Linseis *et al* [22, 29]. They have shown how to obtain a full in-plane characterization of thin film deposited on a pre-structured measurement platform. The platform combines two suspended Si_3N_4 membranes according to Völklein geometry [21, 30] for in-plane thermal conductivity with a Van-der-Pauw structure for electrical conductivity measurement [22]. However, the platform does not enable the characterization of electrochemically deposited films since it is not possible to remove the electrically conductive seed layer.

In this work, I present the development of a transport device based on an array of photolithography and micro-structuring in combination with etching processes. This device enables full in-plane zT characterizations of electrochmically deposited TE thick films, whilst eliminating the influence of the substrate and the seed layer. Hence, the conceptual approach to develop the transport device is focusing on two aims: first, removing the impact of the substrate as well as the electrically conductive seed layer. Second, simultaneous characterizations of transport properties, including, Seebeck coefficient, electrical and thermal conductivity on one single sample.

Beside of the optimization of micro-TE materials characterized within the transport device, the performance of µTEDs is significantly influenced by the design, geometry and construction factors. Therefore a short chapter of the thesis is devoted to the geometry optimization of a micro-TE generator.

In the following section, I give readers an overview of the contents and organizations of each chapter of the present thesis.

1.2. Outline of the Thesis

The outline of the present thesis includes seven chapters which are shortly described in the following.

Chapter 2 - State of the Art

This chapter is devoted to the basic principle and concept of thermoelectricity and three particular TE phenomena in solids. Further, the performance of TE materials along with its main characteristic properties are explained. The structure of a TEG and its corresponding performance parameters are also described. An overview of TE materials with a short definition of materials with high thermopower used within this work are as well addressed in this chapter.

Chapter 3 - Experiments and Methods

In this chapter, the treatments and techniques applied to develop and fabricate the transport device are introduced. These treatments include photolithography and microstructuring, different kind of deposition techniques and etching processes. The electrochemical deposition technique is discussed in more detail as the major synthesis for TE material thick film being characterized using the transport device. Besides, the preparation of bulk samples and thin films are addressed which were used as reference samples. Moreover, a short description of the measurement system used in this work as well as three-dimensional (3D) finite element simulation are introduced.

Chapter 4 - Fabrication of the Transport Device

This chapter is dedicated to the fabrication line and processing steps of the transport device starting from conceptual approach up to the characterization procedure using the transport device. The characterization procedure contains the applied configuration setup and its corresponding boundary conditions for each single parameter.

Chapter 5 - Validation of the Transport Device

This chapter concerns the 3D simulation of the transport device using Comsol Multiphysics. Two aims are pursued in this chapter: first, the validity of the one-dimensional (1D) analytical approach used for thermal conductivity measurement is presented using 3D simulation. For this aim the temperature distribution along the sample was studied. Second, the accuracy of the measurements achieved with the transport device and parasitic heat losses are discussed in more details. This helps to identify the range of thicknesses and thermal conductivities of materials to be characterized with the transport device.

Chapter 6 - Thermoelectric Characterization using Transport Device

This chapter shows the results of the temperature dependent TE properties of $Co_{75}Ni_{25}$ as n-type and Sb as p-type with the developed transport device. To show the validity of the transport device, the results are compared with those obtained for bulk reference samples and thin films. Besides, the synthesis of these two TE thick films along with their corresponding deposition parameters are explained in this chapter.

Chapter 7 - Optimization of µTEG

In this chapter the geometry optimization of a micro-TE generator is addressed by studying the impact of the dimension and the packing density of TE elements and analyzing the interplay of electrical and thermal fluxes of the generator.

Chapter 8 - Summary and Conclusion

In this chapter, the main results and conclusions are summarized.

2. State of the Art

Regarding the focus of this work on TE characterization, I start with a brief overview of thermoelectricity and its main effects then specify the organization of the chapter. Thermoelectricity is a direct energy-conversion between heat fluxes and electricity. The conversion of heat flux into electricity is called Seebeck effect which was first discovered in 1821 by T. J. Seebeck [1, 3, 4, 31]. He discovered that a compass needle would be deflected in a circuit built by two dissimilar metals when a temperature gradient is applied at their junction. He found that an electromotive force could be induced by a temperature gradient between two dissimilar conductors. Peltier effect is the opposite phenomenon of Seebeck effect which was observed thirteen years after the discovery of Seebeck effect by J. Peltier [1, 3, 31]. He showed that an electric current passing through a thermocouple can create a small heating or cooling effect.

The third TE effect known as Thomson effect describes the heating or cooling in the presence of current as well as temperature gradient in a conductor. This phenomenon was found in 1855 by W. Thomson. He established a relationship between Seebeck and Peltier effects by applying the theory of thermodynamics which is known as Kelvin relation [1].

The outline of this chapter is as follows. First in section 2.1, a short description of the thermoelectricity is discussed which was nicely derived by Onsager on the framework of the thermodynamics of the coupled mechanisms involved in this process. Then, a short review of the TE phenomena in solids is given in section 2.2. The three main TE effects and their relations are discussed in this section. Section 2.3 is devoted to the performance of TE materials and its according most important characteristic parameters are explained in this section. The structure of a TEG and its performance parameters are discussed in section 2.4. Section 2.5 is assigned to the definition and a classification of TE materials with an insight into materials with high power factor and high thermal conductivity which were used in this work.

2.1. Application of Onsager Relation to Thermoelectricity

In this section, the basic formulation of the Onsager-Callen theory for transport processes occurring near equilibrium is described. This theory is defined in the thermodynamic framework and expresses the mutual interference of two or more irreversible transport processes (like heat conduction, electrical conduction and diffusion) when they take place simultaneously in a thermodynamic system[31–34]. Each individual transport process is defined by a linear relation between the flux (J) and its corresponding force (X). Hence, for two or more coupled transport processes, the relationship between fluxes $\overrightarrow{J_i}$ and generalized forces $\overrightarrow{X_j}$ is as follows:

$$\overrightarrow{J_i} = \sum_j L_{ij} \overrightarrow{X_j}. \tag{2.1}$$

This relation is referred to as phenomenological coupled transport equation or linear response equation. L_{ij} denote transport coefficients or Onsager coefficients which can be related to the properties of the system such as electrical, thermal conductivity and etc. The L_{ij} is a measure of the interplay between jth and ith processes. In the case of $L_{ij} = 0$ for all $i \neq j$, each flux would only depend on its corresponding force which indicates no coupling between various processes. Considering a small deviation near equilibrium, Onsager reciprocal relations state that [34]:

$$L_{ij} = L_{ji}. \tag{2.2}$$

On the basis of these Onsager relations, TE effects have been described as the result of the carriers flux $\overrightarrow{J_N}$ and the heat flux $\overrightarrow{J_Q}$ in a system which are linked together through the conservation of the energy expression[34],

$$\overrightarrow{J_E} = \overrightarrow{J_Q} + \overline{\mu}_e \overrightarrow{J_N}, \tag{2.3}$$

where $\overrightarrow{J_E}$ is the energy flux and $\overline{\mu}_e$ is the electrochemical potential described as follows

$$\overline{\mu}_e = \overline{\mu}_c + |e|V. \tag{2.4}$$

In Eq. 2.4 $\overline{\mu}_c$ is the chemical potential, e is the elementary charge and V is the externally applied voltage [34]. Using the linear Onsager set of equations, the transport of carriers

and heat is then given by [34]:

$$\begin{bmatrix} \overrightarrow{J}_N \\ \overrightarrow{J}_Q \end{bmatrix} = \begin{bmatrix} L_{11} & L_{12} \\ L_{21} & L_{22} \end{bmatrix} \begin{bmatrix} -\frac{1}{T}\overrightarrow{\nabla}\mu_e \\ \overrightarrow{\nabla}(\frac{1}{T}) \end{bmatrix}, \tag{2.5}$$

where $-\frac{1}{T}\overrightarrow{\nabla}\mu_e$ and $\overrightarrow{\nabla}(\frac{1}{T})$ with T being the absolute temperature are thermodynamic forces (acting as generalized forces or affinities) for carriers and heat, respectively.

The transport coefficients L_{11}, $L_{12} = L_{21}$ and L_{22} in Eq. 2.5 are interrelated with each other and depend on T and the TE properties [34]

$$L_{11} = \frac{T}{e^2}\sigma, \tag{2.6}$$

$$L_{12} = \frac{T^2}{e^2}\sigma S, \tag{2.7}$$

$$L_{22} = \frac{T^3}{e^2}\sigma S^2 + T^2\lambda_e, \tag{2.8}$$

$$L_{21} = L_{12}, \tag{2.9}$$

where σ denotes the isothermal electrical conductivity and λ_e is the thermal conductivity under zero carrier transport. $S = e\alpha$ refers to the entropy per carrier where α is the Seebeck coefficient. The present description of the thermal conductivity does not involve the lattice contribution (phonons) of the TE materials but only the electronic contribution. This is because of the Onsager description which follows the linear response theory. The lattice contribution may be added to the transport coefficient L_{22} term as a lattice thermal conductivity λ_l. Hence the thermal conductivity in the absence of carrier transport is $\lambda = \lambda_e + \lambda_l$. Substituting these four transport coefficients in Eq. 2.5, one can obtain the coupled Onsager expressions [34]:

$$\overrightarrow{J} = \sigma\overrightarrow{E} - \alpha\sigma\overrightarrow{\nabla}(T), \tag{2.10}$$

$$\overrightarrow{J_Q} = T\alpha\overrightarrow{J} - \lambda\overrightarrow{\nabla}(T), \tag{2.11}$$

where

$$\overrightarrow{E} = -\frac{\overrightarrow{\nabla}(\overline{\mu}_e)}{e}, \tag{2.12}$$

$$\overrightarrow{J} = e\overrightarrow{J_N}, \tag{2.13}$$

are the electric filed and the electric current density, respectively. The two terms of $\overrightarrow{J_Q}$ in Eq. 2.11 are the Peltier proportional to $\overrightarrow{J}$ and the conductive terms proportional to $\overrightarrow{\nabla}(T)$, respectively. Using Eq. 2.12, Eq. 2.13 and energy and carriers conservation equations ($\overrightarrow{\nabla}.\overrightarrow{J_E} = 0, \overrightarrow{\nabla}.\overrightarrow{J_N} = 0$), Eq. 2.3 can be written as follows [34]

$$\overrightarrow{\nabla}.\overrightarrow{J_Q} + \overrightarrow{E}.\overrightarrow{J} = 0. \tag{2.14}$$

Within the framework of a 1D model and solving Eq. 2.14 by taking into account boundary conditions for one single TE leg of length of $L(0 \leq x \leq L)$ and a cross section of A, the temperature gradient $\overrightarrow{\nabla}(T)$ at both sides of a TE element is given by

$$\left(\frac{dT}{dx}\right)_{x=0} = \frac{T_c - T_h}{L} + \frac{J^2 L}{2\sigma\lambda} \qquad \left(\frac{dT}{dx}\right)_{x=L} = \frac{T_c - T_h}{L} - \frac{J^2 L}{2\sigma\lambda}, \tag{2.15}$$

where $T(0) = T_h$ is the temperature of the hot side and $T(L) = T_c$ is the temperature of the cold side for a TEG. For one single leg of a TEG, the heat fluxes at the hot $J_Q(0)$ and the cold side $J_Q(L)$ are given as follows [34]

$$J_Q(0) - \alpha T_h J = -\lambda \frac{T_c - T_h}{L} - J^2 \frac{L}{2\sigma}, \tag{2.16}$$

$$J_Q(L) - \alpha T_c J = -\lambda \frac{T_c - T_h}{L} + J^2 \frac{L}{2\sigma}. \tag{2.17}$$

These two above equations can be presented with global values, the electric current $I = JA$, the thermal conductance $K = \dfrac{\lambda A}{L}$, the resistance $R = \dfrac{L}{\sigma A}$ and the heat power $\dot{Q}_h = AJ_Q(0)(\dot{Q}_c = AJ_Q(L))$ at the hot side (cold side) [34].

$$\dot{Q}_h = \alpha T_h I - \frac{1}{2} I^2 R + K(T_h - T_c), \tag{2.18}$$

$$\dot{Q}_c = \alpha T_c I + \frac{1}{2} I^2 R + K(T_h - T_c). \tag{2.19}$$

In Eq. 2.18 and Eq. 2.19, the first term represents the Peltier heat, the second term is the Joule heating dissipated from the TE leg due to the electrical current and the third term is due to the Fourier heat conduction flowing away from the hot side to the cold one. Subscripts h and c stand for the hot and cold side of the TE leg. In section 2.4, the structure and the performance of a TEG is explained using the above equations and the

produced electrical power. In the following sections σ , α and λ are described in more details.

2.2. Thermoelectric Phenomena

Charge carriers in solids play the main role in thermoelectricity because they possess different energies in different materials and can carry electrical current as well as heat. They flow from hot side to cold side by an applied temperature difference giving rise to an electric voltage. Likewise, the energy of electrons is changed by passing a current through a material which leads to the appearance of heating or cooling at the junction. This indicates a coupling between electrical and thermal properties of a material. There are three kinds of TE effects, the Seebeck effect, the Peltier effect and the Thomson effect [1, 3, 35].

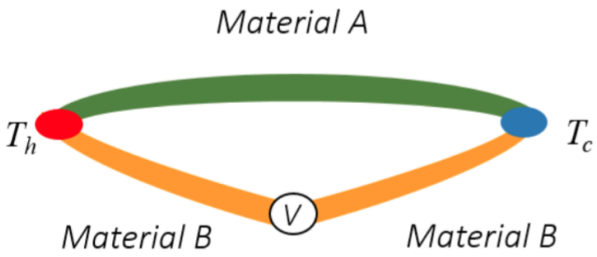

Figure 2.1.: A simple thermocouple built of two different materials shows the Seebeck effect.

In this section, the Seebeck and Peltier effects are defined and it is described how they depend on one another. The Seebeck effect describes how an electric voltage can be induced when a temperature difference is applied to a junction of two dissimilar conductors as shown in Fig. 2.1 [1]. By applying a temperature difference between two junctions, the charge carriers diffuse from the hot side to the cold side and accumulate in the cold region. The electric field is developed between the hot and the cold side which prevents the further diffusion of charge carriers. This phenomenon is known as Seebeck effect which is the principle of the TE power generation [1, 35]. The voltage induced V by temperature difference between the free ends is defined as

$$V = \alpha_{AB}(T_h - T_c), \tag{2.20}$$

where $\Delta T = T_h - T_c$ is the temperature difference between the hot side T_h and the cold one T_c. The magnitude of the induced voltage is dependent on ΔT between the junctions [1, 35, 36].

The Peltier effect is an opposite process of the Seebeck effect [1, 35, 36]. It is described as the induced heating or cooling at the junction of two conductors or semiconductors when passing a current through the junction. The heat induced by Peltier effect can be expressed as

$$\dot{Q}_{Peltier} = \Pi_{AB} I, \tag{2.21}$$

where Π_{AB} is the Peltier coefficient and I is the applied current. The heat dissipated or absorbed depends on the direction of the applied current. Kelvin equation describes the relationship between the Peltier and the Seebeck coefficient

$$\Pi_{AB} = \alpha_{AB} T. \tag{2.22}$$

The other Kelvin equation expresses α_{AB} in terms of Thomson coefficient τ_{AB} [1, 3]. The relevant equation is

$$\tau_A - \tau_B = T \frac{d\alpha_{AB}}{dT}. \tag{2.23}$$

Thomson effect is defined as the heat dissipation or absorption when an electric current flows through a conductor which is exposed to a temperature difference [1, 3]. The heat power related to the Thomson effect can be described as [1]

$$\dot{Q}_t = \tau I \frac{dT}{dx}. \tag{2.24}$$

In addition to the described effects, the Joule heating known as resistive heating is also generated in materials of non-zero resistance due to interactions between charge carriers and causes a reduction of performance of TE generators and coolers. This kind of heat is not generally termed as TE effect. This phenomenon is not reversible in contrast to the TE effects [1].

Since discovery of the TE effects, many materials have been considered to be used in power generators or Peltier coolers. Optimizing the performance of these materials is vital for unlocking their potential use in a board range of applications. The performance of TE materials can be determined by figure of merit z defined by three main transport coefficients, including, Seebeck coefficient, electrical and thermal conductivity. These three components and their effects on the value of z will be discussed and analyzed qualitatively in the following sections.

2.3. Performance of Thermoelectric Material

To obtain an efficient and economical TE device, we need to maximize its performance. The performance or efficiency of TE devices depends on their construction as well as properties of TE materials. The efficiency was mathematically defined by Edmund Altenkirch who expressed this parameter in proportional to physical properties of TE materials in a simplified thermopile. Later, Abram F. Ioffe, has introduced a new parameter, z called figure of merit, to calculate the efficiency of TE materials [37, 38]. z is considered as the most important characteristic of the TE material and expresses the relationship between α, σ and λ given by [35, 36, 38–41]

$$z = \frac{\alpha^2 \sigma}{\lambda}. \tag{2.25}$$

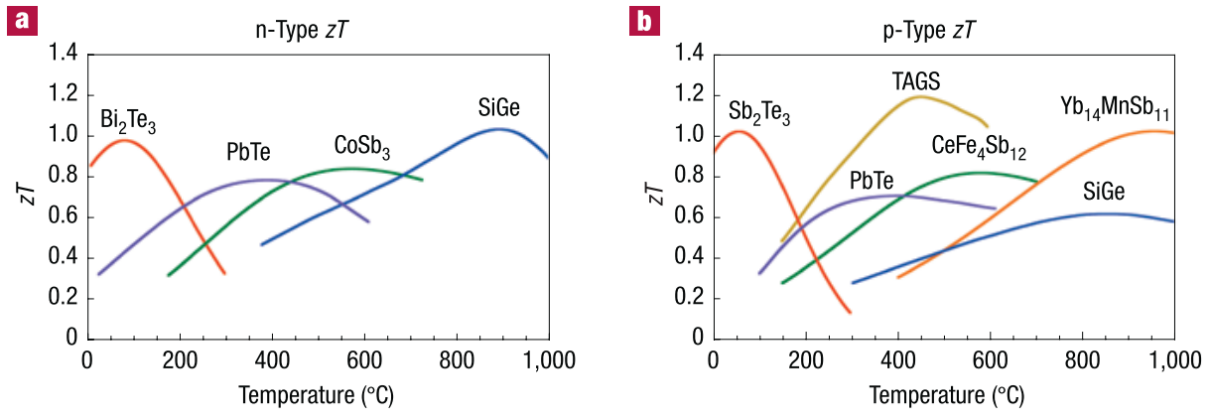

Figure 2.2.: Thermoelectric figure of merit zT of some commercial TE materials (a) n-type and (b) p-type [35], the state of the art of 2008.

In above equation λ includes the electronic λ_e and lattice λ_l contribution (see section 2.3.3). Since the three transport properties depend on the temperature of a material, z is consequently a function of temperature. In studies, people normally use z multiplied by temperature. zT is a dimensionless parameter. This parameter as a function of temperature for a range of commercial materials (a) n-type and (b) p-type is shown in Fig. 2.2 some of which are explained in more details in section 2.5. z can be maximized by high α, high σ and low λ. These three transport parameters are dependent on carrier concentrations and their combination should be good enough to obtain a reasonable efficiency. This will be more discussed in the following sections. Finding TE materials which possess a good combination of these parameters has always been a great challenge in the field of

thermoelectricity [35]. Introduction of semiconductors in 1950s led to the development of TE generators or coolers with high performance for space missions utilization [1].

2.3.1. Thermopower

Thermopower or Seebeck coefficient is defined as the ratio between electrochemical gradient and the temperature gradient or in a simple word it is the entropy transported by charge carriers divided by their charge, therefore the thermopower is expressed as follows [34]

$$-\frac{1}{e}\overrightarrow{\nabla}\mu_e = \alpha\overrightarrow{\nabla}T = \overrightarrow{E}. \tag{2.26}$$

For metals, α is defined as the product of the electronic specific heat C and the temperature T divided by the number of carriers N as follows [39]

$$\alpha \approx \frac{CT}{N} \approx \left(\frac{k_B}{e}\right)\frac{k_B T}{E_F}, \tag{2.27}$$

where k_B denotes the Boltzmann constant $1.38 \times 10^{-23}\mathrm{JK}^{-1}$ and E_F denotes the Fermi energy. This shows that metals possess α less than $k_B/e \approx 87\,\mu\mathrm{V\,K}^{-1}$ and decreases with decreasing temperature where k_B/e is the Seebeck of a classical electron gas and $E_F \gg k_B T$ [39].

In semiconductors with an energy band gap of E_G, α is given by [39]

$$\alpha \approx \left(\frac{k_B}{e}\right)\frac{E_G}{k_B T}, \tag{2.28}$$

which shows that α is larger than the one of the classical electron gas ($87\,\mu\mathrm{V\,K}^{-1}$) and increases with decreasing temperature. Since there are n-type and p-type charge carriers which lead to n- and p-conduction, α depends on the carrier concentration as well as the type of carriers. For a conductor which is composed of an equal number of n- and p-charge carriers, Seebeck voltage is not induced because charge carriers of n and p cancel out each other. α is negative when electrons are the majority of charge carriers while it is positive when the number of holes as charge carriers dominates. The dependency of α on carrier concentration can be seen from relatively simple models of electron transport [35] of metals and semiconductor with parabolic bands given by [35]

$$\alpha = \frac{8\pi^2 k_B^2}{3eh^2} m^* T \left(\frac{\pi}{3n}\right)^{2/3}, \tag{2.29}$$

where n is the density of charge carriers and m^* is the effective mass of the carrier. n as the main transport mechanism affects transport properties involved in zT [35]. Fig 2.3 shows the inversely proportionality of α to the number of charge carriers [35].

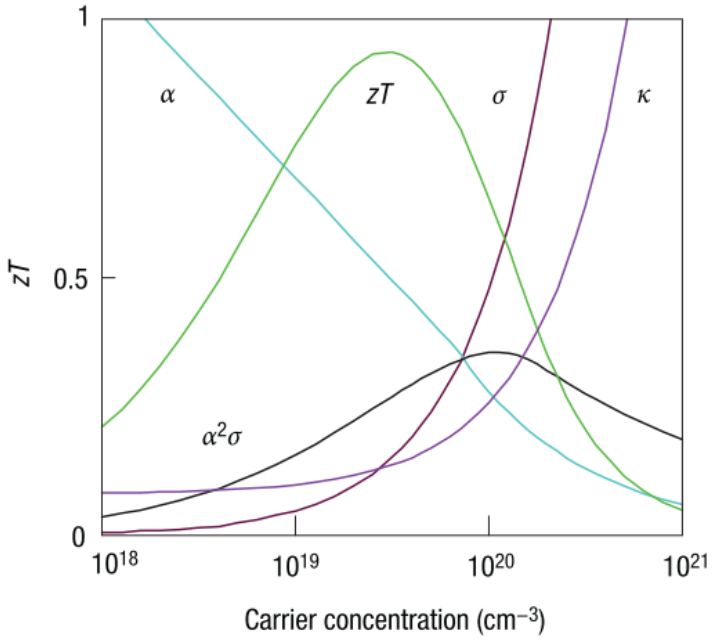

Figure 2.3.: Seebeck coefficient, electrical conductivity, thermal conductivity and figure of merit vs carrier concentration [35].

2.3.2. Electrical Conductivity

As discussed in section 2.3, the value of zT can be increased by increasing σ which is defined as the ability to move charge carriers through a material. σ is proportional to the density of charge carriers and their mobility μ which can be defined as follows

$$\sigma = n\mu e, \tag{2.30}$$

where μ is

$$\mu = \frac{e\tau_m}{m^*}. \tag{2.31}$$

μ is proportional to the mean scattering time between collisions of carriers τ_m and reversely proportional to m^*. According to equation (2.29), insulators and even semiconductors with a low carrier concentration and a high effective mass have a large α despite their small σ. The compromise between α and σ is shown in Fig 2.3 where it is shown that metals due to their high carrier concentrations of typically $n \approx 10^{22}$ cm^{-3} [36] have relatively small α and large σ.

For semiconductors the conduction can be induced by thermal excitation of charge carriers across the band gap [39].

$$\sigma \approx \sigma_0 exp\left(-\frac{E_G}{2k_BT}\right). \tag{2.32}$$

As there are two kinds of charge carriers in semiconductors, the conductivity for semiconductors is dependent on the contribution of both electrons and holes and is given by

$$\sigma = ne\mu_e + pe\mu_p, \tag{2.33}$$

where n (p) and μ_n (μ_p) are electron (hole) concentration and mobility respectively. Semiconductors have a large σ which possess either a very small band gap ($E_G \approx k_BT$) or high mobility of carriers. It can be found that heavily doped semiconductors with carrier concentrations between 10^{19} and 10^{21} cm^{-3} show a reasonable compromise between high α, σ and λ which lead to a high power factor ($\alpha^2\sigma$) and zT values [35].

The effective mass appeared in equation (2.29) indicates the density of states effective mass and depends on the curvature of the band. This parameter brings another conflict optimizing transport properties of TE materials. According to equation (2.29) and (2.31), a large effective mass provides a large thermopower but a small mobility of carriers and consequently a low σ. The relationship between the effective mass and mobility is related to electronic structure, scattering mechanism and anisotropy. It has been always a challenge to form a compromise between large effective mass and small mobility of carriers. There are materials such as ionic compounds with narrow bandwidth which have large effective masses and small mobilities. On the contrary, low effective mass and high mobility can be found in materials built of elements with small electronegativity differences. Finding an optimum effective mass is not an easy task. There are good TE materials with both large and small effective masses. For example polaron conductors such as oxides, chalcogenides possess a small mobility and a large effective mass whereas semiconductors such as SiGe, GaAs have large mobilities and small effective masses [35].

The interdependency between α and σ can be explained considering their relation to the density of states near the Fermi energy $D(E_F)$. According to Eq. 2.30, σ is proportional to n and consequently to $D(E_F)$ while α is proportional to the derivative of $D(E_F)$ [36]

$$\alpha \approx \frac{1}{D}\left[\frac{dD(E)}{dE}\right]_{E=E_F}. \tag{2.34}$$

As opposed to σ that increases with increasing $D(E_f)$, α decreases which can be precisely illustrated by Mott equation given by [36]

$$\alpha = \frac{\pi^2 k_B^2 T}{3e}\left[\frac{1}{\sigma(E)}\frac{d\sigma}{dE}\right]_{E=E_F}. \tag{2.35}$$

Quantum confinement of the density of states, hence, is a promising approach to enhance $(\alpha^2\sigma)$ proposed by Hicks and Dresselhaus [42]. In quantum-confined structures, the electron energy bands are narrower as the dimensionality decreases and the confinement increases which results in high effective masses and therefore large α [35]. Additionally, the electron and energy filtering can be also applied to decouple σ and α using engineered heterostructures leading to high zT values [35].

2.3.3. Thermal Conductivity

There exist three main mechanisms to transfer heat: conduction in solids, convection of fluids or gases and radiation. Conduction is defined as heat flow through a material when a temperature gradient is applied at the two ends of the material. Convection refers to the form of heat transfer which includes flow of mass as well as flow of energy in liquids or gases. Radiation indicates the transfer of energy by thermal radiation which is a type of electromagnetic radiation. The heat transmission by radiation is defined by Stefan-Boltzmann law which states that the heat flow per unit time and area is proportional to the fourth power of the temperature T^4.

Heat conduction characterized as the transfer of the internal energy by collision of particles is governed by the Fourier's Law [43, 44]

$$\overrightarrow{\dot{Q}}_{Fourier} = -\lambda A \overrightarrow{\nabla} T, \tag{2.36}$$

where $\dot{Q}_{Fourier}$ is the heat power through cross section A which is proportional to the temperature gradient ∇T. The proportionality factor λ, known as thermal conductivity, indicates the ability of a material to pass heat through the material. Since λ is a key enabler for the investigation of physical phenomena like TE effects as well as lattice defects and imperfections in solids, it is discussed in more details [44–46].

Depending on the material, the heat transmission can be caused by various independent excitations such as electrical carriers (electrons or holes), lattice waves (phonons), spin waves (magnons) or other excitations. While electrical carriers carry the majority of the heat in metals, in insulators heat is transferred mostly by phonons. λ can be therefore expressed based on the excitations which take place in the heat transmission. If we consider electrons and phonons as the main exciations to the heat transfer, λ can then be expressed as fallows [35, 44, 47]

$$\lambda = \lambda_e + \lambda_l. \tag{2.37}$$

Eq. 2.37 shows that the total thermal conductivity has two contributions. The electronic thermal conductivity λ_e which occurs through heat transport by charge carriers. The second component is lattice component of thermal conductivity λ_l which describes heat transport by lattice vibrations (phonons) [35, 36, 39, 47]. From the kinetic formulation of gases, λ is given by

$$\lambda = \frac{1}{3} C_v v l, \tag{2.38}$$

where C_v is the volume heat capacity. Considering phonons as excitations in the material, v and l denotes the velocity and mean free path of phonons, respectively.
We start first with λ_e. In metals or narrow band gap semiconductors, λ_e can be defined by Wiedemann-Franz law as follows [44]:

$$\lambda_e = \frac{\pi^2}{3}\Big(\frac{k_B}{e}\Big)\sigma T = L\sigma T, \tag{2.39}$$

where L is the proportionality factor between λ_e and σ which is called Lorenz number. For a degenerate electron gas, the value of L equals to $L_0 = 2.44 \times 10^{-8}\,\mathrm{W}\Omega\,\mathrm{K}^{-2}$. However, the value of L can differ depending on temperature and existing scattering mechanisms in the material. At very low temperatures, electron scattering is mainly due to impurities and Wiedemann-Franz ratio reaches the value of the free electron gas. At intermediate temperature, scattering mechanism becomes inelastic and the Wiedemann-Franz law may not be valid. Since the measurement of the electrical conductivity in solids is more straightforward than the thermal conductivity, we can use equation (2.39) to estimate the transport mechanism as well as the thermal conductivity in solids [44].

The second contribution to λ is λ_l which is the dominant contribution in insulators, some semiconductors and alloys. λ_l is referred to vibration of atoms about their equilibrium, known as crystal lattice vibration. This vibration is assigned to phonons. If we consider phonons as the excitation in heat transport, we can discuss the behavior of λ_l with temperature. While phonon velocity v does not generally alter with temperature, the C_v is dependent on temperature and its dependency on temperature has been studied

within the Debye and Einstein model. Phonon mean free path l — the average distance of a phonon wave packet between two interactions — relies strongly on temperature and is governed by various scattering mechanisms. There are various scattering mechanisms such as phonon-phonon, phonon-impurities and phonon-electron scattering. To determine λ_l at different temperature ranges, the dominant scattering mechanisms in the process must be defined [44, 47].

At high temperatures, phonon-phonon scatterings become important which is due to the anharmonic coupling between phonons in an umklapp-Process. This process occurs when the resulting phonon of the collision of two phonons lies outside of the first Brillouin zone. This process effectively changes the momentum of the phonon and leads to phonon scattering at high temperatures. The phonon-phonon scattering, therefore, causes l and λ_l to be inversely proportional to temperature.

At very low temperatures, there exist mostly low-energy phonons with long wavelength. These phonons have a long mean free path and therefore are not prone to interactions with themselves as well as the existing impurities or imperfections. Hence, phonon-phonon and phonon-impurities scattering do not effectively occur in this temperature range. This makes, therefore, l to be independent of temperature. λ_l will then be followed the temperature dependency of C_v and is proportional to T^3 [44].

As discussed, zT requires high σ and low λ. Since λ_e changes linearly with σ, the most promising approach to get a large zT value is to decrease λ_l . Glasses have the lowest lattice thermal conductivity which arises from a random walk of energy through the lattice whereas they exhibit a low electrical conductivity due to their poor electron crystal properties. Hence, they are not a good candidate for TE materials. Good TE materials are therefore crystalline materials in which the phonons are scattered while the electrical conductivity is not significantly disrupted [35, 48]. These materials are known as phonon-glass electron-crystal which stems from the need for as low as possible λ_l as well as high electronic properties.

2.4. Structure and Thermodynamics of TEG

TE generators and coolers can be made of any number of thermocouples with n- and p-type conductors. They are connected electrically in series and thermally in parallel through a conductive metal such as copper tabs. A schematic picture of a TEG is shown in Fig. 2.4. By employing a heat source on the top side of the TEG, charge carriers mostly electrons (holes) in n-leg (p-leg) diffuse to the bottom side. Consequently, This leads to a current flowing in the TEG whose direction is conventionally considered as the holes

movement (counterclockwise in Fig. 2.4). The TE materials forming TE legs should have low thermal conductivity which ensures that heat flows through TE legs restrictively and the temperature gradient is maintained between the hot and cold sides [1, 36, 39, 49].

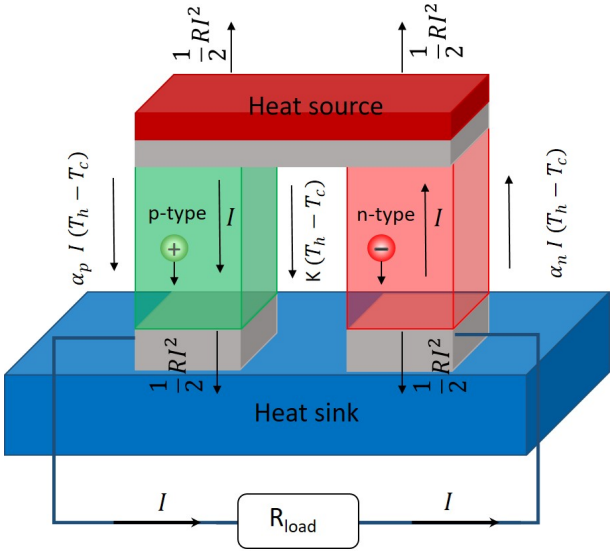

Figure 2.4.: Schematic configuration of a TE generator consisting of one pair.

In order to understand TE performance, a simple analytical thermodynamical model is described. In Fig. 2.4, a schematic configuration of a TEG is shown which is characterized by various performance parameters such as the incoming and outgoing thermal power, the produced electrical power, the induced electrical voltage and the electrical current flowing in the electrical circuit. The hot and cold junctions are connected to each other through n- and p-type legs which are polarized by a thermal and electrical potential.

With the extension of Eq. 2.18 and Eq. 2.19 for two TE legs of a TEG, $\dot{Q}_h$ and $\dot{Q}_c$ are given as follows

$$\dot{Q}_h = \dot{Q}_{Peltier} + \dot{Q}_{Fourier} - \dot{Q}_{Joule}, \tag{2.40}$$

$$\dot{Q}_c = \dot{Q}_{Peltier} + \dot{Q}_{Fourier} + \dot{Q}_{Joule}. \tag{2.41}$$

In the above equations, $\dot{Q}_{Peltier}$ denotes the Peltier heat contribution defined as $(\alpha_p - \alpha_n)IT_{horc}$ for the hot or cold side, $\dot{Q}_{Fourier}$ denotes the Fourier heat conduction defined as $K(T_h - T_c)$ and $\dot{Q}_{Joule}$ denotes the Joule heat contribution defined as $I^2R/2$. K is the thermal conductance of the device, including the contribution of n-type K_n, p-type K_p TE legs and thermal contact resistance. R is the total internal resistance of the device, including the contribution of n-type R_n and p-type R_p TE legs, metallic top and bottom contact and electrical contact resistance.

The produced electrical power P is defined as the difference between the heat absorbed at the hot junction $\dot{Q}_h$ and the heat emitted at the cold junction $\dot{Q}_c$ [1, 34, 50]:

$$P = \dot{Q}_h - \dot{Q}_c = \alpha I(T_h - T_c) - RI^2, \tag{2.42}$$

by connecting an external load resistance R_{load} and defining a load ratio $M = \frac{R_{load}}{R}$, the expressions of the electrical voltage, the current and the power output are given as fallows [34]

$$V_{out} = V_0 \frac{R_{load}}{R + R_{load}} = V_0 \frac{M}{1 + M}, \tag{2.43}$$

$$I_{out} = \frac{V_0}{R + R_{load}} = \frac{V_0}{R(1 + M)}, \tag{2.44}$$

$$P_{out} = \frac{V_0^2}{R} \frac{M}{(M + 1)^2}, \tag{2.45}$$

where V_o is the open circuit voltage

$$V_0 = \alpha(T_h - T_c). \tag{2.46}$$

The output power takes a maximum value of $P = \dfrac{V_0^2}{4R}$ at the point where load resistance equals to the total resistance of the device. The maximum P expression can then be given by[1, 34]

$$P = \frac{\alpha^2 \Delta T^2}{4R}. \tag{2.47}$$

The efficiency η of a TEG is described as the ratio of the produced P_{out} and $\dot{Q}_h$ at the hot side of the device [1, 34]. This is given by

$$\eta = \frac{P_{out}}{\dot{Q}_h} = \frac{IV}{\alpha I T_h - \frac{1}{2} RI^2 + K(T_h - T_c)} = \frac{\Delta T}{T_h} \frac{M}{M + 1 + \frac{(M + 1)^2}{ZT_h} - \frac{1}{2}\frac{\Delta T}{T_h}}, \tag{2.48}$$

with

$$\frac{1}{Z} = \frac{KR}{\alpha^2}, \tag{2.49}$$

where Z is the figure of merit of the TEG and ΔT is the temperature difference of T_h and T_c. The maximum efficiency η_{max} appears at $M_\eta = \sqrt{1 + Z\overline{T}}$ and is expressed as follows [34]

$$\eta_{max} = \frac{T_h - T_c}{T_h}\left(\frac{\sqrt{1 + Z\overline{T}} - 1}{\sqrt{1 + Z\overline{T}} + \frac{T_c}{T_h}}\right), \tag{2.50}$$

with the definition of mean temperature $\overline{T}$

$$\overline{T} = \frac{T_h + T_c}{2}. \tag{2.51}$$

The figure of merit of a thermocouple (based only on TE materials) can be defined as follows [39]

$$ZT = \frac{(\alpha_p - \alpha_n)^2 T}{((\rho_n \lambda_n)^{1/2} + (\rho_p \lambda_p)^{1/2})^2}, \tag{2.52}$$

and reaches its maximum by minimizing the product RK which is achieved when [1, 36]

$$\frac{L_n A_P}{L_p A_n} = \left(\frac{\rho_p \lambda_n}{\rho_n \lambda_p}\right)^{1/2}, \tag{2.53}$$

where A_n (A_p) and L_n (L_p) denote the cross section area and the length of n-leg (p-leg) materials, respectively.

2.5. Thermoelectric Materials

2.5.1. Overview-Classification

Classical TE materials, discovered in the 1950s, are based on Bi_2Te_3, PbTe and SiGe [51, 52]. These materials can be classified into three groups depending on their operation temperature: low, medium and high temperature materials. After theoretical predictions for high zT in TE materials in 1990s, they have received considerable interest in a wide range of commercial TE devices with applications in Peltier coolers and power generators [42, 53].

As an example of low temperature TE materials, Bi_2Te_3 alloys operating as p-type $Bi_xSb_{2-x}Te_3$ and n-type $Bi_2Te_{1-x}Se_x$ can be mentioned. Since these alloys exhibit zT

values around 1, they have been of interest in a variety of commercial TE applications such as Peltier cooling near room temperature and power generators for temperatures up to 500 K [52]. In 2008 Poudel *et al.* was able to achieve a substantial zT value of 1.4 at 373 K in a p-type nanocrystalline $Bi_xSb_{2-x}Te_3$ bulk alloy. Their method is based on ball milling and hot pressing of nanoparticles into bulk ingots. This results in a strong phonon scattering by interfaces in nanostructures which causes a significant decrease in thermal conductivity and consequently an increase in the zT value [54].

Group-IV tellurides such as PbTe, GeTe or SnTe are promising TE materials for medium temperature power generation (500-900 K) [35, 52]. The zT value is about 0.8 for n-type material which can peak at different temperatures by tuning the carrier concentration. $(AgSbTe_2)_{1-x}$ $(GeTe)_x$ with $zT > 1$ for both p- and n-type is another remarkable TE material which is known as TAGS [35, 55]. Only the p-type alloy $(AgSbTe_2)_{0.15}$ $(GeTe)_{0.85}$ with $zT > 1.2$ however has been successfully used in long-life TE generators [35, 56]. Some other promising medium temperature TE materials are skutterudites, clathrates, chalcogenides and half-Heusler compounds. Skutterudites and clathrates have received many attention due to their potential to reduce thermal conductivity through disorder in their unit cell. Skutterudites with crystal formula MX_3 (with M being Co, Rh or Ir and X being P, As or Sb) contain empty positions in the unit cell that can be filled by different elements such as rare-earth or heavy metals. Likewise clathrates are characterized with large cages which have the ability to accept rattling atoms as guests. Introducing guest atoms in the empty positions of these two materials causes phonon scatterings which result in reduction of lattice thermal conductivity and increasing the zT values [35, 57, 58].

Rare earth chalcogenides with Th_3P_4 structure have shown a relatively low thermal conductivity which is related to their affinity to host other elements due to the large number of random vacancies [59]. Half-Heusler compounds with a simple crystal cubic structure exhibit remarkably high power factors by doping with other elements. However, they typically have a high lattice thermal conductivity of $\sim 10\,\mathrm{W\,m^{-1}\,K^{-1}}$ which results in decreasing of zT values. This can be improved by alloying or introducing nanostructures into the system. For instance, lattice thermal conductivity can be reduced to $\sim 3\,\mathrm{W\,m^{-1}\,K^{-1}}$ and consequently $zT \sim 1$ in p-type $Zr_{1-x}\,Ti_x\,Co\,Sb_{0.8}Sn_{0.2}$ [60] and n-type $Hf_{1-x}\,Zr_x\,Ni\,Sb_{0.99}Sn_{0.01}$ [61].

TE materials operating at high temperature range above 800 K have been prospectively used in power generator in probes for deep space exploration. SiGe alloys for both n-type and p-type legs are typically used in TE generators in NASA spacecraft. The zT value is however fairly low due to its relatively high lattice thermal conductivity. YbMnSb is another promising TE material having extremely low lattice thermal conductivity due to the combination of different bonding types which leads to a complex structure. This complex structure along with high Seebeck coefficient and high electrical conductivity results in a high zT value of ~ 1 at a temperature of 900 K which is twice larger than

that of p-type SiGe . Hence, YbMnSb has been accepted as a substitution for SiGe alloys in NASA programs [35].

2.5.2. Thermoelectric Materials with high Power Factor

Regarding the definition of the Peltier effect, TE coolers or Peltier coolers are applied to pump heat from the cold side to the hot side or heat sink. They are prospectively used for many applications from household products such as small refrigerators for beverage cooling up to cooling of car seats and detecting sensors [62]. The aim of most cooling devices is pumping heat against the natural flow which is from hot side to cold side. The performance of these Peltier coolers is defined by its zT which increases by increasing power factor $PF = \alpha^2\sigma$ while decreasing λ [63].

However, these materials with high zT values are not considered for active cooling applications wherein the heat is pumped into the direction of the natural flux using an electrical work. An active cooling system integrated into electronic devices uses an electrical work to cool the hot spots where heat is dissipated from the hot area to a reservoir which acts as passive heat sink [64, 65]. For such applications, one should use TE materials with large λ as well as large PF instead of high zT TE materials [63, 66, 67]. M. Zebarjadi has recently studied the efficiency of active coolers which are based on materials with a combination of high λ and PF [63]. Defining an effective thermal conductivity, they have shown that a better cooling performance depends on both active and passive coolings. This means that both λ and PF should be large. It has been pointed out in Ref.[63] that best materials for this combination are metallic alloys such as Cu-Ni and Pd-Ag. In these two alloys, two transition metals from neighboring groups with large d and f density of states as well as similar electronic structures are selected to maintain the large σ whilst increasing the α [63]. These metallic alloys are not of interest in TE research due to their large λ and consequently low zT values, but they have been received considerable interest in active cooling applications.

2.5.3. Thermoelectric Materials in This Work

The aim of this work is to study the full in-plane zT characterizations, including α , σ and λ, of the TE materials which are synthesized by ECD technique. Hereby, cobalt nickel alloy with 75 % of Co and 25 % of Ni as n-type and Sb as p-type are electrochemically deposited and characterized using the developed transport device. These materials are the best candidates to be characterized using my transport device because on the one hand, they possess high λ used in active cooling applications and energy harvesting, and on the

other hand, they are low-cost materials and they have relatively simple manufacturing processes.

Recently, there has been different studies on electrochemically deposited CoNi alloy nanowires focusing on different subjects such as magneto-structural properties, magneto anisotropies and electro-magneto transport [68–73]. Another characterization of single CoNi alloy nanowires regarding their magnetothermal and magnetotransport properties was presented by Böhnert *et al.* They have studied the magnetothermoelectric effect and thermopower of CoNi alloy nanowires along with the correlation of these effects with the anisotropic magnetoresistance phenomena in these alloys [73, 74].

The latter one, antimony Sb, is a brittle silvery-white semimetal with a band structure similar to bismuth (Bi) which has been widely investigated. The electrochemical deposition of pure Sb and its alloys are of particular interest from the viewpoint of its potential use in many applications. One of the promising applications of pure Sb and its alloy can be found in Li- and Mg- batteries. Currently, there are considerable interest in metal based anode materials such as Sb, Sn and Al for Li-ion battery due to their high Li-storage capacities [75]. Electrochemically deposited pure Sb or co-deposited Sb and Sb_2O_3 have been studied as anode in Li-ion battery by Bryngelsson *et al.* [75]. Another interesting study on electrochemically deposited pure Sb and its alloy with Bi used as anodes for Mg-ion battery was presented by Arthur *et al.* [76]. Integration of Sb results in favorable properties such as increased hardness, electrical conductivity and expansion on solidification [77]. Furthermore, Sb can be used as a component in some semiconductors such as InSb and $InAs_{1-x}Sb_x$ [77, 78].

Moreover, Sb alloys such as $Bi_{1-x}Sb_x$, $CoSb_3$ and $\beta - Zn_4Sb_3$ hold a tremendous promise for developing of TE devices [7, 12, 20, 79–81]. The confinement growth of Sb nanowires using anodic alumina membranes influences the band structure and results in a change in carrier density. Consequently, some unusual transport properties can be expected in Sb nanowires as those observed in Bi nanowires [82]. The band structure of Sb is to some degree similar to that of Bi [82, 83]. Seeking for new and more efficient TE materials, it was demonstrated that $Bi_{1-x}Sb_x$ nanowires display a high PF because of the quantum confinement and a reduced λ due to improved phonon scattering [20, 84]. Another interesting study on Sb nanowires has been presented by Wagner *et al.* They have investigated TE characterization of Sb nanowire networks prepared by pulsed ECD technique in ion track-etched polymer membranes [20].

3. Experiments and Methods

The main goal of this thesis was to develop a transport platform for full in-plane zT characterization of electrochemically deposited TE material. In order to achieve this goal, I needed to use a variety of techniques and methods in the fabrication, characterization and analysis.

The structure of this chapter is as follows. In section 3.1, an overview of the treatments and techniques used in the fabrication of the transport device is presented. First, each technique is briefly introduced followed by the favorable parameters and conditions which are needed for a better understanding of the process flow. Then electrochemical deposition technique (ECD) and its corresponding conditions are explained in section 3.2 which was applied to synthesize of TE material on the pre-structured transport device. Section 3.3 is devoted to the preparation of bulk samples and thin films which were used as reference samples to validate the characterizations results within the transport device. In section 3.4, it is shown how and under which conditions the measurements within the transport device can be performed in a commercial Dynacool measurement system. Besides, I give a short introduction to the characterization devices which were applied to measure TE properties of the reference samples. Section 3.5 is devoted to the 3D finite element simulation which is performed using Comsol Multiphysics. The simulation was used to verify the 1D analytical approach used for the evaluation of the measurement data as well as to provide information about accuracy of the measurement.

3.1. Thin Film and Device Technology

The fabrication of the transport device comprises micro-structuring, different kinds of depositions as well as wet cleaning and etching processes. This section is split into three parts. In the first part, the treatments and techniques used in the micro-fabrication and pre-structuring of the transport device are described as photolithography technique. In the second part, various deposition techniques and their according parameters used during the transport device fabrication are briefly discussed. In the final part, the basic principle of etching processes are addressed.

3.1.1. Micro- and Photolithographic Structuring

Micro-fabrication has attracted much attention due to its potential use in interdisciplinary research bridging physics, chemistry, material and bio-medical science. It is defined as process of design, fabrication and characterization of structures, devices and systems in micro-scales such as MEMS, microfluidics and lab on the chip [85–87]. A major principle of micro-fabrication is based on lithographic technique. Lithography is typically used to transfer a pattern to a photo-sensitive material using an appropriate exposure system [68, 87]. A photo-sensitive material is a photo-sensitive polymer, the photoresist, which experiences changes in its structure when it is exposed to radiation source [88]. Depending on the type of the photoresist and the radiation source, there are different types of lithographic methods, namely, electron beam lithography, x-ray lithography and optical lithography (photolithography) [89–93]. I briefly introduce the basic concept of photolithography technique which was applied in this work.

Photolithography makes use of a visible or ultraviolet (UV) light to project a pattern on the photoresist [93, 94]. There exist two types of photolithography, mask-based and maskless [95]. The mask-based technique relies on the transformation of a pattern from a photographic mask on a substrate which is favorably useful for high volume manufacturing. For low-volume manufacturing, however, mask-based technique is not preferable due to costs and complexity of the mask as well as tools.

The latter is known as maskless photolithography which is here used in micro-fabrication. Maskless technique refers to a process which transfers a pattern onto a substrate, without utilizing a photomask, that is, a photomask is directly replicated [93]. In this technique, the design is taken by system and the pattern is directly exposed onto the resist-covered substrate using a spatial light modulator (SLM) which acts as a programmable mask. The advantages of the maskless process as opposed to the masked process are as follows:
1) Using an expensive photomask whose preparation is very time consuming is avoided.
2) Redesigning the pattern using CAD is much easier than changing the photomask.

In this work, the process was mainly carried out in four steps: photoresist application, soft backing, exposure and development. The photosensitive polymer was spin coated and soft backed on the Si-substrate which was previously cleaned. The coated substrate was then exposed using a direct writing technique in a laser writer µPG 101 (Heidelberg Instruments) equipped with a 375 nm laser. Hereby, the exposed part of the photoresist experiences photochemical reaction and was developed dipping the substrate in a developer solution. The patterned substrate can then be used for further treatments such as sputtering deposition, ECD or any kind of etching processes. Fig. 3.1 shows a schematic overview of a lift-off process and an etching process as an example of treatment after photolithography structuring.

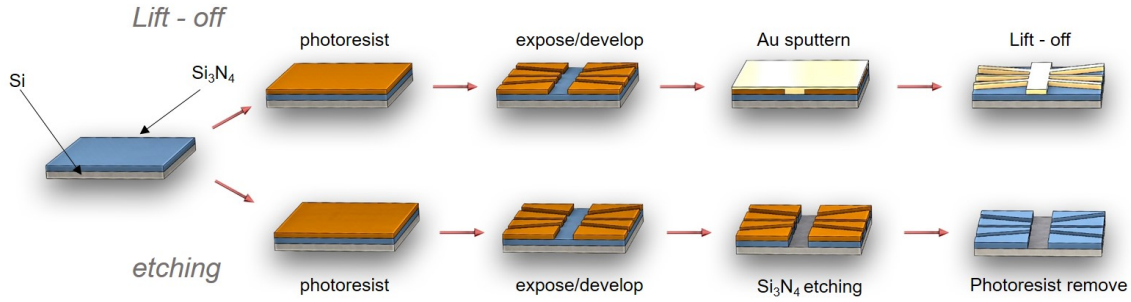

Figure 3.1.: A schematic overview of a lift-off and an etching process along with the photolithography structuring.

For each of these treatments, special requirements need to be met in order to achieve the desired results. For example, when using ECD technique, it is recommended to use a photoresist with a good adhesion to the substrate as well as an enhanced stability in the electrolyte such as positive photoresists AZ 4500 and AZ9260. For a Lift-off process, in which photoresist is removed together with the material deposited on the pre-structured substrate (see Fig. 3.1 lift-off), it is favorable to use an undercut photoresist such as image reversal resist AZ5214 or bilayer photoresist LOR 3B and MA-P 1205. Depending on the applied photoresist, there exist two classifications of photoreists, positive and negative. In positive photoresist the exposed part is dissolved or developed while in negative photoresist the unexposed part gets removed.

In this work, three positive photoresists, bilayer LOR 3B and MA-P 1205, AZ 5214 and AZ9260 with their according developer ma-D 331, AZ 726 MIF and AZ 400 K were employed to be patterned, respectively. For lift-off processes, a bilayer LOR 3B (a non-photosensitive polymer provided by MicroChem) as bottom layer and MA-P 1205 (a photosensitive positive photoresist) as top layer were used. The Photoresist AZ5214 was applied to partly cover the transport device covered with SiO_2 passivation, since it provides a high resolution with a thickness of 1 µm. For ECD of the material with some micrometers thickness in a cavity structured on a Si substrate, AZ9260 photoresist was applied due to its good compatibility with the deposition technique, its good adhesion to the substrate and its appropriate thickness.

3.1.2. Deposition

Thin film deposition refers to a technology of creating and coating a very thin film material onto a substrate surface. This technology has been prospectively used in a variety of products and devices such as medical, optoelectronic and electronic semiconductor devices. Depending on physical or chemical reactions which happen in a deposition process, thin film deposition techniques can be usually classified into two major groups: chemical and physical deposition techniques. In chemical deposition, deposition of thin film material relies on a chemical reaction between the substrate and the material being deposited. The chemical methods comprise gas-phase and solution techniques. The gas-phase methods include chemical vapor deposition (CVD) and solution methods include sol-gel, spin and dip coating and ECD [96–98]. As opposed to chemical deposition, in physical deposition technique, materials in the form of solid, liquid or vapor are released and physically transferred onto the substrate surface without any chemical reaction. Laser ablation, molecular beam epitaxy and physical vapor deposition (PVD) based methods are some examples of physical deposition technique [96, 98, 99]. The choice of an appropriate deposition technique depends on various factors, e.g. the structure of the substrate, the applied temperature and the thickness of desired material. In this work three main deposition methods were employed to develop the transport device, namely, sputtering, atomic layer deposition (ALD) and ECD. Furthers, spin-coating was used to apply photoresist on the substrate for the micro-structuring and photolithography.

Spin-Coating

Spin-coating is a deposition technique usually used in micro-fabrication to deposit uniform thin polymer material (photoresist) on a substrate. The apparatus used for spin-coating is called a spin coater or spinner. In a common way, a small amount of coating material in solution is applied on the center of the substrate surface with a pipette. The substrate is fixed to a plate which is rotated at high velocity in a range of 1000-8000 rpm. The centrifugal force of the rotation makes the material to spread uniformly on the whole surface of the substrate. There are some factors that can influence the thickness of the desired coated film: the rotation speed and acceleration of the spinning plate, viscosity of the solution and surface tension [100–102].

This technique offers some advantages compared to other deposition techniques: it is easy to operate for thin film deposition, there is only a small loss of material, it requires little maintenance and care and above all it is a relatively inexpensive technique which does not need any vacuum. However, it could suffer disadvantages such as complication with fabrication of multilayer structures as well as extremely thin films, probability of surface

contamination (humidity, oxygen dusts, etc.) and difficulties to control deposition process [100].

This technique was used in micro-fabrication to create a pattern on the Si-substrate using photolithography technique. Depending on the desired treatments and material thickness, namely, a lift-off process, etching or ECD of material, I spin coated three different photoresists (bilayer LOR 3B and MA-P 1205, AZ 5214 and AZ9260) on the Si-substrate. Parameters of spin coating (the rotation speed and time) needed to be optimized for each photoresist (shown in Table 3.1).

Table 3.1.: Parameters of spin coating for the applied photoresists.

Photoresist	rotation speed (rpm)	spining time (s)
LOR 3B	3500	45
MA-P 1205	3500	30
AZ 5214	4600	40
AZ9260	2400	60

Sputtering

Sputtering refers to a plasma assisted deposition technique which is widely used to deposit thin films on the substrate. It is a PVD process which utilizes an electrically ionized plasma gas in a vacuum system. In this technique, the material is released from a source material (target) by a physical process and is condensed on the substrate. The simplest form of sputtering is diode sputtering which was developed over the years to various techniques such as magnetron sputtering and high-power pulse magnetron sputtering. In this technology, a target source to be deposited and a substrate to be coated are placed in a vacuum chamber containing an inert gas, usually argon. By applying a voltage between the target and the substrate, a glow discharge happens and the inert gas is ionized. The voltage can be supplied in different ways, ranging from direct current (DC) for conductive targets to radio frequency (RF) for non-conductive targets. The positively charged ions are accelerated to the surface of negatively charged target causing a collision cascade. As a result of the collision cascade, some target atoms are released from the target surface with sufficient energy. They move through the vacuum chamber and are deposited on the substrate [99, 103, 104].

Magnetron sputtering is referred as a further development of diode sputtering which is characterized by a combination of an electrical and magnetic filed. In magnetron

sputtering technique, permanent magnets are used behind the negatively charged source target to increase the ion density in front of it. Hereby, electrons are forced to move on helical path around magnetic lines. This increases the number of target ions and consequently the rate of ionization compared to conventional diode sputtering [99, 105, 106].

In this work, magnetron sputtering (Torr CRC622) was employed to deposit Cr/Au and Ti/Pt as adhesion and seed layer. Cr/Au was sputtered as conductive seed layer for ECD of the TE material. This layer was deposited as first thin film on the pre-structure Si-substrate using a DC current of 50 mA for Cr (deposition rate of $\sim 0.7\,\text{Å}\,\text{s}^{-1}$) and RF power of 80 W for Au (deposition rate of $\sim 1.4\,\text{Å}\,\text{s}^{-1}$), respectively. The second layer was Ti/Pt which was sputtered on top of the pre-structured Cr/Au layer using a DC current of 50 mA for Ti (deposition rate of $\sim 0.7\,\text{Å}\,\text{s}^{-1}$) and RF power of 80 W (deposition rate of $\sim 1.2\,\text{Å}\,\text{s}^{-1}$) for Pt. Both depositions were performed at a vacuum chamber of 10^{-3}-10^{-4} mbar containing a Ar plasma with a gas flow of 15 sccm.

Atomic Layer Deposition (ALD)

Atomic layer deposition (ALD) as a special type of CVD is a promising technique for preparing high quality thin films on planar or 3D substrate. This technique involves a sequential use of two or more chemical precursors wherein gaseous reactants are alternately pulsed into a chamber with intermediate reactor purging (see Fig. 3.2). As opposed to CVD, where chemical precursors are introduced simultaneously, in ALD chemical precursors react with the surface of the substrate in a sequential and self-limiting way. It means that the thin film growth continues on the surface until reactions between precursors and accessible surface reach a saturation [68, 103].

ALD is a tremendous promise to develop advances in MEMS, oxide thin film transistors (TETS), solar cells and high density memories. This deposition technique offers an accurate control of film thickness and composition as well as uniform growth over large area at low temperature. It also fulfills severe requirements for ultra-thin dielectrics for sub 100 nm (CMOS) transistors [68, 107–109].

For the fabrication of the transport device, I used a passivation layer which serves as an electrical insulation between the heating stripe and the upcoming TE material. There were two options available for the deposition of an electrical isolation layer, Al_2O_3 and SiO_2. I used SiO_2 as dielectric layer due to its compatibility with the applied photoresist and developer for photolithography and micro-structuring. The Al_2O_3 was not compatible with the developer AZ 400 K which corresponds to the photoresist AZ9260. This photoresist was used to structure of the cavity for the TE material deposition.

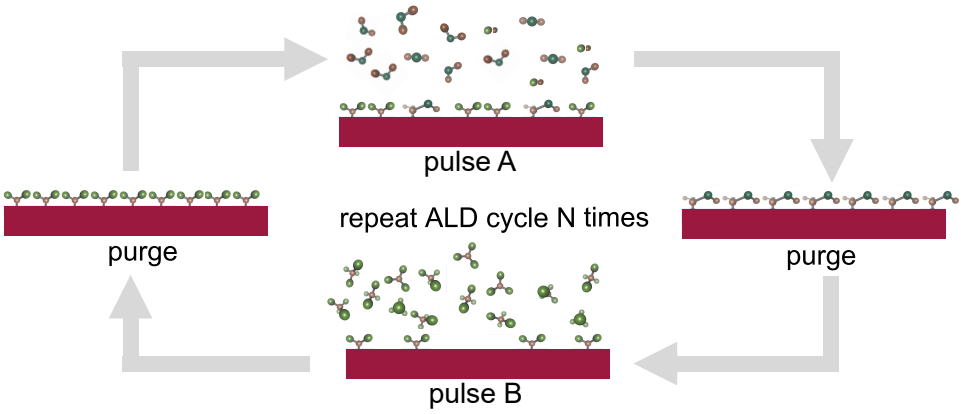

Figure 3.2.: A schematic picture of ALD prozess with two precursors, image courtesy of Linnart Zähr.

The SiO_2 passivation layer was deposited in a commercially available GemStar XT-R thermal bench-top ALD system from Arradiance in a stop-exposure mode with a temperature of the reactor chamber of 200 °C. 3-Aminopropyltriethoxysilane (APTES) was used as the reductant, whereas the combined subsequent use of H_2O and O_3 acted as oxidizer. O_3 was provided by a BMT 803N ozone generator operated with pure oxygen. The metal organic precursor was heated to 100 °C to ensure a sufficient vapor pressure. The pulse time was 75 ms (50 ms, 50 ms), the exposure time 1 s (1 s, 4 s) and the pump time 20 s (4 s, 55 s) for APTES (H_2O, O_3). With these parameters 950 cycles resulted in 50 nm of SiO_2 [110, 111].

3.1.3. Etching

Etching is a process of removing a material previously deposited on the substrate. This technology is widely used as a treatment in micro-fabrication. There exist two major classes of etching processes, wet chemical etching and dry etching. In wet chemical etching process, the material is etched by dipping the sample in an appropriate chemical solution. This technique is here applied to etch Cr/Au as well as the Si-substrate. The latter is dry etching where the material is sputtered or dissolved using reactive ions or a vapor phase etchant. Dry etching can be classified in reactive ion etching (RIE), sputter etching and vapor phase etching. In the following, wet etching and RIE are briefly introduced which were applied in the fabrication of the transport device.

Wet Etching

Wet etching is defined as a process in which the material being etched is dipped in an appropriate chemical solution (etchant) or the solution is sprayed on the material. Wet etching process is divided to isotropic (crystalline orientation independent) and anisotropic etching (crystalline orientation dependent) [101, 102, 112]. Wet etching is mostly isotropic which involves a homogeneous etching in all direction and the material being etched is removed uniformly from all direction (see Fig. 3.3 b). However, some single crystalline materials indicate aniostropic etching, i.e. the etching rate varies in different directions (see Fig. 3.3 a).

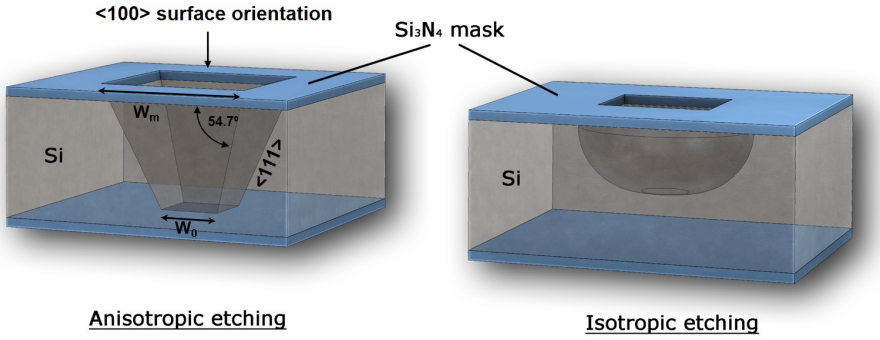

Figure 3.3.: (a) Anisotropic etching of single crystal Si (b) isotropic etching.

Single crystalline silicon is the classic example of wet anisotropic etching process that can usually be achieved using potassium hydroxide (KOH) solution. KOH solution provides a characteristic V-shaped or inverted pyramidal cavity structure in silicon $< 100 >$. Using this solution, silicon $< 100 >$ can be etched in pyramidal cavity with the sidewalls corresponding to $< 111 >$ crystal plane [113]. Since the etching rate depends on crystallographic orientation, the $< 100 >$ plane is etched faster than the $< 111 >$ plane.

In this work, an aqueous 40 % KOH solution at 80 °C was used to selectively etch the Si-substrate. The Si-substrate was structured by photolithography process in order to open a mask window. The width of the achieved pyramidal cavity W_0 can be defined by the thickness of the Si substrate z and the size of the mask window W_m [113]

$$W_0 = W_m - 2cotan(54.74^\circ)z \tag{3.1}$$

The desired mask for photolithography and micro-structuring need to be compatible with the applied etchant solution. It is important to use a mask that does not dissolve or its etching rate is considerably slower than the target material. For the fabrication of

the transport device eliminating the impact of the seed layer, I used Cr etchant solution (TechniEtch Cr01, etch rate $\sim 60\,\mathrm{nm\,min^{-1}}$) and Au etchant solution (KI/I_2, etch rate $\sim 1\,\mu\mathrm{m\,min^{-1}}$) to remove Cr and Au, respectively.

Dry Etching

RIE refers to one of the major applications of plasma treatment used in the fabrication of semiconductor and integrated circuit devices. This technique is carried out in a vacuum chamber using several reactive gases and an inert gas (Ar). Dry etching consists of two parts, physical and chemical etching. By a power source, a plasma is generated which contains free electrons as well as positively charged ions. Ions are accelerated towards the surface of the substrate which is placed in a platter in the bottom side of the chamber. High energy ions from plasma attack the surface of the substrate being etched and cause sputtering of atoms without a chemical reaction, i.e. ions bombardment knocks atoms out of the material resulting in an anisotropic etching. Additionally, a chemical part of etching process is isotropic which is caused by the diffusion and reaction of some of the particles with the substrate and also physically milled out materials so that they can not be re-deposited on the substrate surface [114, 115].

Development of a dry etching, however, is a challenging task regarding the adjustment of many parameters to balance the chemical and physical etching. In this work, RIE was employed to etch Si_3N_4 and SiO_2 through fabrication of the transport device using Etchlab (SENTECH SI220). The available precursor gases are Fluoroform CHF_3, Tetrafluoromethane CF_4, sulfur SF_6, oxygen O_2 and argon Ar. CHF_3 and O_2 were the applied gases for etching of Si_3N_4 and SiO_2. Additional to the etching process, I used RIE applying O_2 to remove photoresist residual before starting the next treatment on the sample. This is especially important for the ECD technique in which the substrate was cleaned and activated by RIE using O_2 before starting the deposition process.

3.2. Electrochemical Deposition Technique

This section is devoted to describe the ECD technique which was used for synthesis of the TE materials being characterized through the fabricated transport device. In this section, first some basic principles and concepts of electrochemisty and ECD are explained. Then, the transport mechanism in an electrochemical cell is discussed in subsection 3.2.2. The applied setup for ECD and two main mechanisms used in this work are shown in subsection 3.2.3 and subsection 3.2.4, respectively. In subsection 3.2.5, I briefly explain cyclic voltammerty which was used for monitoring of electrochemical reactions of various

materials in solution in an electrochemical cell and to define the appropriate reduction potential.

3.2.1. Basic Principles of Electrochemistry

Electrochemistry can be characterized as the study of chemical reactions when electrically conductive electrodes are placed in an electrolyte. These reactions involving oxidation and reduction, known as redox reaction, take place at the interface of electrode/electrolyte by transferring electrons. Hence, the understanding of interactions between the current conducting electrolyte and current supplying electrode is vital for unlocking potential use of electrochemistry in a broad range of fields such as corrosion, ECD, battery and fuel cell technology. Among them ECD of metals and alloys is of wide interest for synthesis of thin film coatings on conductive surfaces for integrated circuit in CMOS technologies. Over other deposition techniques, ECD has the advantage that it does not require any vacuum system and is thus cost-effective to produce thin film materials. It also indicates high scalability, compatibility with CMOS back-end technology wherein the material composition and structure can be controlled through modification of deposition parameters [68, 116].

Electrodeposition of metals involves formation of a desired metal coating on a conductive surface using a conductive solution, the bath electrolyte. A bath electrolyte contains positively and negatively charged species of dissolved metal salts that can be prepared in aqueous or non-aqueous solutions [68, 73, 116]. The deposition is performed by applying a potential difference between two electrodes in an electrochemical cell containing the bath electrolyte. The positive electrode (cathode) acts as working electrode on which desired metal ions are reduced and deposition is to be formed, while the negative electrode (anode) is used to complete the electrical circuit where oxidation reaction happens. This redox reaction is represented as follows:

$$M^{n+} + n^{e-} \longleftrightarrow M, \tag{3.2}$$

where M and M^{n+} denote soluble reduced and oxidized form of species in the electrolyte, n denotes the number of electrons transferred between electrode and solution, respectively. This reversible electrochemical reaction can be represented by Nernst equation which relates the equilibrium potential of the cell E_{eq} to concentration of species in the solution.

$$E_{eq} = E^0 + \left(\frac{N_A k_B T}{nF} ln \left(\frac{a_{M^{n+}}}{a_M} \right) \right) \tag{3.3}$$

where N_A is the Avogadro constant, k_B is the Boltzmann constant, T is the absolute temperature, F is Faraday constant, E^0 is the reference electrode potential and $a_{M^{n+}}$ and a_M are activities of oxidized and reduced species. By flowing a current in an electrochemical cell, the electrochemical reaction is driven out of equilibrium and the potential of electrode E^{dep} varies from Eq. 3.3. The difference between two potentials is defined as overpotential η_{over}

$$E^{dep} = E^{eq} + \eta_{over}. \tag{3.4}$$

The quantity of the material deposited at the electrode surface during a typical ECD is related to the cathodic current $I(t)$ which flows through an electrochemical cell. For this process, the Faraday's law is used to relate the mass of the deposited material m and the $I(t)$:

$$m = \frac{M_M}{nF} \int_0^{T_t} I(t)dt \tag{3.5}$$

where M_M is the molar mass of the metal that undergoes electrodeposition and T_t is the duration of the process. This relationship was calculated by assuming that all the metal ions M^{n+} are reduced and deposited at the surface of the working electrode (metal surface), i.e. all current flowing through an electrochemical cell is caused by reduction of the metal ions M^{n+} resulting in an efficiency of 100 %. In reality, the electrochemical deposition is, however, accompanied with other side reactions that happen simultaneously with the main reaction. Hydrogen evolution is one example which is evidenced in condition such as relatively high cathodic potential in acidic solution which leads to decreasing the efficiency of the process [68, 73].

3.2.2. Transport Mechanism

In an ECD process, an applied potential to electrode results in an electron transfer to and from the electrode surface which subsequently leads to a faradic current. There exist various factors that influence the electrochemical reactions as well as the current such as applied potential to electrode, transport of electroactive species inside the electrolyte and the reaction rates at the electrode/electrolyte surface where the electron transfer occurs. Fig. 3.4 shows an overview of an ECD process including different processes, namely, mass transport and electron transfer. Mass transport is defined as movement of electroactive species inside of the electrolyte solution, while electron transfer describes an exchange of charge at the electrode/electrolyte surface. These two mechanisms are the critical factors for controlling of an electrochemical reaction [68, 117, 118].

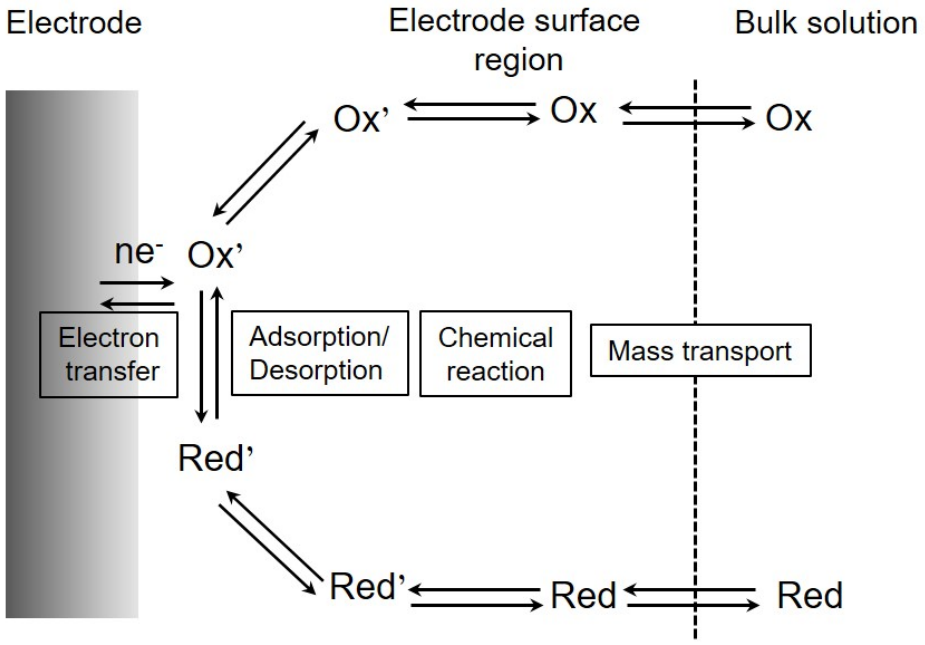

Figure 3.4.: Pathway of a general electrode reaction in an electrochemical cell [117].

When an electrochemical deposition reaches an equilibrium condition, an electrical double layer is formed near the electrode surface, i.e. charges build up on both sides of the electrode surface (see Fig. 3.5). This layer serves as a parallel plate capacitor with one plate being the electrode side with excess electrons while the other plate is formed by ions participating in solution. Ions composing the side of the double layer are normally arranged in three regions, including, inner Helmholtz plane (IHP), outer Helmholtz plane (OHP) and diffuse layer. IHP consists of oriented polar water molecules and some specifically adsorbed anions and OHP is a layer of fully hydrated cations which are adsorbed onto the electrode surface by loosening the solvation sheath and transferring electrons with electrode. Beyond the double layer, there is a diffuse layer with a thickness of microns, much larger than the double layer, comprising of hydrated anions and cations. Because of the consumption of species incorporated in deposition, there is a depletion of these species near the electrode surface resulting in a concentration gradient. Hence, fresh ions are supplied and moved from bulk of electrolyte to the double layer through mass transport. Three processes are responsible for mass transport inside of an electrochemical cell: diffusion is due to concentration gradient caused by consumption of species near electrode, migration is due to the applied potential to electrode and convection is due to concentration and temperature fluctuation. Diffusion occurs near the surface of electrode while convection and migration are dominant mechanisms in the bulk solution and in the border of bulk/diffuse layer [68, 119].

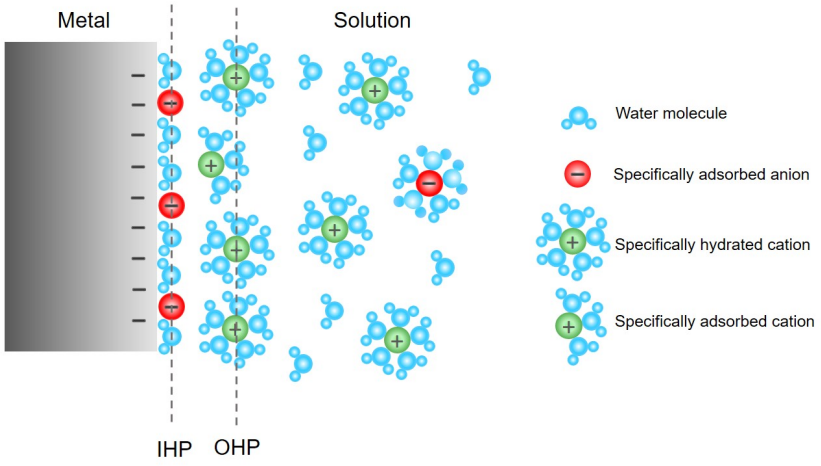

Figure 3.5.: A schematic overview of the electrical double layer builds up at the electrode/electrolyte interface.

The deposition process and electrochemical reactions are controlled either by mass transport or electron transfer at the electrode. If the concentration of ions arriving to the electrode surface is zero, kinetics is fast and deposition process is controlled by diffusion. On the other side, when the consumption of ions at the electrode surface is low, diffusion is fast and the process is controlled by kinetics. Hence the deposition process in the diffusion-limited area is highly dependent on the size of the diffusion layer which results to a change in the concentration gradient and the current. The reduction of the metal ions in a deposition process is as follows: 1) movement of hydrated ions in the bulk solutions towards the surface of the metal electrode through migration, diffusion or convection, (2) transport of metal ions in the diffused double layer followed by dehydration of ions in the Helmholtz double layer, (3) neutralization and adsorbtion of ions at the surface of electrode and (4) migration and incorporation of the absorbed metal atoms to the growth point at the electrode surface [68].

3.2.3. Electrochemical Deposition Setup

ECD processes are usually carried out in an electrochemical cell with either two or three electrodes as the one shown in Fig. 3.6. The simplest form of the ECD cell, known as two-electrodes cell is comprised of a working electrode and a counter electrode which are separated by a solution or electrolyte. The working electrode is defined as electrically conductive electrode on which the desired reaction occurs applying an appropriate potential. Depending on the applications and desired deposition, one can employ different working electrodes such as Au, Pt, Ag and glassy carbon. In this work, the transport

device acts as working electrode which consists of an electrically conductive seed layer Au on which a defined cavity was structured. For more details about the transport device and its corresponding structure, I refer readers to chapter 4. The counter electrode, known as auxiliary electrode, is applied to complete the current circuit in an electrochemical cell which commonly does not take part in the deposition process. In this work, a Pt net was used as counter electrode with a surface area much bigger than the working electrode surface to avoid any limiting factor in the kinetics of the deposition process. This two-electrodes cell can be employed when a precise control of the potential across working electrode/electrochemical interface is not important, i.e. the behavior of the whole electrochemical cell plays the major role in process development.

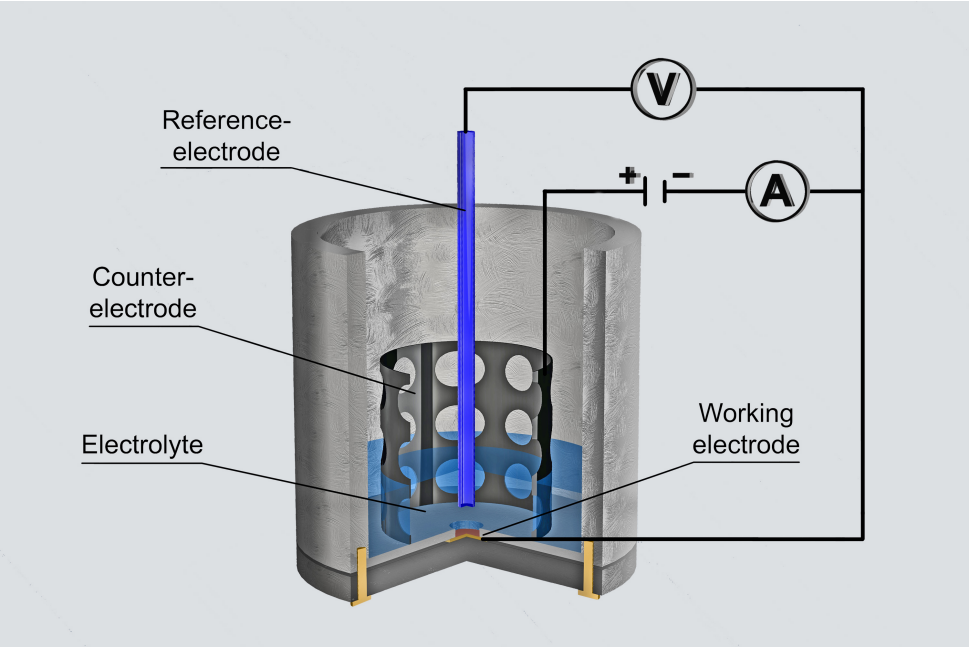

Figure 3.6.: A schematic view of a three-electrodes electrochemical cell.

However, a three-electrodes cell is used for measurement and control of the potential across the electrochemical interface at the working electrode. This configuration is supplied with a reference electrode that has a stable and well-known potential. The introduction of a reference electrode allows sufficient control of the electrical condition resulting in a more reproducible and stable ECD process. In other word, the reference electrode makes an indirect contribution in an electrochemical cell and does not participate in the electrochemical reactions. The most conventional reference electrodes are the silver/silver chloride electrode (Ag/AgCl) and the calomel electrode (Hg/Hg_2Cl_2) which are quoted relative to standard hydrogen electrode (SHE).

3.2.4. Electrodeposition Methods

ECD of metals and alloys can be mostly performed in two methods, namely, potentiostatic and galvanostatic [73]. In potentiostatic method, the potential of the working electrode is kept constant during the deposition process using a potentiostat. A potentiostat is an electronic device which defines the potential difference between the working electrode and the reference electrode whilst controlling the potential of the counter electrode against the working electrode. The potentiostatic method provides the ECD of alloys and multilayered structures through adjusting of the electrodeposition potential. Hence, it has widely been used for synthesis of cobalt, nickel, iron and their alloys with tuned composition [73].

The applied potential on the working electrode is the potential required for reduction of metallic ions that causes a shift of equilibrium of the reaction to the deposition of metal as well as modifying the kinetics of the deposition. The reduction potential can influence the micro-structure and crystalline grain size impacting the physical properties of the deposited material [73].

Regarding the latter method, galvanostatic, a constant current is applied between the working electrode and the counter electrode and the potential between the working electrode and reference electrode is continuously monitored. The critical feature in this method is that the surface area of the working electrode must be defined which is not straightforward for some substrates and templates. As opposed to potentistatic one, galvanostatic method which is a favorable method in industrial applications provides a constant growth rate enabling a better control of the amount of the deposited material [73].

Both methods can be also performed in pulsed electrodeposition. In pulsed mode, a deposition potential or current is applied in a short pulse on-time t_{on} followed by a relaxing time of t_{off} which can be related to each other using a common parameter known as duty cycle D

$$D = \frac{t_{on}}{t_{on} + t_{off}}. \tag{3.6}$$

As it was discussed in 3.2.2, there is a depletion of metal ions in the double layer near the working electrode which causes a concentration gradient and a transport of fresh ions to the electrode surface. Applying electrodeposition in pulsed mode provides easy availability and rearrangement of metal ions during the t_{on} by controlling and adjusting the t_{off} which in turn improves the uniformity of the deposition as well as reduces the roughness and porosity of the desired deposition. Another advantage of pulsing, compared to constant potentiostatic and constant galvanostatic, is that some unfavorable negatively charged ions at the electrode surface can be discharged during the adjusted t_{off}. These

negatively charged ions are formed at the electrode surface which affect the deposition and prevent the passage of metal ions.

In this work, I characterized thermoelectric properties of electrochemically deposited cobalt nickel with the composition of 75 % Co and 25 % Ni as n-type and Sb as p-type using the fabricated transport device. Hereby, $Co_{75}Ni_{25}$ and Sb were electrochemically deposited on the photolithography pre-structured transport device which acts as substrate (working electrode) in the ECD (see section 6.1.1 and 6.2.1).

3.2.5. Cyclic Voltammetry

Cyclic Voltammetry (CV) is a characterization technique to study the ECD behavior in an electrochemical cell. In CV, the potential of the working electrode is linearly swept between two values at a constant scan rate whilst recording the current corresponding to the potential. In this method, the applied potential, measured against a reference electrode, starts at a defined value and comes back to the same value after a period of time. For the case that the potential would first scan negatively, the cathodic current starts to increase by increasing the potential and it reaches a maximum when the cathodic reduction potential is achieved. At the cathodic reduction potential, all metal ions at the electrode surface have been reduced resulting in a depletion of ions. After the reduction potential, the current starts to decrease which is typical of a regime where the deposition is limited by mass transport of metal ions (mostly diffusion) from the bulk to the electrode surface. During the reverse sweep, the product at the electrode surface starts to oxidize and anodic peak potential is reached when all metals at the surface undergo oxidation [116, 118, 119]. In this work, CV was used to find the desired reduction potential for an ECD of TE material.

3.3. Reference Samples

To assure the reliability of the measurement achieved using the transport device, the results of the electrochemically deposited TE materials were compared to those obtained for reference samples. In this work, two TE thick films, $Co_{75}Ni_{25}$ and Sb were characterized using the developed transport device and accordingly the $Co_{75}Ni_{25}$ bulk sample, the Sb bulk sample and the thermally evaporated Sb thin film were used as reference samples. In the following, I address the preparation of arc-molten $Co_{75}Ni_{25}$ bulk sample in subsection 3.3.1 and the fine grained Sb bulk sample and the thermally evaporated Sb thin film in subsection 3.3.2. All these reference samples were produced in house.

3.3.1. CoNi Reference Sample

A $Co_{75}Ni_{25}$ bulk sample was chosen as reference which was produced through arc-melting technique. Hence, a $Co_{75}Ni_{25}$ ingot was prepared by vacuum arc melting of Co (99.9 %) and Ni (99.7 %) granules. The melting was performed under Ar atmosphere where the chamber was evacuated followed by purging with high purity Ar three times. During the melting process the ingot was placed on a water cooled Cu plate. The ingot was molten five times while flipping the sample after each melting step to ensure the same solidified condition of the ingot and make the micro-structure uniformed. After arc-melting, the sample was sealed under vacuum (10^{-4} mbar) in a fused silica tube and annealed at 1180 °C for 24 h. After annealing the sample was quenched in a water bath [111].

3.3.2. Sb Reference Sample

The first reference sample was Sb fine grained bulk sample which was prepared using the field assisted sintering technique (FAST) also called Spark Plasma Sintering (SPS). The latter one, the Sb thin film, was prepared using the thermal evaporation technique.

To produce the fine grained bulk sample, 13.3 g Sb powder with a (99.5 %) purity and a grain size of 200 mesh from *Alfa Aesar* was used. Then, the pressing die with a diameter of 20 mm was filled with Sb powder under Ar atmosphere in a glovebox. The surface of the die was covered with graphite foil to avoid the contamination of the sample or the die. Hereafter, a strong DC current was applied and passed through the graphite pressing die and heated it rapidly through joule heating. This led to the sintering of powder with lower temperatures than in conventional sintering method preventing grain growth and phase separation. The sintering process was carried out under vacuum condition for three minutes at a temperature of 550 °C and a pressure of 50 MPa.

The second reference sample, Sb thin film was deposited on the commercially pre-structured zT measurement chip using a Covap thermal evaporator by *Anstrom Engineering* where a tungsten boat was used as evaporation source. The zT measurement chip, developed by Linseis [22], consists of two Si_3N_4 membranes with a 100 nm thickness which allows full in-plain characterization of nano-scaled thin films. The deposition was carried out under vacuum with a pressure of 1×10^{-3} Pa, a rotation speed of 15 rpm, deposition rate of 1 Å s^{-1} and the set thickness of 400 nm. Due to the special setup of the measurement chip with two membranes, the deposition rate was considered rather low which results in a minimized thermal stress within the layer as well as between the layer and the substrate.

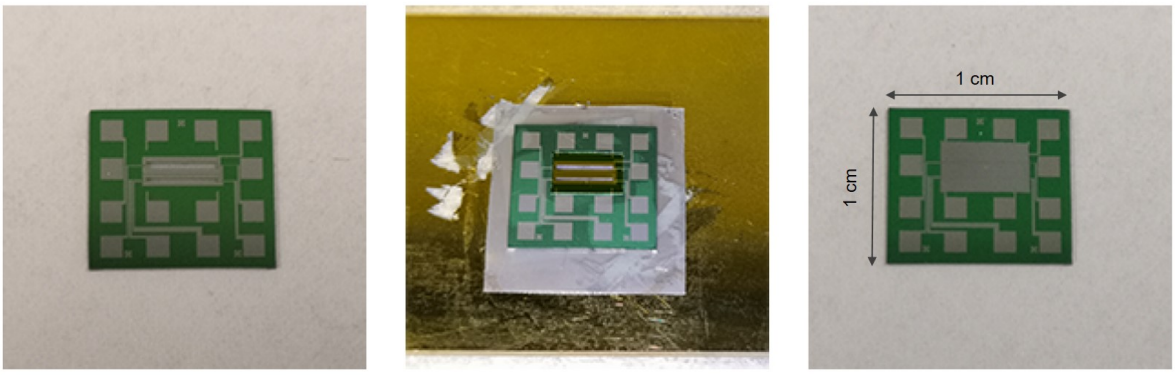

(a) Initial zT chip (b) Mask on the zT chip (c) Deposited zT chip

Figure 3.7.: (a) Initial zT chip before deposition, (b) zT chip covered with a transparent mask (c) zT chip with deposition of Sb [120].

Fig. 3.7 shows the steps of the Sb thin film deposition on the pre-structured measurement chip starting from the initial sample before the thermal evaporation deposition (a), then the partially covering the chip with mask (b) and finally the chip with the deposited Sb thin film (c). The initial chip was first cleaned and then carefully covered with a tape mask. Note, that the tape mask was applied in a way that allows the deposition on two membranes contacting four van der Pauw pads contacts Fig. 3.7 (b). Finally the deposition of the Sb thin film with a thickness of 382 nm on the unmasked chip was achieved using the above mentioned parameters (see Fig. 3.7 c). It is worth to mention that the parameter tooling factor plays an important role to control the deposition thickness. This factor relates the position of the evaporation source, the quartz micro valance and the sample. To assure a precise control on the thickness, these three positions must not be change.

3.4. Characterization

In this section, I introduce the characterization devices which were applied to determine TE properties of the TE materials used in this work. First, the commercial measurement system Dynacool is addressed as the main characterization device used for the electrochemically deposited thick films. It also provides one option for full zT characterization of bulk samples which was here used for $Co_{75}Ni_{25}$ bulk sample. Then, I give a short description of Linseis LSR-3, Linseis Thin Films Analyser (TFA) and Linseis Laser Flash Analyser (LFA) which were used to characterize the Sb bulk sample, thermally evaporated Sb thin film and $Co_{75}Ni_{25}$ bulk sample, respectively.

3.4.1. Quantum Design Dynacool

The full zT characterization was carried out in a Physical Property Measurement System (PPMS) Quantum Design Dynacool. The Dynacool provides electrical, thermal and magnetic measurements whilst controlling the temperature of the sample and the applied magnetic field. The Dynacool system is a closed cycle system in which a single two-stage pulse tube cryocooler is used for the superconducting magnet as well as the temperature control system. This provides a low vibration environment for measurement of sample. The Dynacool system comes equipped with a 9 T or 14 T conduction-cooled superconducting magnet system. Measurements of material properties such as electrical transport, thermal transport, specific heat and magnetic AC and DC can be performed in a temperature range of 1.9 K up to 400 K.

The system provides multiple possibilities to user, namely, Resistivity Option (RO), Electrical Transport Option (ETO), Horizontal Rotator Option and Thermal Transport Option (TTO). Depending on the desired characterization and the material being measured, an appropriate option and its according sample puck can be employed. TTO enables a simultaneous characterization of σ, α and λ as well as zT of a TE material with a size of few millimeter. Regarding TTO, the size of the sample being measured has to be defined in such a way, that the sufficient temperature gradient along the sample can be achieved. In this work, TTO was applied for the $Co_{75}Ni_{25}$ bulk reference sample. Hereby, the reference bulk sample was mounted in a special puck and subjected to a thermal pulse which was measured by recording its temperature and voltage. However, this option is not appropriate for TE characterization of thin and thick film materials, particularly for those synthesized by the ECD.

For the characterization of the electrochemically deposited $Co_{75}Ni_{25}$ and Sb within the transport device, the transport device was mounted to an electrical transport puck and connected to the external devices. The electrical transport puck has three channels each of which provides resistivity measurement in a standard 4-probe configuration. These three channels were bonded to the pre-structured pads on the transport device by means of wire.

Fig. 3.8 shows a close view of the transport device in a scanning electron microscopic (SEM) image, where the pre-structured pads were bonded to the channels on the puck. A top view of the sample located and bonded on the puck is also shown in the left side of the Fig. 3.8. I have used the external devices, namely, three DC sourcemeters (Keithley 2400) and four nanovoltmeters Keithley 2182A. DC sourcemeters were used to measure the heating power and the current of the Resistance Thermometer Detectors (RTDs). The thermo voltage between two RTDs and the drop voltage for the resistance measurement of the heating stripe and RTDs were measured using four nanovoltmeters.

Three configuration setups were applied to characterize the three main TE properties, σ, α and λ. In section 4.3, I explain more details about the heating stripe and RTDs used in each configuration setup.

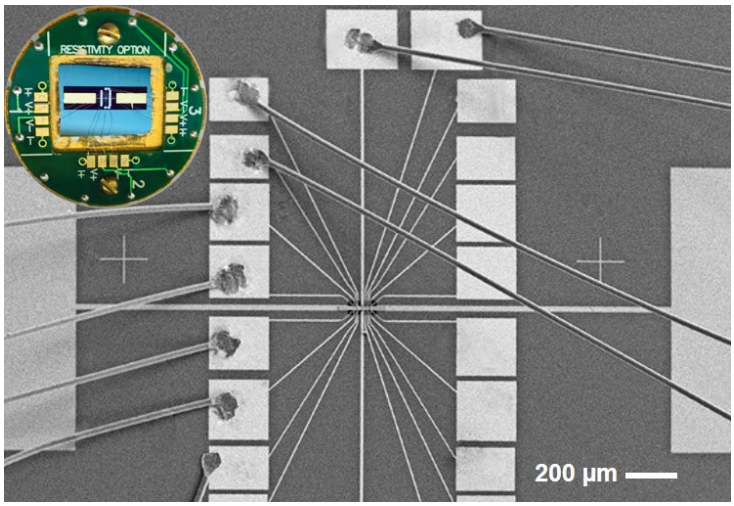

Figure 3.8.: An SEM image of the transport device placed and bounded in an electrical transport puck. The inset in the left side of the picture shows the puck with the bonded transport device.

3.4.2. Linseis LSR-3, TFA and LFA

The Linseis LSR-3 provides simultaneous measurements of the Seebeck coefficient and the electrical conductivity under inert atmosphere and a temperature range of 0 °C up to 500 °C. Using this device, bar samples with a length in the range of 6 mm up to 23 mm can be analyzed. Fig. 3.9 shows a schematic picture of the measurement principle of the Seebeck coefficient and the electrical conductivity. The LSR-3 enables the Seebeck measurement where a temperature gradient is generated along the height of the sample resulting in a thermo voltage (see Fig. 3.9 (a)). The temperature gradient ΔT as well as the generated thermo voltage V_{th} can be measured by two s-type thermocouples which were placed at two points on the sample. The relative α — determined by the thermo voltage divided by the temperature gradient — includes a combination of α of the sample and the thermocouples. Using a reference thermocouple with a known absolute α, it is possible to measure the releative α of the sample by subtracting α of the reference from the measured α.

To measure σ using LSR-3, a current was applied between the upper and the lower electrodes placed at the top and the bottom of the sample resulting in a potential between

the two thermocouples (see Fig. 3.9 (b)). Note, that the measurement has to be carried out under thermal equilibrium in order to avoid a Seebeck effect. The applied current has to be adjusted so that, on the one hand, it enables a sufficient signal for resistivity measurement, and on the other hand it keeps the temperature gradient generated by Peltier cooling and Joule heating between the thermocouples close to zero. σ can then be calculated knowing the area and the length of the sample between the thermocouples.

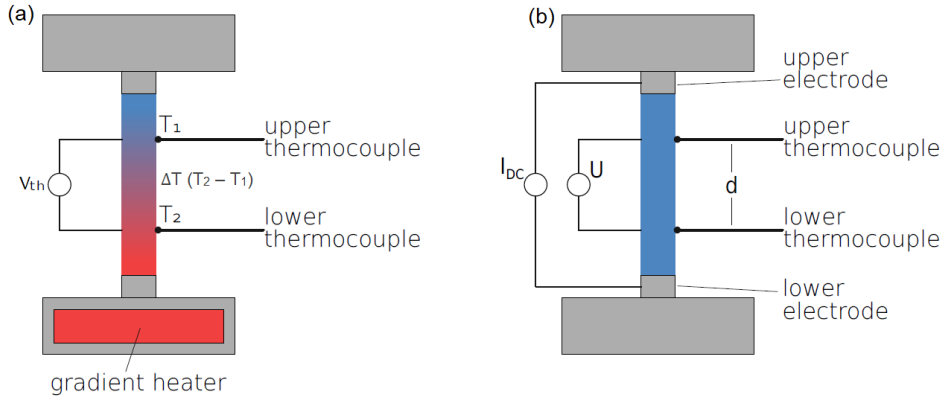

Figure 3.9.: Schematic pictures of measurement principle of Linseis LSR for (a) Seebeck coefficient (b) resistivity measurement [120].

The Linseis TFA is a chip based device which allows the measurement of the thermal conductivity, the electrical conductivity, the Seebeck coefficient, the specific heat and the Hall coefficient of a sample nearly simultaneously. That is to say that the characterizations are performed in one measurement run in order to avoid measurement errors which offers a great comparability of the measured values. Using this device, films from nm to µm range can be measured in a temperature range of 80 K up to 500 K and a magnetic filed up to 1 T. In this work, the Linseis TFA was applied to measure the TE properties of the thermally evaporated Sb thin film reference sample. The Sb thin film was prepared on the special pre-structured zT chip which was presented in subsection 3.3.2. For more details of the working principle of this zT chip, I refer readers to references [22, 29]

Linseis LFA provides the measurement of the thermal diffusivity D_{th} of the sample using a transient measurement technique. The measurements can be carried out under inert atmosphere or vacuum in a temperature range from room temperature up to 1250 °C. The sample is placed in a special sample holder which has a hole at its bottom and top sides. A laser pulse heats the sample through the bottom hole while the temperature of the sample can be measured through the top hole by the infrared detector located above the sample. The thermal diffusivity can then be obtained by fitting the measured temperature over time. The thermal conductivity can be calculated from $\lambda = D_{th} c_p \rho$ with the sample thickness, density ρ and the heat capacity c_p.

3.5. Simulation

In this section, a short description of Comsol Multiphyscis is introduced which was used to optimize and verify the fabricated transport device as well as to study the accuracy of the measurements achieved with the transport device. Optimization and simulation of TE effects can be done by various numerical and simulation methods. Comsol Multiphysics is a general-purpose finite element analysis software which is based on advanced numerical methods. It provides a finite element modeling and simulating of physics-based problems. Comsol Multiphysics is defined to solve complex problems with interactions between two or more modules of different physics. Applying this method, we can prospectively decrease the necessity for physical prototypes along with substantial saving in the development process and time. In this work, simulation approach was used in the following cases and scenarios

(a) Testing and validation of the fabricated transport device

- Analysis of temperature distribution
- Analysis of the accuracy of the 1D analytical approach for the thermal conductivity measurements

(b) Study of parasitic heat losses

- Define the thickness of the resistance thermometers
- Define the range of thicknesses and thermal conductivities of TE material

(c) Define and optimization of a µTEG

For a TE analysis, the heat transfer and electric current modules are applied which can be simultaneously coupled by TE effects to find solutions for Peltier, Seebeck and Thomson effects. To analyze Seebeck and Peltier effects, there are two governing equations $\overrightarrow{J_Q}$ and $\overrightarrow{J}$ for the heat and electric current flux which were described in section 2.1 in the framework of the Onsager equations.

By substituting $\overrightarrow{J_Q}$ and $\overrightarrow{J}$ and considering $\overrightarrow{E} = -\overrightarrow{\nabla}V$ in the heat energy balance $\overrightarrow{\nabla}.\overrightarrow{J_Q} + \overrightarrow{E}.\overrightarrow{J} = 0$ and the charge density conservation $\overrightarrow{\nabla}.\overrightarrow{J} = 0$, a system of coupled TE field equations is described by the following partial differential equations (PDE) [121, 122]:

$$-\overrightarrow{\nabla}((\sigma\alpha^2 T + \lambda)\overrightarrow{\nabla}T) - \overrightarrow{\nabla}(\sigma\alpha T\overrightarrow{\nabla}V) = \sigma((\overrightarrow{\nabla}V)^2 + \alpha\overrightarrow{\nabla}T\overrightarrow{\nabla}V), \tag{3.7}$$

$$\overrightarrow{\nabla}(\sigma\alpha\overrightarrow{\nabla}T) + \overrightarrow{\nabla}(\sigma\overrightarrow{\nabla}V) = 0. \tag{3.8}$$

Depending on the experimental setup and the desired simulation, specific boundary conditions including applied current, temperature and voltage are considered. The simulation of the fabricated transport device is shown and discussed in chapter 5. The optimization of a µTEG is discussed in chapter 7.

4. Fabrication of the Transport Device

In this chapter, the development of the transport device is presented based on a variety of different micro-structuring techniques in combination with etching processes which were described in chapter 3. The organization of this chapter is the following. In section 4.1, the conceptual approach of the device is introduced which is needed for a clearer understanding of the idea behind the development. Then I show the fabrication line and processing steps of the transport device along with the treatments and techniques in section 4.2. In section 4.3, characterization methods are introduced through which one can evaluate electrical conductivity σ, Seebeck coefficient α and thermal conductivity λ within the transport device. Finally, I conclude the results in section 4.4.

4.1. Conceptual Approach

The conceptual approach to develop the transport device for characterization of electrochemically deposited TE materials is focusing on two goals: first, eliminating the influence of the substrate and the conductive seed layer to avoid the falsification of the data. Second, the determination of TE and transport properties of electrochemically deposited TE materials on one single sample.

A schematic top view of the transport device with a detailed view of its center region is shown in Fig. 4.1. The device consists of a Si_3N_4 membrane structured in its center on which an electrically conductive seed layer, a heating stripe and four electrodes were patterned. An electrically conductive seed layer was needed in order to synthesize the TE material using ECD technique. The heating stripe placed in the center of the membrane was partly covered with SiO_2 layer. Four electrodes were structured symmetrically on both sides of the heating stripe which serve as RTDs. The TE material was deposited by ECD technique on the rectangular cavity which was patterned on the center of the membrane. Finally, to complete the transport device and to obtain a suspended TE material, the Si_3N_4 membrane and seed layer were removed from the backside of the transport device by RIE followed by wet chemical etching processes. This configuration enables the simultaneous characterization of the in-plain σ, α and λ of an electrochemically deposited TE-material.

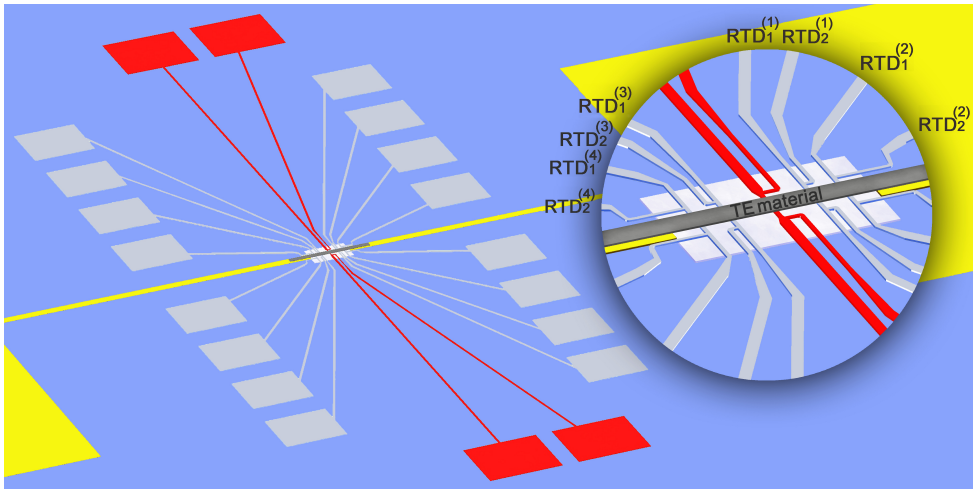

Figure 4.1.: A top view of the transport device with an inset of its center including a heating stripe (red), four electrodes (light gray), the electrically conductive seed layer Au (yellow) and the TE material (dark gray).

4.2. Fabrication line

Fig. 4.2 represents the sequential process flow for the fabrication of the transport device. To get a better insight of the fabrication line, I divide it into three major parts each of which includes specific treatments including photolithography, pre-structuring and etching process. For more details about the applied parameters in each step such as temperature, backing time and pressure, I refer readers to the supporting material A of this thesis.

In the first part (see Fig. 4.2 a-c), the preparation of a Si_3N_4 membrane on the Si substrate is explained followed by RIE of Si_3N_4 layer and chemical etching of Si substrate. In the second part (see Fig. 4.2 d-f), the structuring of a conductive seed layer and RTDs on the pre-structured membrane are discussed. In the last part (see Fig. 4.2 g-i) the finalization of the transport device after ECD of the TE material is described.

4.2.1. Preparation of the Membrane

As it was discussed earlier, the goal was the characterization of the TE material while removing the impact of the seed layer and the substrate. To achieve this, a suspended membrane within a defined cavity was desirable to remove the impact of the substrate. The conductive seed layer was as well etched away using an appropriate etchant which was applied in the cavity.

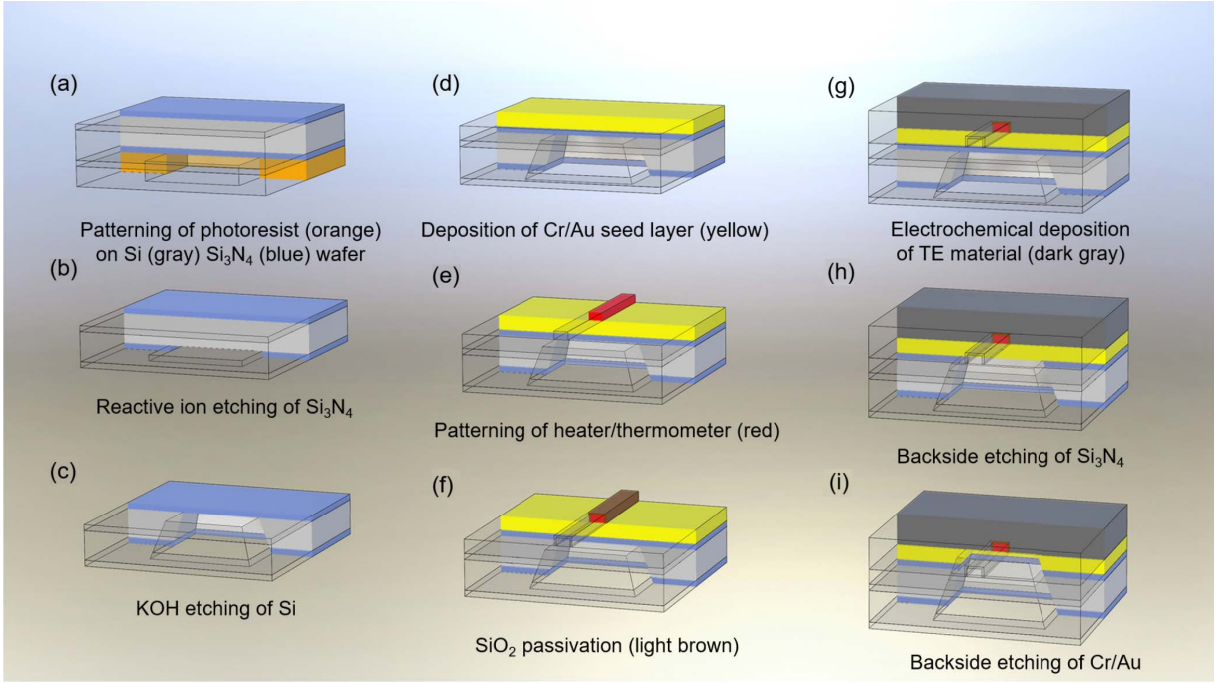

Figure 4.2.: Schematic process flow showing the fabrication of the transport device. (a) patterning of the photoresist (orange) on a Si_3N_4 (blue) coated Si (gray) substrate, (b) removing the Si_3N_4 layer by RIE, (c) anisotropically etching of Si by KOH etching, (d) Sputtering of the Cr/Au adhesion and seed layer (yellow), (e) patterning of the heating stripe and the RTDs (red), (f) protecting of the heating stripe by a dielectric layer SiO_2 layer (light brown), (g) ECD of the TE material (dark gray), (h) backside etching of the Si_3N_4 and (i) wet chemical etching of the Cr/Au adhesion and seed layer.

Hence, the starting point of the development was the structuring of a Si_3N_4 membrane within a defined window on a substrate. The size of the membrane was chosen in a way that, on the one hand, it enables a symmetric patterning of other layers including a seed layer, a heating stripe, four RTDs and the TE material, and on the other hand, it was adjusted to the mask window on the backside of the Si substrate. I used a Si substrate (gray) of 300 µm thickness with a 100 nm Si_3N_4 (blue) on both sides, since it fulfills the requirements for getting a suspended membrane using a wet and dry etching of Si and Si_3N_4, respectively.

For this purpose, the following treatments need to be done on the backside of the Si substrate: photolithographic structuring to pattern a window, RIE of Si_3N_4 and wet KOH etching of Si (see Fig. 4.2 a-c). First, a rectangular window of $520 \times 460\,\mu m^2$ was patterned on the backside of the Si through photolithography (photoresist application,

exposure and development) (see Fig. 4.2 a). Note, that the size of the window was adjusted to the achieved membrane on the front side of the substrate according to wet anisotropic etching of Si (see subsection 3.1.3). Hereafter, Si_3N_4 was etched from the uncovered window using RIE applying precursor gases O_2 and CHF_3 (see Fig. 4.2 b).

After etching of the Si_3N_4 layer from the window and removing the photoresist, Si etching process can be started. Si was anisotropically etched from the window using an aqueous KOH solution, until the Si_3N_4 layer on the front side of the substrate was reached (see Fig. 4.2 c). This results in a free standing Si_3N_4 membrane of $100 \times 40\,\mu m^2$ on which a seed layer, other RTDs and the TE material were structured (see Fig. 4.2 c).

4.2.2. Structuring of the Seed Layer and RTDs

The second part of the development was the patterning of the conductive seed layer, the RTDs and the passivation layer SiO_2 on the the front side of the free standing Si_3N_4 membrane (see Fig. 4.2 d-f). The lift-off processes (see subsection 3.1.1) were employed for the structuring of the conductive seed layer as well as the heating stripe and the RTDs while the passivation layer of SiO_2 was prepared in an etching process (see subsection 3.1.1). Deposition of the conductive seed layer on the front side of the membrane was the first step of the second part. Hereby, a 10 nm Cr and a 150 nm Au as adhesion and seed layer were sputtered on the pre-structured Si followed by a lift-off process (see Fig. 4.2 d). This results in an Au stripe (yellow) in the center of the membrane which was extended to the corner of the Si substrate to provide enough contact pads for ECD process.

Hereafter, the second layer comprising of the heating stripe, four RTDs and the contact pads were sputtered by a 10 nm Ti and 400 nm Pt as adhesion and contact layer in a lift-off process. Fig. 4.2 (e) represents solely the heating stripe (red) in the center of the membrane where four RTDs were symmetrically placed on its both sides.

Before continuing with the ECD of the TE material, it is necessarily needed to isolate the heating stripe individually from the upcoming TE material, avoiding an electrical short-circuit. Therefore, a 50 nm SiO_2 layer was deposited by ALD on the whole substrate which served as electrical insulation between the heating stripe and the TE material. For later electrical contacting and ECD, the SiO_2 was removed from the RTDs, the seed layer and the contact pads using photolithographic process in combination with RIE (see Fig. 4.2 f). A detailed description of the applied parameters through photolithographic structuring and RIE is given in the supporting material A.

4.2.3. TE-Material Deposition and Finalization of the Device

(Fig. 4.2 g-i) show schematically the finalization of the transport device including, the ECD of the TE material, etching of the Si_3N_4 membrane using RIE and wet chemical etching of the Cr adhesion layer and Au seed layer. The ECD of the TE material was carried out in a rectangular cavity on the pre-structured transport device which acts as working electrode in the ECD technique. The following treatments need to be done to deposit the TE material: photolithography to structure of a cavity of $200 \times 20\,\mu m^2$ on the Au stripe on the center of the membrane, RIE using O_2 to remove the residual photoresist and to activate the Au layer before starting the ECD and performing of the ECD under potentiostatic or galvanostatic conditions in a two or three electrodes configuration.

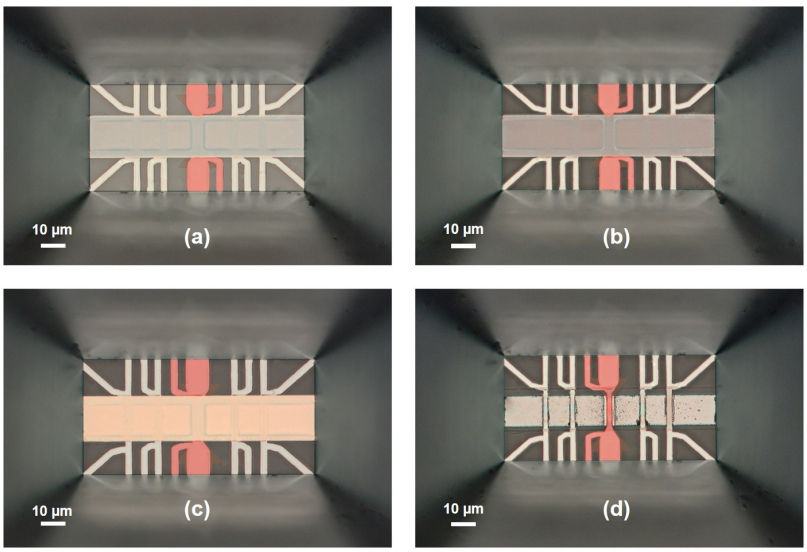

Figure 4.3.: Optical microscope images of the backside of the transport device in etching process (a) the initial transport device before backside etching, (b) RIE of the Si_3N_4 membrane, (c) wet chemical etching of the Cr adhesion layer, (d) wet chemical etching of the Au seed layer.

The thickness of the TE material was chosen in such a manner that, on the one side, the passivated heating stripe was covered by the TE material. And on the other side, to adjust the thermal conductance of the TE material to stay within a measurement error of 10 %. More details regarding the thickness and thermal conductivity measurement is discussed in chapter 5.

To finalize the device, the Si_3N_4 layer, the Cr/Au adhesion and seed layer were etched from the backside of the device. To protect all components on the front side of the device

against backside etching processes, a thick photoresist AZ9260 was used. Fig. 4.2 (h) and (i) show schematically the finalization of the transport device. First, the Si_3N_4 membrane was etched from the backside using RIE applying precursor gases O_2 and CHF_3. Hereafter, I etched the Cr and Au layer by dipping the device in TechniEtch Cr01 and KI/I_2 etchant solutions, respectively.

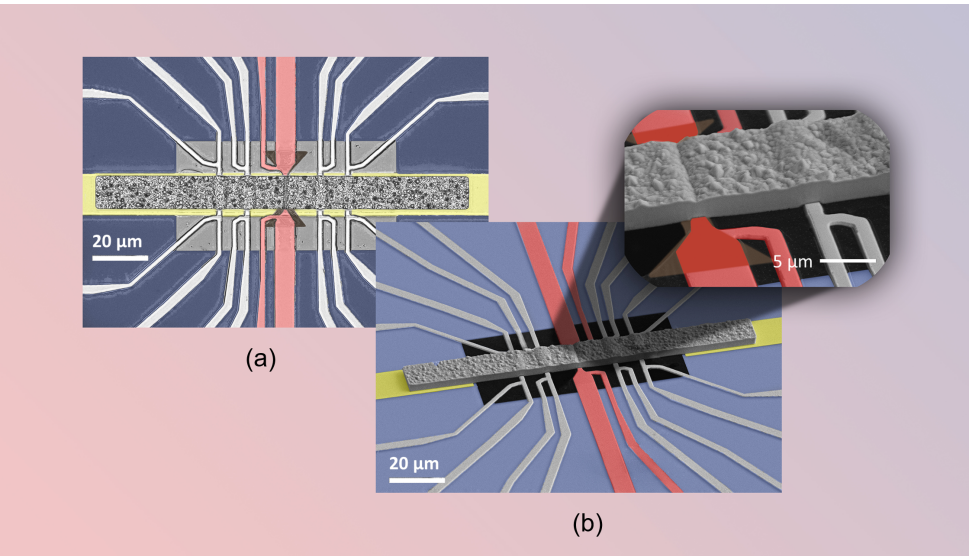

Figure 4.4.: (a) An optical microscope image top view of the transport device before backside etching, (b) an SEM image top view of the transport device after backside etching. The inset in the center shows a nice view of the heating stripe with the SiO_2 passivation and the the TE material.

Fig. 4.3 shows optical microscope images of the backside etching of the transport device step by step, starting from the initial device (a), RIE of the Si_3N_4 layer (b), etching of the Cr layer (c) to remove the Au layer (d). More details of the initial device (before backside etching) can be seen in an optical microscope image of its front side (Fig. 4.4 (a)), where the membrane and the Au seed layer were still there. As a result of the etching process, the free standing heating stripe (red), the RTDs (light gray) and the deposited TE material (dark gray) on top of the membrane were revealed. Fig. 4.4 (b) shows an SEM image of the finalized transport device after backside etching, where the suspended TE material can be well identified. I used the color codes in optical microscope and SEM images in order to recognize the different materials and functionalities within the device and to enable a direct comparison with the schematic pictures. It is worth to mention, that the dimension of the SiO_2 layer on the heating stripe was chosen in such a manner that it allows the deposition of the TE material across the small passivated section building a dell at the intersection area [111].

4.3. Characterization Procedure

In this section, a detailed description of the characterization techniques within the transport device is presented which were applied to determine the TE material properties. For the characterization of each parameter, a defined configuration setup was used. As it was discussed in the conceptual approach, four RTDs were placed symmetrically on both sides of the heating stripe which make the characterization on each side possible.

4.3.1. Electrical Conductivity Characterization

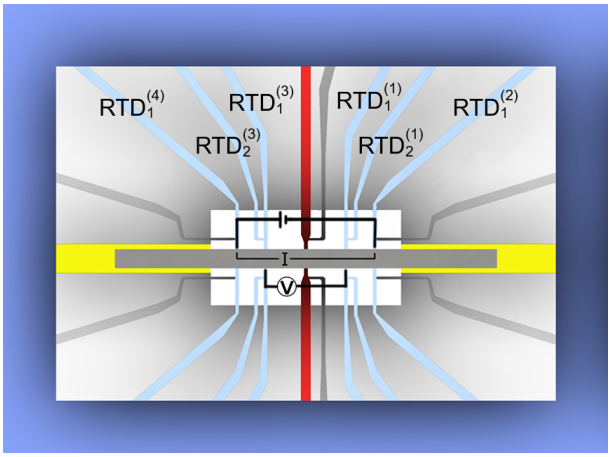

Figure 4.5.: A schematic top view of the contact configuration for electrical conductivity measurement.

σ of the sample can be determined in a common 4-point probe configuration. The measurement relies on four contact resistances or RTDs on the sample. In this configuration, a current was passed through the sample using two outermost contacts while the voltage drop was measured between the two inner contacts. Hereby, four RTDs on both sides of the heating stripe were used. Fig. 4.5 represents the applied contact configuration setup for the measurement of σ. The voltage drop was measured between RTD$_1^{(3)}$ and RTD$_1^{(1)}$ when a current I_{4p} was applied between the contacts RTD$_1^{(4)}$ and RTD$_1^{(2)}$. σ can then be defined by:

$$\sigma = L_{4p} R_{4p}^{-1} A^{-1}, \tag{4.1}$$

where $R_{4p} = V_{4p} I_{4p}^{-1}$ denotes the resistance, L_{4p} denotes the distance between the voltage probes and A is the cross section area of the TE material.

4.3.2. Seebeck Coefficient Characterization

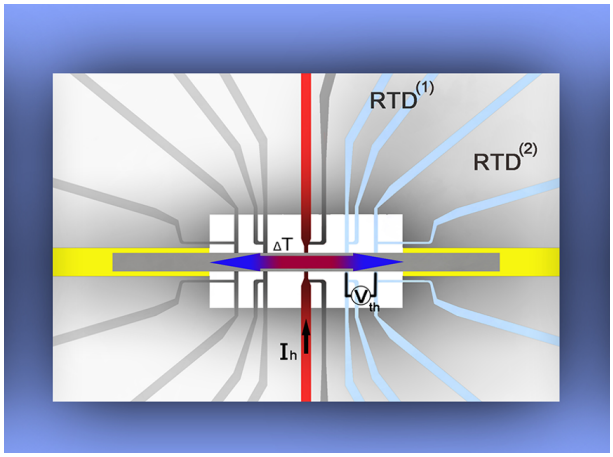

Figure 4.6.: A schematic top view of the contact configuration for Seebeck measurement.

To measure α, a temperature gradient has to be created between two RTDs resulting in a thermo voltage between the same RTDs. Hence, the heating stripe in the center of the membrane and two RTDs were used (see Fig. 4.6). By applying an electrical current I_h through the heating stripe, a temperature gradient was generated along the sample from the heating stripe to both edges of the surrounding Si. Si substrate serves as heat sink which corresponds to the ambient temperature T_0 , RTD$^{(1)}$ and RTD$^{(3)}$ close to heating stripe serve as hot contacts and RTD$^{(2)}$ and RTD$^{(4)}$ located near the edge of the surrounding Si act as cold contacts.

Considering RTD$^{(1)}$ as hot and RTD$^{(2)}$ as cold contacts, α can then be evaluated as follows:

$$\alpha = \frac{-V_{th}}{T_{hot} - T_{cold}}, \tag{4.2}$$

where T_{hot} is the temperature of RTD$^{(1)}$, T_{cold} is the temperature of RTD$^{(2)}$ and V_{th} is the thermo voltage between RTD$^{(1)}$ and RTD$^{(2)}$. The V_{th} can be directly determined whilst the temperature difference $T_{hot} - T_{cold}$ was evaluated through the temperature increase of each thermometer. Consequently, the temperature increase of each thermometer can be measured evaluating its resistance increase $R(T) - R(T_0)$ regarding the ambient temperature T_0 in a 4-point probe configuration as follows [20, 123]:

$$R(T) - R(T_0) = m(T - T_0) = \beta R(T_0)(T - T_0). \tag{4.3}$$

Where β denotes the temperature coefficient of the resistance and $m = dR/dT$ denotes the

slope of the resistance-temperature curve. These two values β and m were calibrated when no current was applied to the heating stripe and the device was in a thermal equilibrium.

4.3.3. Thermal Conductivity Characterization

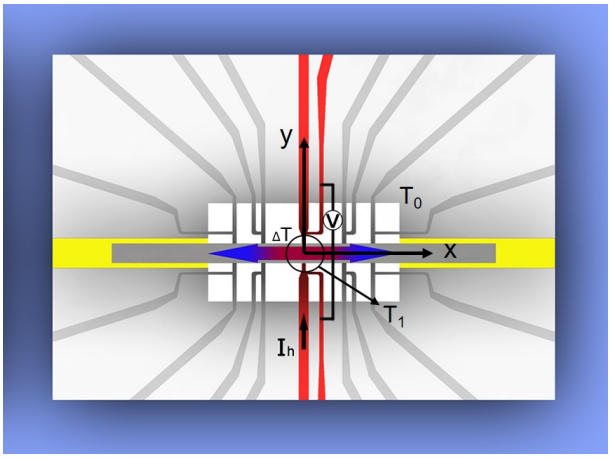

Figure 4.7.: A schematic top view of the contact configuration for thermal conductivity measurement.

The in-plane λ was measured using a steady-state method when an established temperature difference along the material was constant with time. Hereby, the temperature difference and the generated heat power along the material need to be defined. To provide conditions for a 1D heat conduction through material, it is required to ensure that parasitic heat losses are minimized. Parasitic heat losses consist of heat conduction and radiation along the length direction of the heating stripe and the RTDs, heat convection and radiation losses to ambient. Heat losses through the the heating stripe and the RTDs by both, heat conduction and radiation were minimized by decreasing their cross section area using advanced micro- and photolithographic structuring. Heat losses to ambient can be minimized by considering a vacuum condition for measurements.

Fig. 4.7 shows a schematic top view of the configuration setup for λ measurement. By applying a current I_h through the heating stripe, a heating power P is dissipated in the heating stripe. The heating power results in a temperature gradient along the sample from the heating stripe to the Si substrate (heat sink). Due to the symmetry of the device, I considered half of P on each side of the heating stripe. The thermal conductance K of the material can then be determined as fallows:

$$K = \frac{P/2}{\Delta T}, \tag{4.4}$$

where $\Delta T = T_1 - T_0$ denotes the temperature difference from the heating stripe to the edge of the heat sink, T_1 denotes the temperature of the heating stripe and T_0 denotes the temperature of the heat sink which corresponds to the ambient temperature, respectively. $P = RI_h^2$ can be determined from the electrical resistance R of the heating stripe and the applied I_h.

I start first with ΔT and show how to obtain it along the sample in x-direction (perpendicular to the heating stripe). Hereby, three approaches, namely analytical, simulation and experimental were applied. The analytical approach was determined by 1D steady state heat equation which contains the contribution of heat conduction $\dot{Q_C}$, radiation $\dot{Q_R}$, and convection. Note, that the characterization was carried out under vacuum (pressure $<10^{-5}$ mbar) in order to minimize heat losses, so that I do not have to account for convection. ΔT was calculated in steady state considering the stationary heat balance equation using following equation:

$$\dot{Q_R} - \dot{Q_C} = 0. \tag{4.5}$$

$\dot{Q_R}$ of the sample for a volume element Adx is given by Stefan-Boltzmann law:

$$\dot{Q_R} = \sigma_B(T(x)^4 - T_0^4)[(2b + 2d)\varepsilon]dx, \tag{4.6}$$

where σ_B denotes the Stefan-Boltzmann constant, ε denotes the emissivity, d denotes the thickness and b denotes the width of the TE material, respectively. Considering small changes in temperature where $(T(x) - T_0)T_0^{-1} \ll 1$, the Stefan-Boltzmann can be approximated linearly by Eq. 4.7.

$$T(x)^4 - T_0^4 \approx 4T_0^3\Delta T(x), \tag{4.7}$$

and by substituting Eq. 4.7 in Eq. 4.6, $\dot{Q_R}$ is achieved as follows:

$$\dot{Q_R} = 4\sigma_B T_0^3 \Delta T(x)[(2b + 2d)\varepsilon]dx. \tag{4.8}$$

$\dot{Q_C}$ in the sample is defined as follows:

$$\dot{Q_C} = -(\lambda d)b\frac{d^2\Delta T(x)}{dx^2}dx. \tag{4.9}$$

The 1D heat balance equation 4.5 can then be written as:

$$4\sigma_B T_0^3 \Delta T(x)[(2b + 2d)\varepsilon] - (\lambda d)b\frac{d^2\Delta T(x)}{dx^2} = 0, \tag{4.10}$$

or in the usual form

$$\frac{d^2\Delta T(x)}{dx^2} - \mu\Delta T(x) = 0, \tag{4.11}$$

with definition of μ

$$\mu = \frac{4\sigma_B T_0^3[(2b+2d)\varepsilon]}{(\lambda d)b}. \tag{4.12}$$

ΔT along the TE material in x direction can then be obtained by taking the boundary conditions into account. Defining the origin of x-y coordinate system in the center of the membrane (see Fig. 4.7), the first boundary condition is defined on the heat sink, $\Delta T(x = L) = 0$. The second boundary is defined at the position of the heating stripe, $\Delta T(x = 0) = T_1 - T_0$.

Eq. 4.11 can be solved considering these two boundary conditions which results in ΔT in x direction as

$$\Delta T(x) = (T_1 - T_0)\frac{sinh(\sqrt{\mu}(L-x))}{sinh(\sqrt{\mu}L)}. \tag{4.13}$$

Along with the 1D analytical approach, a 3D finite element method simulation was carried out using Comsol Multiphysics. The simulation was performed by using the heat transfer and AC/DC modules with specific boundary conditions dedicated to the experimental setup. For more details about on how the simulation was done, I refer readers to the chapter 5 which is specifically devoted to the validation of the transport device.

Fig. 4.8 represents the temperature distribution depending on the position x (ranging from the heating stripe position ($x = 0$) up to the heat sink ($x = L$)) employing different approaches. The first approach is to use the above analytical approach (see Eq. 4.13) which is shown in Fig. 4.8 with the solid green line. Interestingly, the distribution at the specified range of x is highly linear considering an emissivity of 0.8 to study the influence of the radiation loss assuming a worst-case scenario. The inset in Fig. 4.8 shows the deviation of the analytical results calculated for an emissivity of 0 and 0.8 which confirms that the radiation contribution of the TE material is negligible. The second approach is the 3D simulation model, which shows as well a linear distribution along the sample (the solid and dotted blue line) and it is in a good agreement with the 1D analytical approach. More discussions about the simulation approach and the deviation between the simulated ΔT at the bottom and top of the sample will be presented in chapter 5.

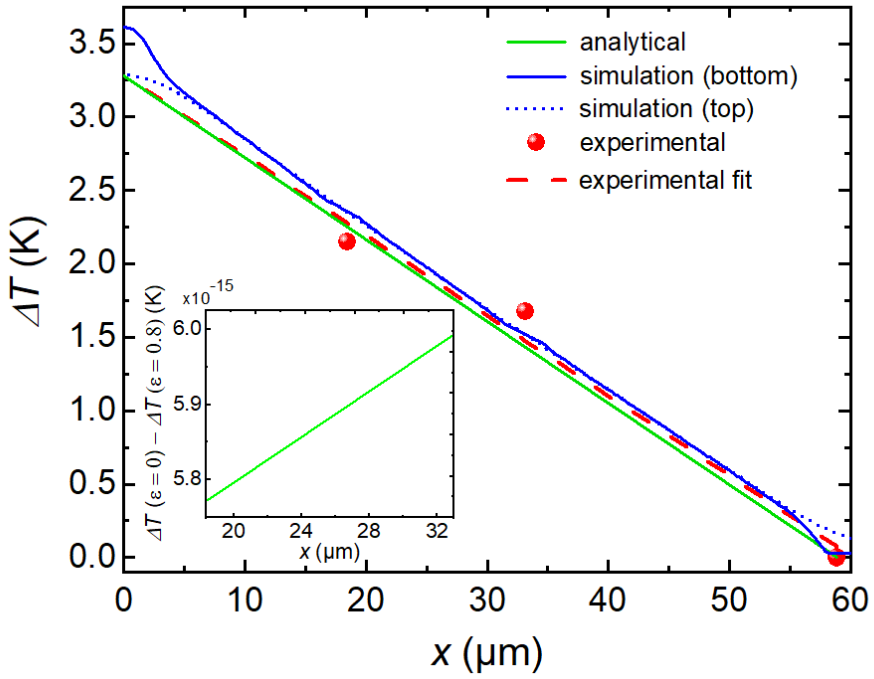

Figure 4.8.: The behavior of the temperature distribution depending on the position x starting at the position of heater (x=0) up to the heat sink at the position (x=L) for analytical (green), simulation (blue) and experimental (red) model. The dashed red line shows the fitted line to experimental data.

Based on the linearity assumption of ΔT validated analytically and by simulation, ΔT along the sample can be defined by a linear fit to the experimental data (the red points) which is also shown in Fig. 4.8 with the dashed red line. There are three experimental data points corresponding to three x positions: the measured temperature of $\text{RTD}^{(1)}$ and $\text{RTD}^{(2)}$ as well as the ambient temperature T_0. The temperature of each RTD was calculated by evaluating its resistance increase described previously in subsection 4.6. The linear fit is very consistent with experimental data as well as the hyperbolas of the analytical and simulation results. Therefore considering the extrapolated temperature produced from this fit is a valid assumption as the heating stripe temperature, T_1.

To calculate λ of the TE material, in addition to ΔT, P has to be also obtained. P comprises radiation and conduction contributions. Because of the small dimension of the heating stripe compared to that of the TE material, the heat losses of the heating stripe by conduction and radiation contributions are small and can be neglected. The radiation loss of the TE material is negligible as discussed before. So P at the position of the

heating stripe ($x = 0$) can then be written as following:

$$P = -A\lambda \frac{d\Delta T(x)}{dx}\bigg|_{x=0} \tag{4.14}$$

where A denotes the cross section ($b \times d$). Using $\Delta T(x)$ from equation 4.13, P at $x = 0$ is given by

$$\begin{aligned} P = A\lambda(T_1 - T_0)\frac{\sqrt{\mu}cosh(\sqrt{\mu}L)}{sinh(\sqrt{\mu}L)} = \\ A\lambda(T_1 - T_0)\sqrt{\mu}coth\sqrt{\mu}L. \end{aligned} \tag{4.15}$$

This shows a linear behavior of P in terms of $T_1 - T_0$ that can be used to evaluate λ. Considering the first order of the Tylor series approximation around $\mu \longrightarrow 0$ (due to the small radiation contribution of the TE material) for P and taking into account that the heating power is equally distributed on each side of the heating stripe, λ of the TE material can then be calculated by:

$$\lambda = \frac{PL}{2A(T_1 - T_0)}. \tag{4.16}$$

Using the developed transport device and the defined measurement procedure, I studied the temperature dependent transport properties of two TE thick films which are shown and discussed in chapter 6.

4.4. Summary

In this chapter, the development of the transport device was illustrated which was fabricated based on a series of treatments and technologies including, microstructuring, sputtering and chemical etching processes. It was started with the definition of the conceptual approach focusing on two subjects: first, removing the impact of the substrate as well as the seed layer. Second, the simultaneous characterization of the transport properties on one single sample. To give a more detailed image of the progression of the device, the fabrication line was divided into three main parts: (1) preparation of the membrane (2) structuring of the electrically conductive seed layer together with the resistance thermometers and (3) the deposition of the TE material along with the finalization of the device. To finalize the device, the Si_3N_4 membrane and the conductive seed layer were properly etched from the backside of the device resulting in a suspended TE material.

Additionally, the characterization procedure within the transport device was shown and explained along with the configuration setup and the used equations for each transport parameter. Electrical conductivity was measured in a four point configuration passing a current through the material using two outermost thermometers and measuring the drop voltage between two other inner thermometers. Seebeck coefficient was defined using a partly passivated resistance thermometer which acts as heating stripe and two other thermometers as hot and cold contacts. For the thermal conductivity measurement, a 1D steady state method was applied considering the realistic boundary conditions. Hereby, a current was passed through the heating stripe resulting in a temperature gradient along the sample from the heating stripe to the substrate. The heating power dissipated into the material was determined by the electrical resistance of the heating stripe and the applied current.

5. Validation of the Transport Device

This Chapter is devoted to the 3D simulation of the transport device using Comsol Multiphysics. Two objectives are to be investigated: first, to verify the 1D analytical approach which was used for the thermal conductivity measurement and second, to study the accuracy of the measurement and parasitic heat losses dissipated through the heating stripe and RTDs.

The outline is as follows: First, in section 5.1, the geometry of the device and the specific boundary conditions dedicated to the experimental setup are introduced. Then, the validation of the thermal conductivity measurement is shown using 3D simulation through study of the temperature distribution along the TE material. The accuracy of the measurement along with the measurement error due to parasitic heat losses is explained in section 5.2. Here, the range of thicknesses and thermal conductivities of TE materials are identified which can be characterized using the developed transport device. Finally, I summarize and conclude the results in section 5.3.

5.1. 3D-Simulation Model

The simulations were performed using Comsol Multiphysics applying heat transfer and electric current modules which can be linked through TE effects. These two modules solve the governing equations (see section 3.5). Fig. 5.1 (a) shows a 3D plot of the model geometry where a free standing TE material was placed on the heating stripe and four RTDs located symmetrically on both sides of the heating stripe. Two boundary conditions were chosen dedicated to the experimental setup, including ambient temperature T_0 and the temperature of heating stripe T_1. The first one was devoted to the Si substrate which acts as heat sink with a fixed temperature of $T_0 = 300\,\mathrm{K}$ and the second one was defined by an electric current I_h applied to the heating stripe. An adjusted I_h was passed through the heating stripe which generates a T_1 at the position of the heating stripe. Table 5.1 shows a summary of the materials and their according TE properties used in the simulations. To study the validation of the 1D analytical approach, the heat flow and the temperature distribution through the sample, I have characterized $Co_{75}Ni_{25}$ in the simulation.

Table 5.1.: Summary of the applied parameters used in Comsol simulation, including the dimension of each component and TE material properties (a) Values taken from COMSOL Multiphysics database. (b) Values taken from the experimental measurement of $Co_{75}Ni_{25}$ thick film. (c) Measured values of a Pt thin film.

Material	σ $(10^6\,\mathrm{S\,m^{-1}})$	α $(\mu\mathrm{V\,K^{-1}})$	λ $(\mathrm{W\,m^{-1}\,K^{-2}})$
Au	45.6 $^{(a)}$	6.5 $^{(a)}$	317 $^{(a)}$
Pt	6 $^{(c)}$	0 $^{(a)}$	40 $^{(c)}$
Si	10^{-12} $^{(a)}$	Electrically isolated	130 $^{(a)}$
Si_3N_4	Electrically isolated	Electrically isolated	20 $^{(a)}$
SiO_2	Electrically isolated	Electrically isolated	1.4 $^{(a)}$
$Co_{75}Ni_{25}$	8.26 $^{(b)}$	-24.3 $^{(b)}$	54 $^{(b)}$

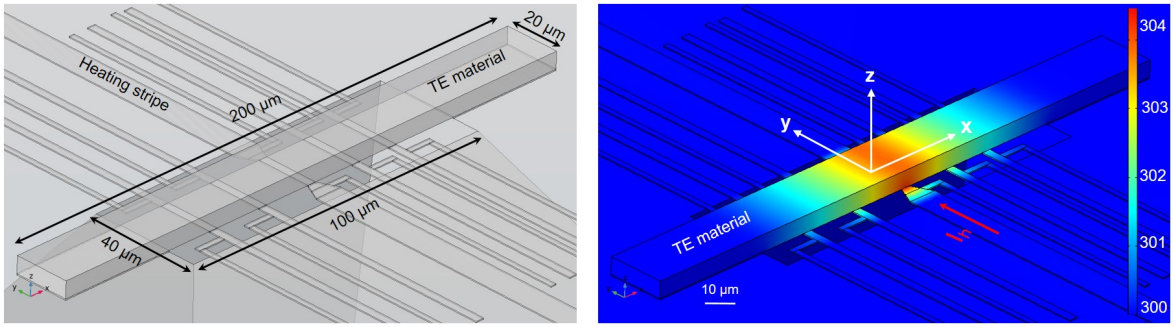

Figure 5.1.: (a) A 3D model of the transport device along with the used geometry for the simulation (b) a 3D plot of the steady state temperature distribution through the sample at the ambient temperature of $T_0 = 300\,\mathrm{K}$ and an applied electric current of $I_h = 16\,\mathrm{mA}$.

An overview of the steady state temperature was shown in Fig. 5.1 (b). The simulation presents spreading of the temperature through the material at the position of the heating stripe up to the heat sink position. The geometry of the heating stripe was chosen in such a way that the maximum power was mostly generated at the position of the heating stripe underneath the TE material, i.e. the resistance of the heating stripe underneath the TE material was increased. To achieve this, the cross section of the heating stripe underneath the TE material was reduced while at the edges of the material was increased though a trapezoid surface.

To verify the 1D analytical approach applied for the thermal conductivity measurement, the temperature distribution along the sample was studied. Defining the origin of the x-y coordinate system in the center of the membrane (see Fig. 5.1 (b)), the temperature distribution ΔT depending on the position x at the bottom and top of the sample is shown in Fig. 4.8. Based on the simulation approach, ΔT along the sample shows a linear behavior which is in a good agreement with the 1D analytical approach discussed in section 4.3.3. This indicates that heat is mostly transferred by conduction and contribution of the radiation heat loss can be completely disregarded. For the simulation, an emissivity of 0.8 for TE material was applied to study the influence of the radiation on the measurement.

There are several remarks in Fig. 4.8 worth noting. $\Delta T(x)$ at the bottom of the sample presents a small deviation from the linear behavior at $x = 0$. This is due to the heat flow in z-direction which was not taken into account in the 1D analytical approach. This only influences the direct surrounding of the heating stripe, i.e. a few micrometers away from the heating stripe $\Delta T(x)$ along the sample is homogenized. This homogenization can be seen in Fig. 4.8 at the top of the sample which does not depend on the z-direction. There are also two kinks in the simulation plot presenting $\mathrm{RTD}^{(1)}$ and $\mathrm{RTD}^{(2)}$ which match the experimental positions (red points in Fig. 4.8). The experimental point at the position $x = 60\,\mu\mathrm{m}$ shows the temperature of the heat sink T_0.

5.2. Heat Loss Analysis

This section is devoted to the study of parasitic heat losses through the heating stripe as well as four RTDs contacts. This especially helps to identify the range of material parameters and film thicknesses that can be characterized using the transport device. The thickness and thermal conductivity of the TE material as well as the heating stripe and RTDs contacts contribute significantly in the design, fabrication and validation of the transport device to increase the accuracy of the measurements.

The heating stripe and RTDs possessed the same thickness which was selected in such a way that the dissipated heat loss through them is at least by a factor of 10 smaller than the heat conducted in the material. This was validated by 3D simulations which were carried out through varying the thickness of the heating stripe as well as RTDs ranging from 300 nm to 700 nm. Hereby, the dissipated heat $\dot{Q}$ through each RTD and the heating power P generated in the heating stripe were obtained by FEM simulation. Considering half of the power going through one side of the device due to its symmetry, the heat loss is defined as $2(\dot{Q}_1 + \dot{Q}_2)/P$, where $\dot{Q}_1$ ($\dot{Q}_2$) is the dissipated heat through $\mathrm{RTD}^{(1)}$ ($\mathrm{RTD}^{(2)}$). Table 5.2 represents the obtained P by simulation, the thickness of RTDs, the dissipated heats $\dot{Q}_1$ and $\dot{Q}_2$ and the heat loss in (%) for a fixed $\lambda_{TE}^{sim} = 54\,\mathrm{W\,m^{-1}\,K^{-1}}$.

Table 5.2.: Summary of the heating power P, different thicknesses of RTDs and the heating stripe, the dissipated heat $\dot{Q}_1$ through RTD$^{(1)}$, the dissipated heat $\dot{Q}_2$ through RTD$^{(2)}$, and the heat loss through RTDs for a fixed $\lambda_{TE}^{sim} = 54\,\mathrm{W\,m^{-1}\,K^{-1}}$.

P	RTDs thickness (nm)	$\dot{Q}_1$ (W)	$\dot{Q}_2$ (W)	heat loss (%)
11×10^{-4}	300	2.48×10^{-5}	1.58×10^{-5}	7
8×10^{-4}	400	2.40×10^{-5}	1.57×10^{-5}	10
6×10^{-4}	500	2.22×10^{-5}	1.42×10^{-5}	12
5×10^{-4}	600	2.12×10^{-5}	1.36×10^{-5}	14
4×10^{-4}	700	2.00×10^{-5}	1.28×10^{-5}	16

The results show that $\dot{Q}_1$ and $\dot{Q}_2$ of each thickness are by a factor of 10 smaller than $P/2$. The generated P through the heating stripe decreases by increasing the thickness of the heating stripe. Consequently, the heat loss increases by increasing the RTDs thickness which is as a result of parasitic heat losses through RTDs contacts. From fabrication point of view, the thickness of RTDs and the heating stripe should be chosen in a way that they survive after removing the Cr/Au seed layer in the backside etching process. Considering a 10 nm Cr and 150 nm Au as adhesion and conductive seed layer for the ECD, the contacts thickness must be at least two times thicker to assure the free standing contacts after the backside etching. Therefore, in the fabrication of the transport device, a thickness of 400 nm Pt was considered for RTDs contacts.

To study the range of TE materials and film thicknesses that can be characterized using the developed transport device, simulations with different thermal conductivities and thicknesses of the TE material were performed. These simulations provided possibility to investigate the accuracy of the measurement results. First, the influence of different simulated thermal conductivities λ_{TE}^{sim} ranging from $2\,\mathrm{W\,m^{-1}\,K^{-1}}$ to $80\,\mathrm{W\,m^{-1}\,K^{-1}}$ was studied considering a constant thickness d of 6 µm for the TE material. The simulated ΔT depending on the position x at the bottom (solid lines) as well as top (dashed lines) of the TE material for 10, 20 and 40 $\lambda_{TE}^{sim}\mathrm{W\,m^{-1}\,K^{-1}}$ is shown in Fig. 5.2 (a). λ_{TE} of the TE material was then calculated using:

$$\lambda_{TE} = \frac{PL}{2A\Delta T(x=0)}, \tag{5.1}$$

where P is the experimental value of the heating power, $P = I_h V = 6 \times 10^{-4}\,\mathrm{W}$ (V dropped voltage in the heating stripe) and $\Delta T(x=0)$ is obtained through a linear fit to the simulated temperatures at the position of RTD$^{(1)}$, RTD$^{(2)}$ and the heat sink (dotted

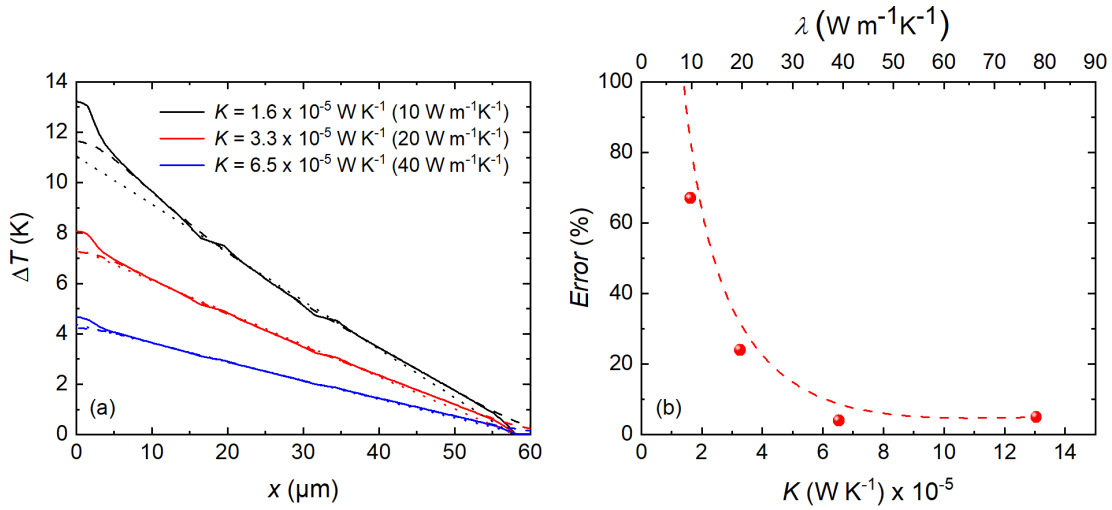

Figure 5.2.: (a) ΔT along the sample (x-direction) starting at the position of the heating stripe (x=0) up to the heat sink at the position (x=L) for different λ_{TE}^{sim} of $10\,\mathrm{W\,m^{-1}\,K^{-1}}$, $20\,\mathrm{W\,m^{-1}\,K^{-1}}$ and $40\,\mathrm{W\,m^{-1}\,K^{-1}}$. The solid lines show ΔT at the bottom of the TE material, the dashed lines show ΔT at the top of the TE material and the dotted lines show the linearized of ΔT, (b) the deviation between λ_{TE}^{sim} and the calculated λ_{TE} as a result of parasitic heat loss for a fixed d of 6 µm.

lines in Fig. 5.2(a)). L and $A = d \times b$ denotes the length and cross section of the TE material, respectively. Table 5.3 shows a summary of λ_{TE}^{sim}, the thermal conductance $K = \lambda_{TE}^{sim} A L^{-1}$, $\Delta T(x = 0)$, the calculated λ_{TE} and the deviation between λ_{TE}^{sim} and the calculated λ_{TE} for a fixed d of 6 µm.

The results indicate that the measurement error exceeds 24 % for a λ_{TE}^{sim} below $20\,\mathrm{W\,m^{-1}\,K^{-1}}$ which is a consequence of parasitic heat losses through the contacts or the heating stripe. Fig. 5.2 (b) shows the measurement error depending on K and λ_{TE}. Looking at Table 5.3 and Fig. 5.2, it can be seen that K has to exceed $5 \times 10^{-5}\ \mathrm{W\,K^{-1}}$ to stay within a measurement error of 10 %, this correlates with a λ_{TE}^{sim} of $30\,\mathrm{W\,m^{-1}\,K^{-1}}$. That is to say for a d of 6 µm, the applicability of the transport device is for TE materials with $\lambda d > 1.8 \times 10^{-4}\,\mathrm{W\,K^{-1}}$.

Beside of parasitic heat losses through RTDs along the material, there is another measurement error caused by the heat flow in z-direction. As discussed in section 5.1, $\Delta T(x)$ at the bottom and top of the sample match each other except for a small deviation from the linear behavior at $x = 0$. The linearity behavior is not any more valid when $\Delta T(x)$ at the bottom and top of the sample deviate from each other. For this reason, the influence of different TE material thicknesses d on the accuracy of the measurement was studied.

Table 5.3.: Influence of the thermal conductivity in simulation λ_{TE}^{sim}, the calculated thermal conductance K, the temperature increase $\Delta T(x = 0)$, the calculated λ_{TE} and the measurement error for a fixed TE thickness of 6 µm.

λ_{TE}^{sim} ($\mathrm{W\,m^{-1}\,K^{-1}}$)	K ($\mathrm{W\,K^{-1}}$)	ΔT (K)	λ_{TE} ($\mathrm{W\,m^{-1}\,K^{-1}}$)	Error (%)
2	3.3×10^{-6}	15.7	11.7	475
5	8.3×10^{-6}	14.2	12.9	158
10	1.6×10^{-5}	11.1	16.7	67
20	3.3×10^{-5}	7.4	24.9	24
40	6.5×10^{-5}	4.4	41.8	4
80	1.3×10^{-4}	2.4	76.6	4

I considered a λ_{TE}^{sim} of $20\,\mathrm{W\,m^{-1}\,K^{-1}}$ which shows an error of 24 % according to the above calculation for fixed d of 6 µm. λ_{TE} was calculated according to the Eq. 5.1 from simulations with different d ranging from 4 µm to 18 µm. $\Delta T(x = 0)$ is defined through a linear fit to the simulated temperatures in the similar way to the above procedure (dotted lines in Fig. 5.3 (a)) and P is the experimental value of the heating power, $P = 6 \times 10^{-4}\,\mathrm{W}$. Table 5.4 presents d of the TE material, the calculated K, $\Delta T(x = 0)$, the calculated λ_{TE}, and the measurement error defined as the deviation between λ_{TE}^{sim} and the calculated λ_{TE} for a fixed λ_{TE}^{sim} of $20\,\mathrm{W\,m^{-1}\,K^{-1}}$.

Table 5.4.: Summary of the applied TE thickness d in simulation, the calculated thermal conductance K, the temperature increase $\Delta T(x = 0)$, the calculated λ_{TE} and the measurement error for a fixed λ_{TE}^{sim} of $20\,\mathrm{W\,m^{-1}\,K^{-1}}$.

d µm	K ($\mathrm{W\,K^{-1}}$)	ΔT (K)	λ_{TE} ($\mathrm{W\,m^{-1}\,K^{-1}}$)	Error (%)
4	2.21×10^{-5}	9.16	29.7	48
6	3.31×10^{-5}	7.4	24.9	24
8	4.41×10^{-5}	6.01	22.6	13
10	5.52×10^{-5}	5.16	21.1	5
12	6.62×10^{-5}	4.55	19.9	0.4
16	8.83×10^{-5}	3.72	18.3	8
18	9.93×10^{-5}	3.44	17.6	12
30	16.6×10^{-5}	2.43	14.9	25

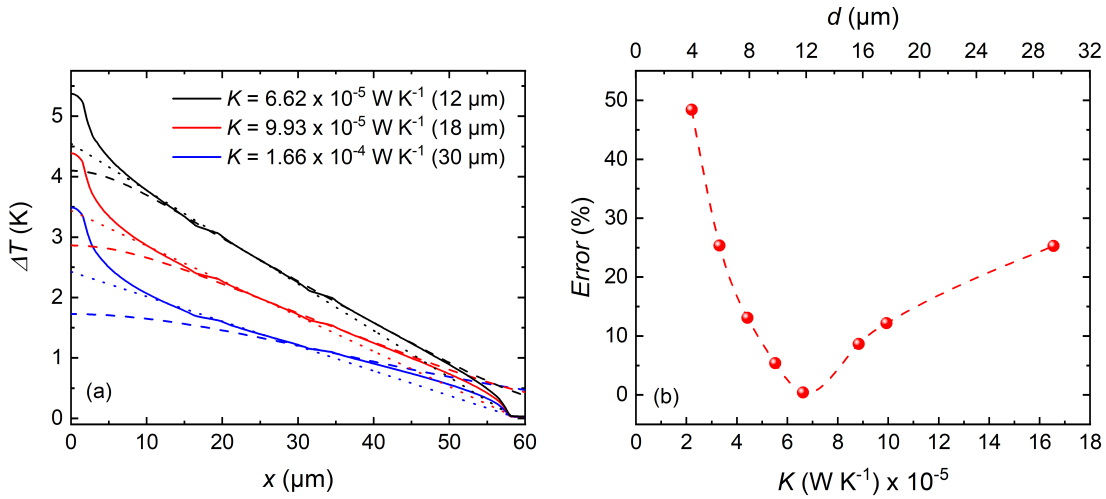

Figure 5.3.: (a) $\Delta T(x = 0)$ along the sample (x-direction) starting at the position of the heating stripe (x=0) up to the heat sink at the position (x=L) for different thicknesses of 12 µm, 18 µm and 30 µm. The solid and dashed lines show $\Delta T(x = 0)$ at the bottom and the top and of the sample. The dotted lines show the linearized $\Delta T(x = 0)$.

As discussed for different thermal conductivity measurements, to stay within an error of 10 %, K has to be higher than 5×10^{-5} W K^{-1} which corresponds in this case to thicknesses higher than 8 µm. On the other hand, the measurement error starts increasing from a thickness of 18 µm. This is due to the fact, that ΔT at the top and bottom of the TE material deviate from each other and the heat flow in z-direction is not negligible any more. That is to say that the simulated ΔT does not show a linear behavior and is not consistent with the 1D analytical appraoch. Hence $\Delta T(x = 0)$ in Eq. 5.1 can not be calculated through linearization to the simulated temperatures. Fig. 5.3 (a) represents the simulated ΔT along the x-direction at the bottom of the sample (solid line), at the top of the sample (dashed line) for different TE thicknesses of 12 µm, 18 µm and 30 µm. The dotted lines show the linearized of ΔT to the simulated temperatures at the position of RTD$^{(1)}$, RTD$^{(2)}$ and the heat sink. The measurement error depending on K and d for a λ_{TE}^{sim} of 20 W m^{-1} K^{-1} is shown in Fig. 5.3 (b).

5.3. Summary

Using 3D finite element simulations, the 1D analytical model for the thermal conductivity measurement was validated through study of the temperature distribution along the material. The simulated temperature distribution shows a linear behavior which is in a good agreement with the 1D analytical approach as well as with the experimental data achieved by the transport device.

Further, parasitic heat losses through the heating stripe and RTDs were studied using 3D simulations. The results show that the thickness of RTDs and the heating stripe affects the total heat losses dissipated through them. It was shown that the ratio of the total dissipated heat to the heat conducted through the material increases by increasing the thickness of RTDs. Moreover, from the fabrication point of view, the thickness of RTDs has to be at least two times thicker than the Au seed layer to guarantee the free standing contacts after removing the Au seed layer.

3D simulation provided possibilities to identify the range of thicknesses and thermal conductivities of TE materials which can be characterized within the developed transport device. That is to say, that the accuracy of the measurement with the transport device is highly dependent on the thermal conductance of TE materials. Considering a thickness of $6\,\mu m$, the thermal conductance of the TE material has to be higher than $5 \times 10^{-5}\,W\,K^{-1}$ to achieve a relative error less than $10\,\%$ which correlates with a thermal conductivity of $30\,W\,m^{-1}\,K^{-1}$. For TE materials with thermal conductivity less than $30\,W\,m^{-1}\,K^{-1}$, the decreasing of the thermal conductance can be compromised by increasing the thickness of the TE material. I showed that the accuracy of the measurement can be improved when the thickness of the TE material increases. The thickness of the TE material, however, has an influence on the heat flow in z-direction as well as on the linearity assumption of the temperature distribution along the material. Note, that the 1D steady state model for the thermal conductivity is valid as long as the temperature distribution along the material shows a linear behavior. Hence, the simulation supported to define the range of thickness of materials being characterized with the transport device taking the validity of the 1D steady state approach into account.

6. Thermoelectric Characterization using Transport Device

In this chapter, I show TE characterization of two electrochemically deposited TE thick films with the developed transport device which was presented in chapter 4. The outline of this chapter is as follows. First in section 6.1, the characterization of TE properties of $Co_{75}Ni_{25}$ thick film is presented within the fabricated transport device followed by a comparison with those obtained for a bulk sample. Section 6.2 is devoted to the temperature dependent properties of Sb thick film with the transport device. The morphology and chemical composition of the samples were studied using scanning electron microscopy (SEM), energy dispersive x-ray analysis (EDX) and X-Ray diffractometry (XRD) with a Bruker D8 Advance using a Co K_α radiation, a 0.4 mm Fe filter and 0.2 mm slit. Finally, I summarize and conclude the results in section 6.3.

6.1. N-Type CoNi

In this section, first the deposition of $Co_{75}Ni_{25}$ and its corresponding conditions are described which consist of the applied configuration setup, the bath solution and the applied potential. The temperature dependent characterizations within the transport device are then demonstrated in subsection 6.1.2.

6.1.1. Synthesis of CoNi Thick Film

Recently, there have been studies on electrochemically deposited nanowires of Co_xNi_{1-x} alloys based on the well known Watts type bath electrolytes containing different amount of Co^{2+} ions. The Watts baths were systematically developed by Vega *et al.* which have been successfully used to synthesize the Co-Ni alloy nanowires for different purposes such as magnetization behavior, mangeto-thermopower and magnetoresistance [71]. In this work, a cobalt nickel alloy with a composition of 75 % Co and 25 % Ni was electrochemically

deposited on the pre-structured transport device based on the above bath. The mentioned composition was desirable due to its high TE power factor ($PF > 4\,\mathrm{mW\,m^{-1}\,K^{-2}}$) and its excellent reproducibility of the electrochemical deposition, well established by a variety of different available deposition parameters [70, 71, 74].

The used Watts-type bath consists of $0.18\,\mathrm{mol\,l^{-1}}$ $CoSO_4$ (Fluka chemika, 99 %), $0.02\,\mathrm{mol\,l^{-1}}$ $CoCl_2$ (Fluka chemika, 98 %), $0.95\,\mathrm{mol\,l^{-1}}$ $NiSO_4$ (Merck, 98 %), $0.16\,\mathrm{mol\,l^{-1}}$ $NiCl_2$ (Merck, 98 %), $0.73\,\mathrm{mol\,l^{-1}}$ H_3BO_3 (99.8 %) and $0.5\,\mathrm{mol\,l^{-1}}$ NaOH to adjusted the pH-value to $4 - 4.2$ [71]. The ECD was carried out under potentiostatic method in a three-electrode configuration setup with Pt being the counter electrode and Ag/AgCl as reference electrode (see Fig. 3.6 in subsection 3.2.3) using a BioLogic VSP modular 5 channels potentiostat/galvanostat. In order to control the edge effect and the thickness of the deposited material, a pulsed mode was used with a deposition potential of $E_{\mathrm{on}} = -1\,\mathrm{V}$ applied for $t_{\mathrm{on}} = 0.25\,\mathrm{s}$, followed by a relaxing time of $t_{\mathrm{off}} = 2\,\mathrm{s}$ at an off potential of $E_{\mathrm{off}} = 0\,\mathrm{V}$.

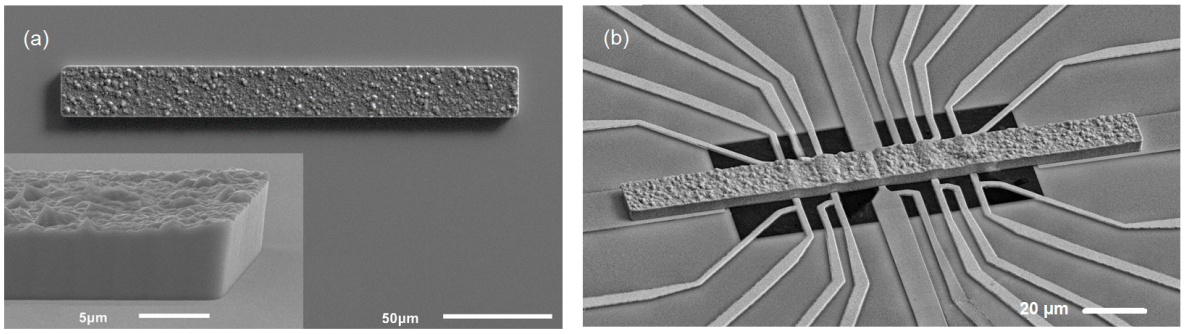

Figure 6.1.: (a) an SEM image of a micro-cavity with an inset of its corner, (b) an SEM image of the transport device showing the deposition onto the micro-cavity.

The deposition was first performed on a Si-substrate coated with 10 nm Cr and 150 nm Au as adhesion and conductive seed layer which contains an array of micro-cavities. These micro-cavities have the same size to the one on the pre-structured transport device and were patterned through photolithography and micro-structuring. This especially helped to define the range of composition and thickness which can be obtained with the applied deposition parameters. As discussed in subsection 3.1.1, the AZ9260 photoresist was applied which shows good compatibility with the ECD method and provides the desired thickness for the thick film deposition. The above mentioned deposition parameters resulted in a $Co_{75}Ni_{25}$ thick film with a thickness of 6 µm which was measured with a profilometer (Bruker Dektak). It is worth to mention, that the major focus of the deposition was on the achieving of the right thickness and composition as well as a significant compact thick film. This particularly provided the requirements for full in-plane characterization within the transport device. Fig. 6.1 shows SEM images of the $Co_{75}Ni_{25}$ thick

film on the micro-cavity (a) with an inset of its corner as well as the deposition on the pre-structure transport device (b).

6.1.2. Thermoelectric Properties of CoNi

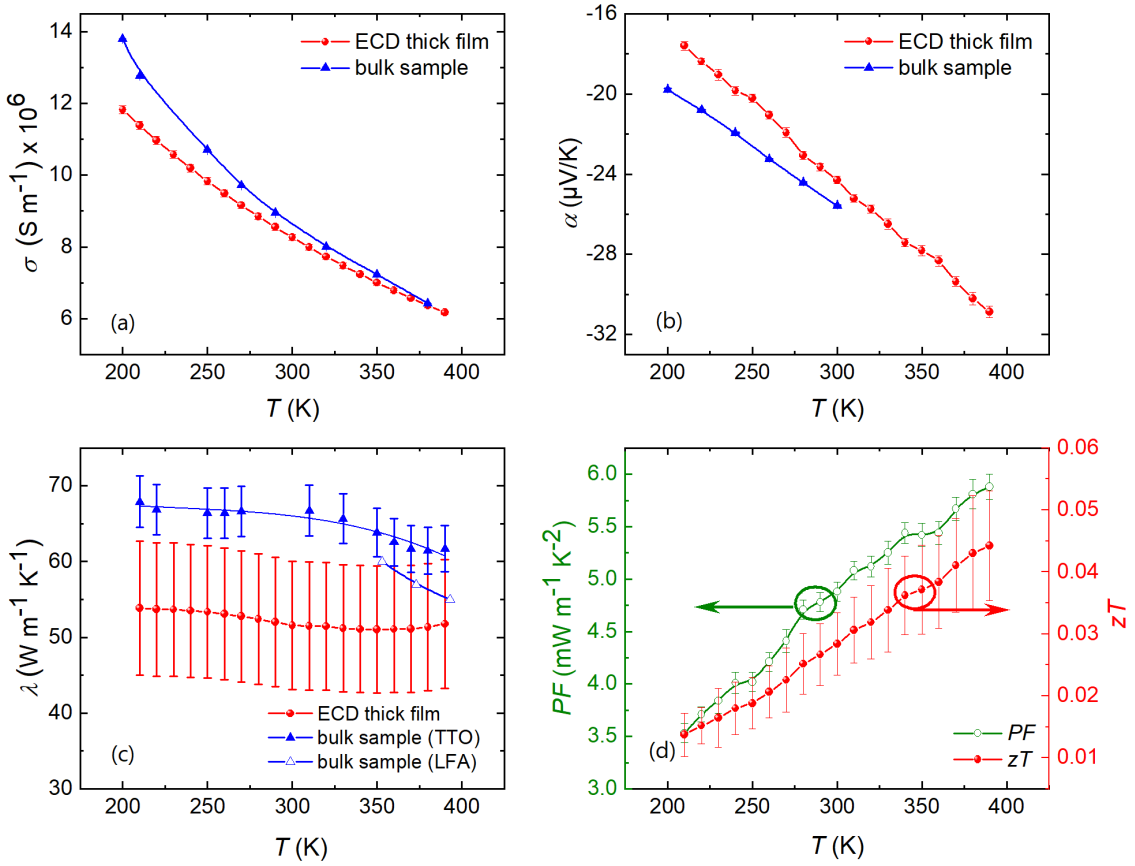

Figure 6.2.: a) σ b) α of the thick film measured with the transport device and the bulk sample measured with TTO, c) λ of the thick film measured with the transport device in comparison with the bulk sample measured with TTO as well as LFA and d) calculated zT and PF of the thick film in terms of temperature.

In this section, the temperature dependent properties of the electrochemically deposited $Co_{75}Ni_{25}$ thick film within the transport device are shown and discussed. The characterization included the in-plane σ, α and λ which were measured in a temperature range of 200-400 K. As discussed in section 3.4, the measurements were performed using external

DC sourcemeters and nanovoltmeters. Furthermore, the characterizations of the thick film within the transport device were compared with those obtained for the arc-molten bulk sample (see subsection 3.3.1 for bulk sample preparation). The arc molten bulk reference sample was measured with TTO in the Dynacool device and LFA from Linseis (see section 3.4).

Fig. 6.2 represents the temperature dependent properties of the $Co_{75}Ni_{25}$ thick film measured with the transport device and an arc molten bulk sample with the same composition measured by TTO and LFA. It is worth noting that the measurement error bars shown in Fig. 6.2 are the results of the standard deviation of the measured properties and its error propagation in the applied equations.

The value of σ at room temperature for the thick film and the arc molten bulk sample is $8.27 \times 10^6\,\mathrm{S\,m^{-1}}$ and $8.56 \times 10^6\,\mathrm{S\,m^{-1}}$, respectively. This shows that σ of the thick film measured within the developed transport device is close to that of the arc molten reference sample except for a small deviation at lower temperatures (See Fig. 6.2 a). The temperature dependent α of the $Co_{75}Ni_{25}$ thick film as well as the arc molten bulk sample was shown in Fig. 6.2 (b). α of the thick film and the bulk sample is negative which indicates an n-type TE material. The electrochemically deposited $Co_{75}Ni_{25}$ thick film shows a slightly smaller α as to that obtained with arc molten bulk sample.

Fig. 6.2 (c) shows the temperature dependent λ of the $Co_{75}Ni_{25}$ thick film as well as the arc molten bulk sample. The arc molten bulk sample has a larger λ than that of the thick film in the temperature range of 200-400 K. Transport properties of matter can be affected through a number of factors such as grain size, porosity and impurities. As opposed to the bulk sample, the electrochemically deposited $Co_{75}Ni_{25}$ thick film shows a stronger disorder within the grains and at the grain boundaries. This results in a more scattering at the defects and boundaries which consequently reduces the mean free path of electrons and phonons. λ, in principle, comprises contributions of electrons λ_e and phonons λ_l. As opposed to pure metal, where λ is mostly dominated by λ_e and λ_l is insignificant, electrons in metallic alloys are strongly scattered by solute atoms. This causes reducing the ability of electrons to carry heat and current [44].

If the experimental λ is assumed to be λ_e, L_0 can then be calculated through the Wiedemann-Franz relation (see Eq. 2.39) which is $2.14 \times 10^{-8}\mathrm{W\Omega K^{-2}}$ at room temperature. This value is close to $2.19 \times 10^{-8}\,\mathrm{W\,\Omega\,K^{-2}}$ for bulk Ni and $1.98 \times 10^{-8}\,\mathrm{W\,\Omega\,K^{-2}}$ for bulk Co [44]. Fig. 6.2 (d) shows the calculated PF and zT of the electrochemically deposited $Co_{75}Ni_{25}$ thick film in a temperature range of 200-400 K. At room temperature, the thick film has a PF of $4.8\,\mathrm{mW\,m^{-1}\,K^{-2}}$ which is close to that of the bulk sample of $PF = 5.6\,\mathrm{mW\,m^{-1}\,K^{-2}}$. zT value of the electrochemically deposited $Co_{75}Ni_{25}$ thick film remains quite low due to its relative large λ. zT of the $Co_{75}Ni_{25}$ thick film at room temperature is 0.028 which is comparable to the bulk value of 0.024.

6.2. P-Type Sb

In this section, first the deposition of Sb thick film using ECD technique and its corresponding conditions are described in subsection 6.2.1 which consist of the applied configuration setup, the bath solution and the applied current density. Then, the temperature dependent characterizations within the transport device are explained in subsection 6.2.2 and compared with those for reference samples (see subsection 3.3.2 for preparation of reference samples). This section was studied in collaborations with two colleagues Lennart Wilkens in the course of his Diploma and Alejandra Ruiz de Clavijo in the course of her internship in IFW Institute.

6.2.1. Synthesis of Sb Thick Film

To identify the applied potential and current for the deposition of Sb thick film on the prestructure transport device, special requirements need to be met. The deposition process was first started with a cyclic voltammetry (CV) on a continuous Si substrate which was coated with Cr/Au as adhesion and seed layer. Then, the deposition process was scaled down to micro-cavities produced by photolithography and micro-structuring. To synthesize the Sb thick film, the well known bath electrolyte was used which consists of $0.3\,\mathrm{mol\,l^{-1}}$ $SbCl_3$ (Sigma-Aldrich, 99 %), $1.6\,\mathrm{mol\,l^{-1}}$ H_2SO_4 (Merck, 97 %) and $1.7\,\mathrm{mol\,l^{-1}}$ HCl (Merck, 37 %) as proposed by Kozlov *et al.* [124]. This highly acidic electrolyte enables the reduction of Sb^{3+} species to Sb^0 and avoids the hydrolysis of $SbCl_3$ in the aqueous solution which follows this reaction

$$SbCl_3 + H_2O \rightarrow SbOCl + 2HCl. \tag{6.1}$$

As a further treatment to avoid the hydrolysis of $SbCl_3$, the sample had to be washed in concentrated HCl after ECD process. To study the reactions involved in the electrolyte as well as to identify the range of reduction potential of metallic Sb, a CV was performed on a Si substrate coated with 10 nm Cr and 150 nm Au as adhesion and conductive seed layer. The CV curve (see Fig. 6.3) was studied at a potential ranging from $-1.0\,\mathrm{V}$ to $1.0\,\mathrm{V}$ with a scanning rate of $10\,\mathrm{mV\,s^{-1}}$ at temperature of 323 K. The result shows that the reduction and oxidation of Sb^{3+} species occurs at a potential of $-0.48\,\mathrm{V}$ and $0.32\,\mathrm{V}$ respectively. The reduction potential corresponds to a current density of $-1.1 \times 10^{-4}\,\mathrm{A\,cm^{-2}}$ which is in a less negative region of the cathodic curve identified as Sb underpotential deposition (UPD) reported in Wang *et al.* [125, 126]. Metallic Sb films can be achieved under potentiostatic method in a potential range between $-0.48\,\mathrm{V}$ and $-0.8\,\mathrm{V}$ before hydrogen is involved due to the aqueous solution.

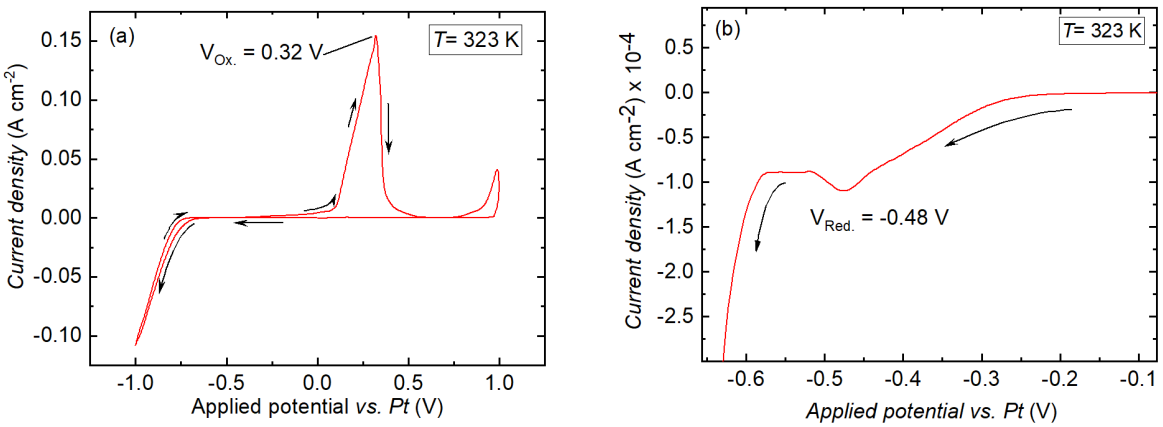

Figure 6.3.: a) Cyclic Voltammetry of Sb solution from -1 to 1 V at 323 K and b) Zoomed-in area around reduction peak of Sb^{3+}.

Considering these parameters obtained by CV curve, the ECD of Sb thick films were performed in a two electrodes cell configuration setup using a Pt net as both reference and counter electrode. A Si substrate was used as the working electrode which was coated with 10 nm Cr and 150 nm Au as adhesion and conductive seed layer. Hereby, the thickness and morphology of Sb thick films were studied before starting deposition on the cavity structured on the transport device. The depositions were performed on a Si substrate consisting of nine micro-cavities of $200 \times 20\,\mu m^2$ at temperature of 323 K under galvanostatic conditions with a current density of $0.022\,A\,cm^{-2}$ and an adjusted current of $-7.92\,\mu A$ which corresponds to a reduction potential of about $-0.8\,V$. These parameters resulted in a Sb thick film with a thickness of about 7 µm.

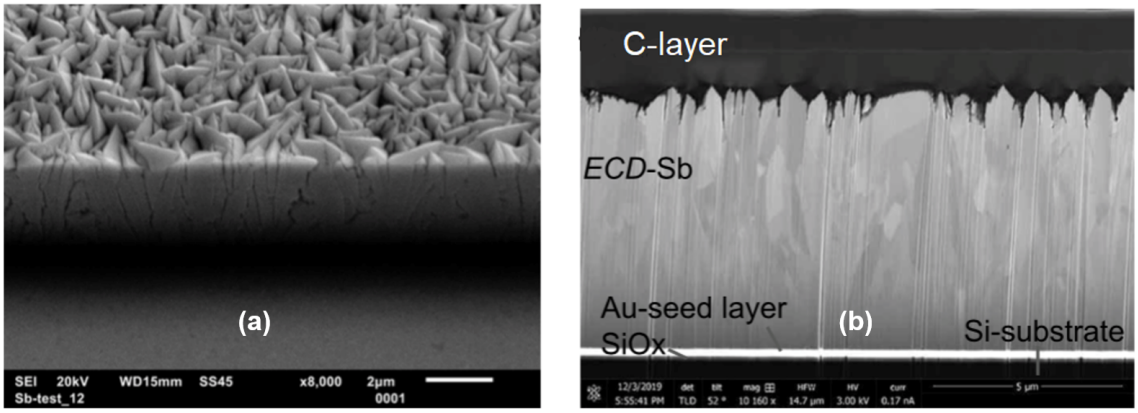

Figure 6.4.: (a) an SEM image of the texture of a micro-cavity and (b) an SEM image of the cross section of a micro-cavity showing the grain structure.

Fig. 6.4 (a) shows an SEM image angled view of the electrochemically deposited Sb thick film in a micro-cavity and Fig. 6.4 (b) presents an SEM image of the cross section of the micro-cavity showing the grain structure of the Sb deposition under galvanostatic conditions. It can be seen that Sb shows a columnar growth with a wide size distribution and a lamellar cross section, that is, one axis of the area is much longer that the perpendicular ones. The cross section view shows that there exist no voids or cracks within the deposited cavity and the grain size is about 1 to 2 µm in the long direction of the columns and about 500 nm in other directions.

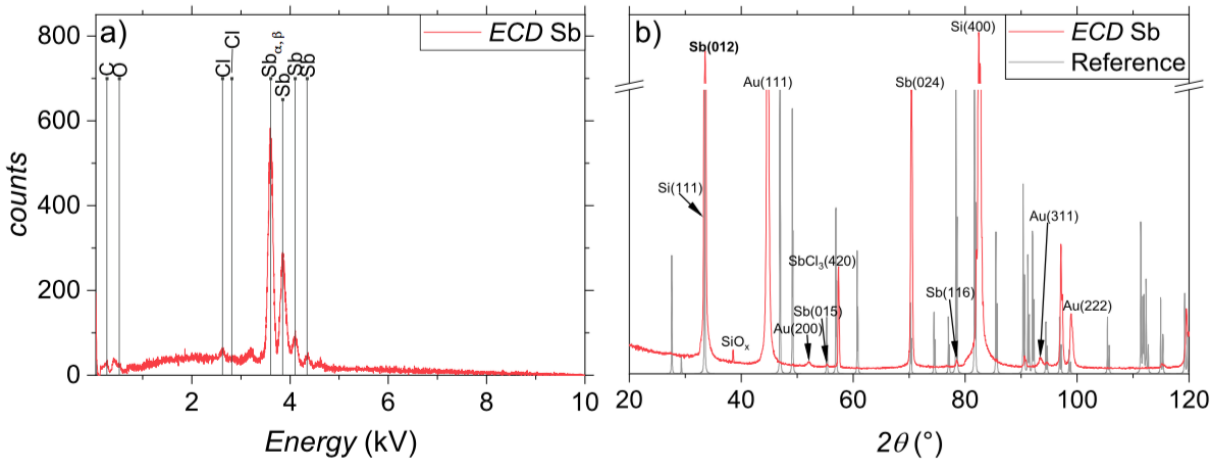

Figure 6.5.: (a) An EDX and (b) an XRD of the electrochemically deposited Sb continuous film (red) with a reference pattern of Sb.

The chemical composition of the Sb continuous film prepared under ECD technique was studied using EDX and XRD (see Fig. 6.5 (a) and (b)). The EDX shows the Sb peaks as well as slight contributions of O, C and Cl. The presence of C is more likely attributed to the preparation step for EDX measurement and are not considered as contamination of the film. The contribution of Cl stems from the precursor $SbCl_3$ in the electrolyte which can be exposed to the hydrolysis in the aqueous solution in spite of the washing treatment with HCl. By comparing the peak ratios, the content of Cl and Sb is $2.2 \pm 0.2\,\%$ and $97.8 \pm 2.2\,\%$, respectively. More details about the composition can be seen in the XRD of the Sb continuous film (Fig. 6.5 (b)) along with the Sb reference (card no. 00-005-0562). The XRD was analyzed using references of $SbCl_3$ (card no. 04-007-0865), $SbCl_5$ (card no. 04-010-5044), SbOCl (card no. 00-009-0117), Au (card no. 00-004-0784) and Si (card no. 00-005-0565). Among the Sb peaks, the presence of Cl in the film can be realized as a peak of $SbCl_3$ (420) next to the Sb peak. The influence of the substrate Si coated with a seed layer Au can be as well observed in the XRD.

6.2.2. Thermoelectric Properties of Sb

In this section, the temperature dependent σ and α of the electrochemically deposited Sb thick film performed within the transport device are presented and discussed. The characterization of the Sb thick film was performed in a Dynacool system in a temperature range of 200-400 K similar to the above mentioned procedure for $Co_{75}Ni_{25}$. In addition, the thick film characterizations were compared with those of a bulk sample and a thermally evaporated thin film. The bulk sample and the thin film sample measurements discussed in the following were done by my colleague, Lennart Wilkens, in the course of his Diploma thesis (see subsections 3.3.2 and 3.4.2 for the preparation of Sb reference samples and their characterization).

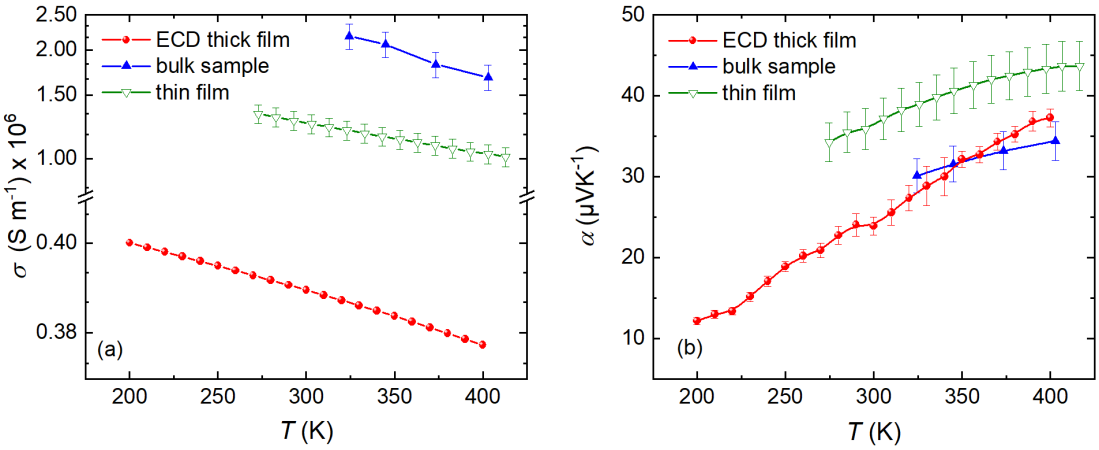

Figure 6.6.: a) σ and b) α of the electrochemically deposited Sb thick film, the thin film, and the bulk sample as a function of temperature.

Fig. 6.6 shows the temperature dependent σ and α of the thick film measured with the transport device, the bulk sample measured with LSR-3 and the thin film measured with TFA. The measurement error bars shown in Fig. 6.6 are the results of the standard deviation of the measured properties and its error propagation in the applied equations. The measured σ of these three samples declines with increasing the temperature which indicates a metallic behavior of Sb. The value of σ at room temperature for the thick film is about 0.39×10^6 and slightly decreases with temperature in a linear manner more similar to that of the thin film (see Fig. 6.6 a). σ of the bulk sample is larger than that of the thick and the thin film. This is because of the fact that σ is highly dependent on the grain size, i.e. the larger the grain size is, the higher σ is. However, σ of the thick film is considerably smaller than that of the thin film sample which may be assigned to the poor material quality produced by the ECD technique as well as the existing impurities such as $SbCl_3$ in the sample which act as electrically active scattering centers.

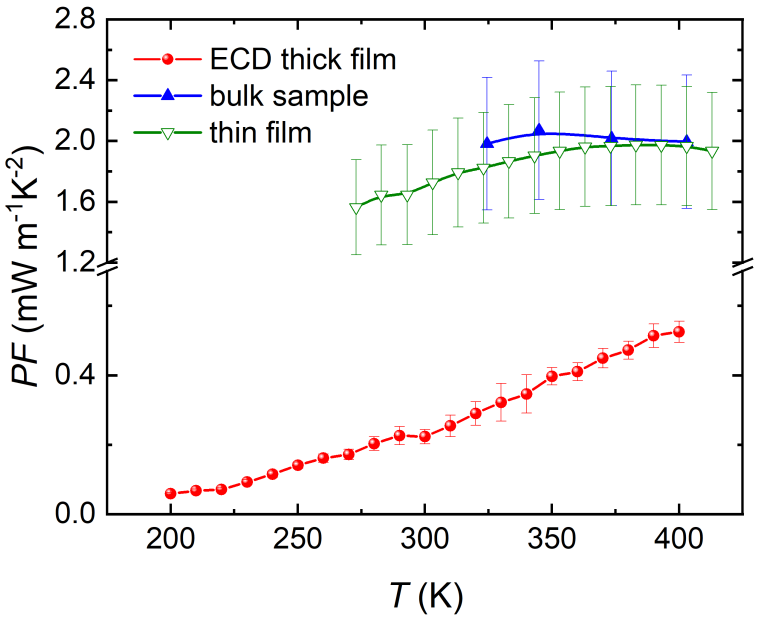

Figure 6.7.: Calculated PF of the electrochemically deposited Sb thick film in comparison with the Sb thin film and the bulk sample.

Fig. 6.6 (b) shows the temperature dependent α for the Sb thick film, the bulk sample and the thin film which indicates a positive α implying p-type conduction. It was already pointed out in chapter 2, for metals, α is dependent on temperature and decreases as temperature decreases. As opposed to σ, α is not strongly correlated with the grain size but is more related to the carrier concentration, mobility and effective mass. The electrochemically deposited Sb thick film shows a slightly higher α as to that obtained with the bulk sample. α of the thick film is, however, lower than that of the high purity thin film. The physical interpretation of α of the Sb thick film may be explained qualitatively by employing a two-band model taking two types of charge carriers p- and n-type into account. The lower α of the thick film may be attributed to the existence of $SbCl_3$ impurities which act as scattering centers resulting in a shift of p- and n-type contributions. Based on the two-band model, the overall Seebeck depends on the conductivity ratio σ_e/σ_h which is consequently a function of the charge carriers mobilities [127, 128]. The calculated carrier concentration of the electrochemically deposited thick film and the thin film remains almost unchanged ($n \approx 10^{20}$ cm^{-3}) while the carrier mobility decreases from $\mu \approx 220\,\mathrm{cm^3\,V^{-1}\,s}$ for the thin film to $\mu \approx 45\,\mathrm{cm^3\,V^{-1}\,s}$ for the thick film at the room temperature. The mobility and carrier concentration were calculated through Hall measurement. Hence, the decreased amount of the mobility as well as the existence of scattering centers together with the mixed conduction in the thick film may be caused the reduction of α compared to the thin film. At temperature about 320 K, the electrochemically deposited Sb thick film has a PF of $0.29\,\mathrm{mW\,m^{-1}\,K^{-2}}$ which is significantly smaller

than that of the bulk sample, $1.98\,\mathrm{mW\,m^{-1}\,K^{-2}}$, and the thin film, $1.82\,\mathrm{mW\,m^{-1}\,K^{-2}}$. This is due to the much smaller σ of the thick film in comparison with those of the bulk sample and the thin film (see Fig. 6.7).

6.3. Summary

Using the developed transport device and the defined characterization procedure, I characterized the temperature dependent transport properties of the electrochemically deposited $Co_{75}Ni_{25}$ and Sb thick films. Additionally, the synthesis of the both $Co_{75}Ni_{25}$ and Sb thick films along with the applied parameters for ECD technique were studied. To show and confirm the reliability of the transport device, the thick film measurements within the transport device were compared with those obtained for the reference samples. Despite the small size of the thick film, $Co_{75}Ni_{25}$, compared to the arc-molten bulk sample, the calculated PF and zT of the thick film are in a good agreement with the bulk sample which was measured with the commercial measurement system. This is a promising breakthrough for applications of the TE device, i.e. reducing the size of the device without loosing efficiency.

The temperature dependent σ and α of the electrochemically deposited Sb thick film measured with the transport device were compared with those of the reference samples, thin film and bulk sample. σ of the thick film measured with the transport device was much lower than that of the thin film and the bulk sample. This may be attributed to the low material quality of the ECD technique compared to the thermally evaporated thin film and the sintered bulk sample as well as the impurities like $SbCl_3$ present in the deposition. As opposed to σ, α of the thick film is close to that of the bulk sample and is lower than the high purity thin film. The behavior of α of the electrochemically deposited Sb thick film may be explained in the framework of a two-band model considering two types of charge carriers p-and n-type. The impurities like $SbCl_3$ in the thick film act as scattering centers and result in a mixed carrier conduction. The calculated carrier concentration of the thick film is almost the same as that of the thin film while the carriers mobility of the thick film is much lower than that of the thin film. Therefore, the Seebeck of the thick film decreases due to the decreased mobility as well as the existence of scattering centers. Hence, further developments and measurements need to be performed in order to improve the transport properties of the electrochemically deposited Sb. One of them is to achieve high material quality whilst reducing the existence of impurities like $SbCl_3$. The other one is to measure the thermal conductivity of Sb with the developed transport device which was not carried out in the scope of this work due to the lack of time.

7. Optimization of µTEG

There have been many numerical, mainly finite element simulations, and analytical studies focused on performance analysis of macro- and micro-TE devices some of which fabricated by electrochemically deposited techniques[7, 129–134]. However, less attention has been given to the effects of design and geometry factors on their performance. These effects especially can be realized in micro-fabrication processes where the material properties are deviated from their bulk values [7]. In this chapter, the geometry optimization of a micro-TE generator (µTEG) is presented using a finite element simulation considering realistic and optimized material properties and device dimension. It is demonstrated how the geometry variation has a significant impact on the performance of a µTEG.

This chapter is based on a jointly collaboration with my colleague David Alberto Lara Ramos, with the support of our other colleagues whose names have been listed as authors in [135]. For the simulations of a µTEC, I refer the reader to his PhD thesis [136]. In this chapter, however, I focus on the simulations of a µTEG starting from the conceptual approach for the optimization of µTEDs.

The outline of the chapter is as follows. First, in section 7.1, the properties of the applied TE materials along with their corresponding dimension are defined. Then, the impact of the geometry variation on the performance of the µTEC is discussed in section 7.2, including a specific focus on the fill factor of the µTEG. Finally, I summarize and conclude the results in section 7.3.

7.1. Simulation Approach

The governing equations of the heat power balance at the hot side $\dot{Q}_h$ and the cold side $\dot{Q}_c$ for one leg (Eq. 2.18 and Eq. 2.19) as well as one thermocouple (Eq. 2.40 and Eq. 2.41) of a TEG were introduced in more details in sections 2.1 and 2.4.

The simulations were performed using finite element Comsol Multiphysics based on the heat transfer and electric current modules. In the simulations, the electrical contact

resistance of $r_c = 5 \times 10^{-11}\,\Omega\,\mathrm{m}^{-2}$ was considered as reported in [129]. The thermal contact resistances at the interfaces were neglected. For the simulation of the µTEG, two boundary conditions were chosen dedicated to the temperature and the electrical impedance matching. The bottom of the substrate was kept at 300 K which acts as a heat sink while the temperature of the upper surface of the top contact was defined at a fixed temperature of 310 K. In the following, ΔT is defined as the temperature difference across the TE legs. The second boundary condition was defined by an electrical load resistance R_{load} with an equal value to the total resistance R of the µTEG.

Table 7.1.: Summary of the used parameters in the simulations of the µTEG including the material, the dimension of each component as well as its σ, α and λ. (a) Values taken from Comsol Multiphysics database. (b) Values taken from in house electrochemically deposited continuous films [135].

Material	Dimension $(\mu m)^3$	σ $(\mathrm{S\,cm^{-1}})$	α $(\mu\mathrm{V\,K^{-1}})$	λ $(\mathrm{W\,m^{-1}\,K^{-2}})$
Au	$30(40) \times 30 \times 1$	456 000 [a]	6.5 [a]	317 [a]
Ni	$80 \times 30 \times 8$	138 000 [a]	−15 [a]	150 [a]
Si	$90 \times 40 \times 500$	0	0	130 [a]
$Bi_2(Te_{1-x}Se_x)_3$	$30 \times 30 \times 20$	950 [b]	−55 [b]	1.2 [b]
$(Bi_{1-x}Sb_x)_2Te_3$	$40 \times 30 \times 20$	1800 [b]	55 [b]	1.1 [b]

The TE materials were considered the electrochemically deposited $Bi_2(Te_{1-x}Se_x)_3$ as n-type and $(Bi_{1-x}Sb_x)_2Te_3$ as p-type whose TE properties were measured from in house electrochemically deposited continuous films [135]. Table 7.1 shows a summary of the geometrical dimension as well as the TE properties, including σ, α and λ of each component in the µTEG. The proposed µTEG in the simulation consists of one pair with a typical *Π*- structure and an asymmetric design of p- and n-type. In the asymmetric design, p- and n-leg have different cross sections in order to fulfill the aspect ratio Eq. 2.53 discussed in section 2.4. The cross section area of n-type and p-type is $30 \times 40\,\mu m^2$ and $30 \times 30\,\mu m^2$, respectively. The dimension of the top contact material Ni, the bottom contact material Au for the p-type (n-type) leg and the Si substrate is shown in Table 7.1 for an interleg distance of 10 µm.

7.2. Results and Discussion

I start first with a short discussion about the systematic study for geometry optimization of a µTEC with a typical *Π*- structure presented in [135]. This study resulted in guidelines

for the geometrical optimization of µTEDs considering geometry variation of the TE elements, the metallic top and bottom contacts and the total area of the substrate.

As opposed to bulk TEDs, the thickness of metallic top and bottom contacts in µTEDs are comparable with the thickness of TE elements. Hence, a non-optimized design of metallic contacts may cause undesirable effects on the performance of µTEDs. This was studied in this paper [135] for a µTEC which shows that the total resistance of the device decreases by increasing the thickness of any top and bottom contacts which consequently results in an increase of cooling performance due to the reduction of $\dot{Q}_{Joule}$ heating in the device. The impact of the metallic top contacts was even found more considerable on the cooling performance because of the improved heat spreading at the top contacts. For a µTEC, the influence of the geometry variation of the TE elements, including their leg width, depth and height on the individual heat contribution in heat balance equations (Eq. 2.40 and Eq. 2.41) was studied. Fig. 7.1 shows exemplarily the influence of width variation of the TE legs on the individual heat contribution as well as on the behavior of the temperature difference and the coefficient of performance (COP) of a µTEC. The results show that both $\dot{Q}_{Joule}$ and $\dot{Q}_{Fourier}$ are geometry-dependent due to their relation to R and K while $\dot{Q}_{Peltier}$ does not vary with respect to the geometry (see section 2.4). It has been discussed that the minimum temperature at the cold side of the µTEC is achieved when $\dot{Q}_{Joule}$ and $\dot{Q}_{Fourier}$ are compensated mutually. These optimization guidelines can also be applied for a µTEG in order to study its performance while changing the design and construction factors.

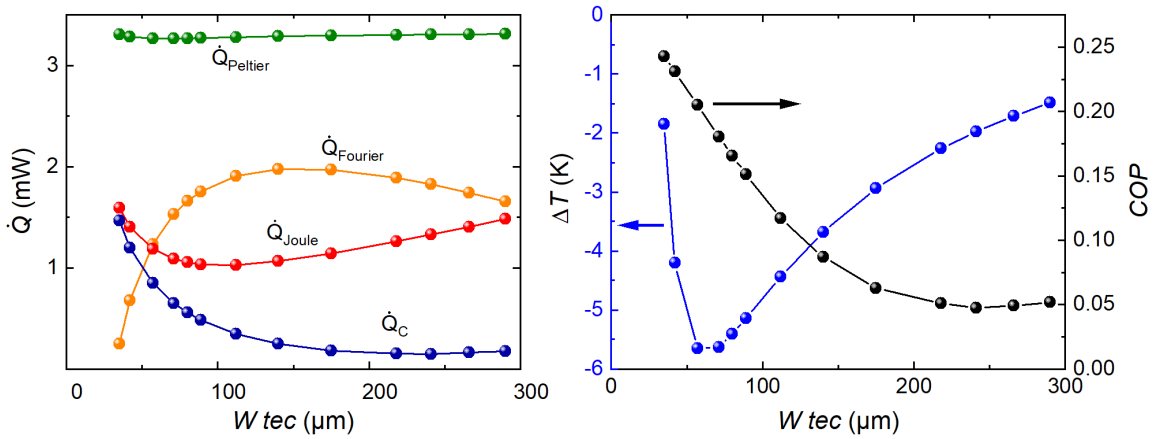

Figure 7.1.: (a) heat powers of $\dot{Q}_{Peltier}$, $\dot{Q}_{Fourier}$, $\dot{Q}_{Joule}$ and $\dot{Q}_c$ as a function of width of the TE legs (W tec) (b) the behavior of the temperature difference ΔT and the coefficient of performance (COP) as a function of W tec [135].

Here, the impact of the total area of the substrate on the performance of the µTEG is evaluated. Since the TED is connected to the heat sink and the heat source, the geometry

of both influences the heat powers in Eq. 2.40 and Eq. 2.41 which has to be taken into account. Hence, the impact of the substrate was studied on the performance of the µTEG under the effect of fill factor (FF) defined as the ratio of the cross sectional area of the active TE elements to the total substrate area. Fig. 7.2 shows, for example, the FF for two different configurations, 12 % and 58 % considering a TE leg height of 20 µm and a smallest accessible size of the heat sink. The larger the heat sink is, the more beneficial the fabrication of laboratory devices is, like a small device on a large Si substrate. However, in reality, the capacity of the heat sink in integrated devices is a main restriction.

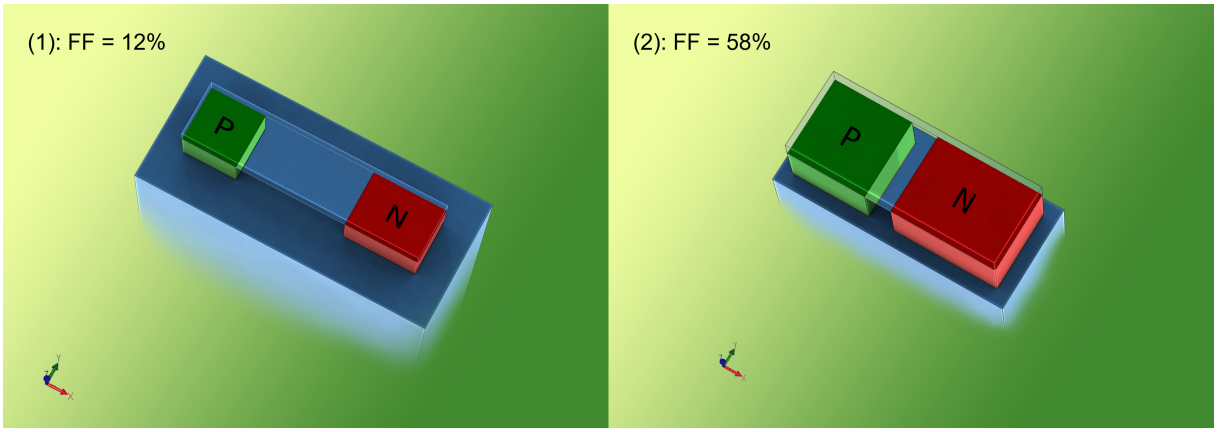

Figure 7.2.: Schematic picture of a µTEG consisting of one pair and a thickness of 20 µm for two fill factor values (1) 12 % and (2) 58 %.

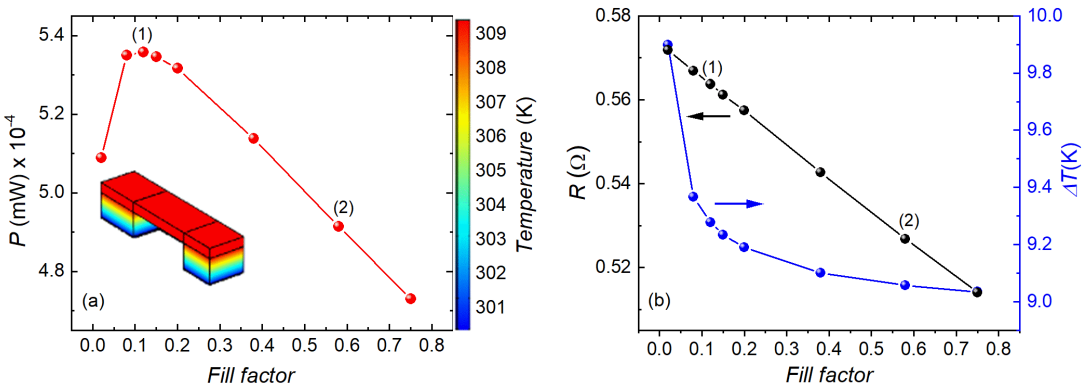

Figure 7.3.: (a) Calculated power output P in terms of fill factor for the µTEG (b) the achieved ΔT across the TE legs (blue) and the variation of the total resistance R of the device in terms of fill factor (black) for a TE leg height of 20 µm. The data point (1) and (2) corresponds to the fill factor of 12 % and 58 %, respectively.

The calculated power output P of the µTEG for different values of FF is shown in Fig. 7.3 (a). The results show that the power output reaches a maximum value at a FF of 0.12 which is much lower than that found for macroscopic devices. Because of the dependency of P on R as well as ΔT (see Eq. 2.47 in section 2.4), the impact of FF on ΔT and R was studied (see Fig. 7.3 (b)). Fig. 7.3 (b) shows that FF affects the achieved ΔT due to the finite thermal resistance of the device. That is to say that increasing FF limits the ability of the heat sink (substrate) to carry heat away from the device. Consequently, R decreases by increasing FF which is mainly assigned to the reduction of the interleg distance followed by the reduction of the top contact length. The behavior of these two main factors in P results in an optimum P.

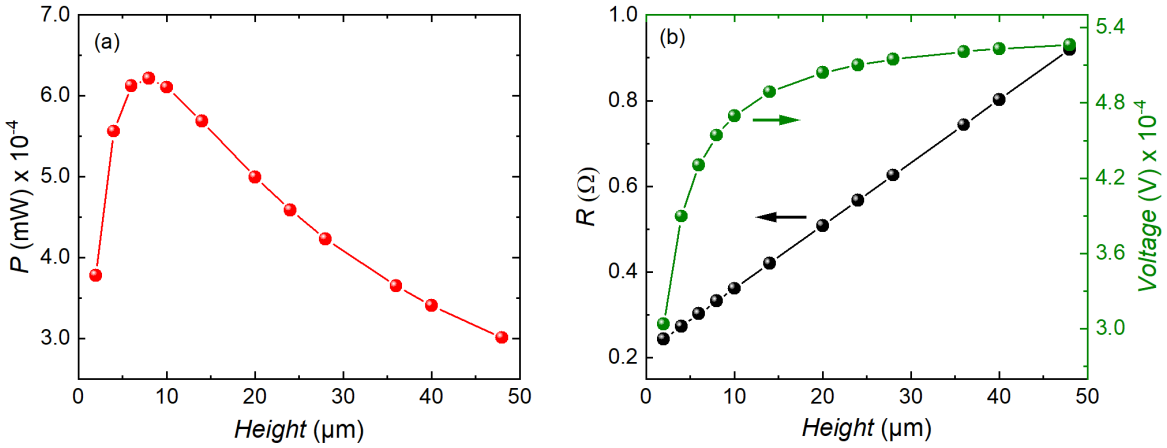

Figure 7.4.: (a) The calculated power output P in terms of TE leg height for a µTEG with a fill factor of 58 % (b) dependency of the total resistance R (black) and the electrical voltage (green) as a function of TE leg height for a fill factor of 58 %.

In the case of higher packing density and consequently larger FF for the fabrication of a µTEG, the height of the TE legs should be then decreased in order to obtain a larger P. This can be achieved when micro-fabrication process would allow to minimize the heat sink. Fig. 7.4 (a) and (b) show the dependency of P, R and the electrical output voltage V on the TE leg height for the µTEG with a FF of 58 %. R continues to increase linearly by increasing the height of the TE legs. V increases due to its dependency on ΔT as a function of the height and it slows when the maximum temperature difference reaches. The results show that P reaches a maximum value of 6.21×10^{-4} mW by increasing FF to 58 % as well as reducing the height of the TE legs to 8 µm.

7.3. Summary

This chapter was devoted to the effects of device geometry and design on the performance of µTEDs with a special focus on the packing density for a µTEG. Since the thickness of n-and p-type TE elements in micro-scaled TEDs are of comparable magnitude to that of metallic top and bottom contacts, using a design optimization is crucial to avoid any undesirable effects on the performance of µTEDs. The proper design of the metallic contacts increases the performance whilst decreasing losses due to the Joule heating. It was discussed that both the Joule heating and the Fourier heat conduction in the heat balance equations are geometry dependent while the Peltier heat contribution does not change with geometry variation. Hence, for a µTEC, the minimum cooling temperature can be achieved where a compromise between the Joule heating and the Fourier heat conduction is reached. The developed optimization strategies provide a framework for µTEDs achieving a best possible device performance. In this chapter, the impact of the fill factor was studied on the electrical power output and the device performance of a µTEG.

To study the effect of the fill factor, a finite element analysis was performed using Comsol Multiphysics based on the heat transfer and electric current modules. The results of the simulations for the µTEG show that the electrical power output changes as a function of the fill factor and the optimal value of the fill factor is much lower than that found for commercially macroscopic devices. The optimal value is a result of two main factors, namely the temperature difference across the TE legs and the total electrical resistance of the device. The temperature difference decreases by increasing the fill factor which is attributed to the finite thermal resistance of the substrate. This constrains the ability of the substrate to carry away heat from the device. The total electrical resistance decreases rapidly by increasing the fill factor because of the reduction of the interleg distance. A higher power output and smaller TE leg height (thickness) could be reached, this however acquires very challenging and accurate micro-fabrication steps and processes in order to increase the packing density.

8. Summary and Conclusion

In this thesis, a transport device was developed which provides the means to characterize thermoelectric (TE) thick films prepared by electrochemical deposition technique. In particular, two main subjects were thought out to develop this transport device. First, the characterization of electrochemically deposited TE thick films without the impact of the electrically conductive seed layer as well as the substrate. These layers carry severe consequences such as short circuit to the electrical field which makes TE characterizations of materials difficult to achieve. Second, the simultaneous characterization of the in-plane electrical conductivity, Seebeck coefficient and thermal conductivity on one single sample. To confirm the validity of the transport device, temperature dependent properties of two TE thick films were characterized. Here, I will briefly outline the results and conclusions regarding the development of the transport device along with its simulation analysis and thick film characterizations within the transport device.

A comprehensive micro-structuring was undertaken to design and fabricate the transport device namely photolithography, various deposition techniques and etching processes. The fabrication line was performed in three major parts: preparation of the Si_3N_4 membrane, patterning of the seed layer together with the resistance thermometers and finally the electrochemical deposition of the TE thick film accompanied by the backside etching processes. This configuration resulted in a suspended TE thick film on a free standing membrane enabling in-plane characterizations of TE thick films whilst removing the seed layer and the substrate.

The development was followed by a demonstration of the characterization procedure for the transport device which consists of the applied configuration setup and its boundary conditions dedicated to each TE parameter. Each individual parameter was measured using a number of resistance thermometers placed on the membrane of the transport device. It was shown that the electrical conductivity was measured using a four point probe configuration setup with two inner resistance thermometers for current while the voltage was measured through two outer thermometers. The configuration setup regarding the Seebeck measurement was defined using a partly passivated heating stripe on the center of the membrane together with two resistance thermometers.

For the thermal conductivity measurement, a 1D steady state model was developed within the transport device. It was discussed that the thermal conductivity was measured defining the temperature difference and the heating power dissipated along the sample when a current was passed through the heating stripe. According to the 1D analytical approach, the temperature distribution showed a linear behavior along the TE material.

The 1D analytical approach was validated using a 3D finite element Comsol simulation considering boundary conditions and materials properties devoted to the experimental setup. It was found that the temperature distribution along the material behaves linearly in a similar manner to the applied 1D analytical approach. The simulation results were found to be in a good agreement with the experimentally obtained data points confirming the validity of the transport device.

Using the simulation, I studied the accuracy of the measurements within the transport device and parasitic heat losses through the resistance thermometers. I showed how parasitic heat losses change as a function of the resistance thermometers thickness. The effect of the thickness on heat losses through the thermometers can be described as follows. By increasing the thickness of the resistance thermoemeters, the ratio of the total dissipated heat through thermometers to the heat conducted through the material increases. Moreover, from the fabrication point of view, the thickness of the thermometers has to be chosen in a way to ensure the free standing contacts after removing the seed layer. Therefore, the thickness of the thermometers has to be compromised between these two criteria. Additionally, the relationship between the accuracy of the measurement and the range of thicknesses as well as thermal conductances of the TE materials being characterized with this transport device was studied. Based on this analysis, guidelines were provided particularly for the choice of the thickness and thermal conductance of the TE materials in order to define the limitation of the applicability of the transport device.

To show the reliability of the transport device, the temperature dependent TE properties of $Co_{75}Ni_{25}$ as n-type and Sb as p-type TE thick films were successfully characterized and compared with those obtained for the reference samples. The reference samples were the arc-molten bulk sample for $Co_{75}Ni_{25}$, the spark plasma sintered bulk sample and the thermally evaporated thin film for Sb. The measured TE properties of the $Co_{75}Ni_{25}$ thick film were overall in a good agreement with those of the $Co_{75}Ni_{25}$ arc molten bulk sample. The recognized deviation in the transport behavior of the thick film and the bulk sample could be assigned to the differing micro-structure. Likewise, a comparison between the Sb thick film and the bulk sample as well as the thermally evaporated thin film revealed that the Seebeck coefficient of the thick film is close to that of the bulk sample and is lower than that of the high purity thin film. This behavior was explained based on a two-band model taking two types of charge carriers into account. The presence of the impurities like $SbCl_3$ as scattering centers as well as the lower carriers mobility of the thick film compared to that of the thin film result to a decrease in Seebeck. The electrical

conductivity of the electrochemically deposited Sb thick film is much less than those of the bulk sample and the thermally evaporated thin film. This may be attributed to the low material quality of the electrochemical deposition technique as well as the presence of the scattering centers.

In general, with the transport device presented in this thesis, it is possible to characterize materials in a wide range of temperature from liquid He up to several hundred degrees Celsius. Moreover, this device has the potential for magnetic field dependent characterizations which is of more interest in magneto-caloric and magneto thermopower measurements which are often not easily accessible. Because of the highly scalable and adjustable structure of the device, the other physical and chemical vapor deposition techniques can be as well applied.

The last section of this thesis was devoted to the development of the design guidelines for µTEDs prepared by electrochemically deposited materials. A study was performed using a Comsol simulation taking optimized material properties and device dimensions into account. It was discussed that the non-optimized design of the TE elements and their packing density on the substrate result in losses in the performance of µTEDs. In this thesis, the impact of the substrate and the packing density known as fill factor was specifically studied for a µTEG. The simulation summarized that the packing density affects the achieved temperature difference across the TE legs and the total resistance of the device. Increasing fill factor constrains the ability of the substrate to carry the heat away from the device. The total resistance decreases by increasing the fill factor due to the reduction of the interleg distance. As a result of the simulation, an optimized fill factor was found. The optimized value is however smaller than the typical value of the available macroscopic devices. Taken together, the presented geometry optimization provides inevitable guidelines for the fabrication of next generation of µTEDs with best possible device performance.

A. Supporting Material to chapter 4

The processing steps (a)-(i) of the transport device referring to Fig. 4.2 in section 4.2 along with the treatments and techniques used in this work are explained in this section [111].

(a) Patterning of photoresist (orange) on Si (gray) Si_3N_4 (blue) wafer: The first photolithography structuring was done on the backside of the sample (a 300 µm Si substrate with a 100 nm Si_3N_4 layer on both sides) to structure a cavity of $540 \times 460\,\mu m^2$ to etch Si_3N_4 and Si:

- Spin coating bilayer photoresist LOR 3B (3500 rpm/45 s), softback at 180 °C/250 s and MA-P 1205 (3500 rpm/30 s) and softback at 100 °C/30 s.
- Direct exposure with laser writer µPG 101 (Heidelberg Instruments), applied power 8 mW, power percentage 90 %, energy mode 1×1 and filter on.
- Developing in ma-D 331 for 30 s.

(b) Reactive ion etching (RIE) of Si_3N_4:

- Si_3N_4 etching by RIE (Sentech SI220) using 15 sccm O_2 and 45 sccm CHF_3, pressure 5 Pa and power 50 W for 6 min.
- Removing the photoresist using remover 1165.
- Cleaning the sample with Acetone and Isopropanol to remove the photoresist residual.

(c) KOH etching of Si:

- Sample was etched in a 40 % KOH solution at 80 °C for around 6 h (etching rate $\sim 50\,\mu m\,h^{-1}$).

(d) Deposition of Cr/Au seed layer (yellow):

- Spin coating bilayer photoresist LOR 3B (3500 rpm/45 s), softback at 180 °C/250 s and MA-P 1205 (3500 rpm/30 s) and softback at 100 °C/30 s.

- Direct exposure with laser writer µPG 101 (Heidelberg Instruments), applyed power 8 mW, power percentage 90 %, energy mode 1×1 and filter on.

- Developing in ma-D 331 for 30 s.

- Sputtering (Torr CRC622) of 10 nm Cr (15 sccm Ar, DC current of 50 mA, r $\sim$ 0.7 Å s^{-1}) and 150 nm Au (15 sccm Ar, RF power of 80 W, r $\sim$ 1.4 Å s^{-1}).

- Lift-off in 1165 remover at 50 °C.

(e) Patterning of the heating stripe (red) and RTDs

- Spin coating bilayer photoresist LOR 3B (3500 rpm/45 s), softback at 180 °C/250 s and MA-P 1205 (3500 rpm/30 s) and softback at 100 °C/30 s.

- Direct exposure with laser writer µPG 101 (Heidelberg Instruments), applied power 8 mW, power percentage 90 %, energy mode 1×1 and filter on.

- Developing in ma-D 331 for 30 s.

- Sputtering (Torr CRC622) of 10 nm Ti (15 sccm Ar, DC current of 50 mA, r $\sim$ 0.7 Å s^{-1}) and 400 nm Pt (15 sccm Ar, RF power of 80 W, r $\sim$ 1.2 Å s^{-1}).

- Lift-off in 1165 remover at 50 °C.

(f) SiO_2 passivation (light brown)

- Deposition of 50 nm SiO_2 by Atomic Layer Deposition (ALD) on the sample. The SiO_2 passivation layer was deposited in a commercially available GemStar XT-R thermal bench-top ALD system from Arradiance in stop-exposure mode with a temperature of the reactor chamber of 200 °C. 3-Aminopropyltriethoxysilane (*APTES*) was used as the reductant, whereas the combined subsequent use of H_2O and O_3 acted as oxidizer. The O_3 was provided by a BMT 803N ozone generator operated with pure oxygen. The metal organic precursor was heated to 100 °C to ensure a sufficient vapor pressure. The pulse time was 75 ms (50 ms, 50 ms), the exposure time 1 s (1 s, 4 s) and the pump time 20 s (4 s, 55 s) for *APTES* (H_2O, O_3). With these parameters 950 cycles resulted in 50 nm of SiO_2[111].

- Spin coating photoresist AZ 5214 (4500 rpm/40 s), softback at 90 °C/240 s.
- Direct exposure with laser writer µPG 101 (Heidelberg Instruments), applied power 6 mW, power percentage 100 %, energy mode 1 × 1 and filter on to structure the small section of heating stripe.
- Developing in AZ 726 MIF for 80 s.
- Removing the SiO_2 from RTDs, seed layer and contact pads by RIE using O_2 (pressure 5 Pa, gas flow 15 sccm) and CHF_3 (pressure 5 Pa, gas flow 45 sccm), applied power of 50 W for 5 min.
- Removing the photoresist using remover 1165.

(g) Electrochemical deposition of TE material (dark gray):

- Spin coating of 10 µm AZ 9260 (2400 rpm/60 s), softback at 110 °C/165 s.
- Direct exposure with laser writer µPG 101 (Heidelberg Instruments), applied power of 5 mW, power percentage 50 %, energy mode 1 × 2 and filter off to structure a cavity of $200 \times 20\ \mu m^2$ for electrochemical deposition of TE material.
- Developing in AZ 400 K developer diluted 1:3 in deionized water for 300 s.
- RIE using 25 sccm O_2 (50 W/1 min/3 Pa) to remove photoresist residual.
- Deposition of the TE material by electrochemical deposition technique in a two or three electrodes configuration cell (see section 6.1 and 6.2).
- Removing the photoresist using remover 1165.

(h) Backside etching of Si_3N_4:

- Spin coating of 10 µm AZ 9260 (2400 rpm/60 s), softback at 110 °C/165 s to protect the sample.
- RIE using O_2 (5 Pa/15 sccm) and CHF_3 (5 Pa/45 sccm), applied power of 50 W for 6 min to remove Si_3N_4 from backside of the transport device.

(i) Backside etching of Cr/Au:

- Removing of Cr/Au seed layer by wet chemical etching of Cr etchant (TechniEtch Cr01, etch rate $\sim 60\,\mathrm{nm\,min^{-1}}$) and Au etchant ($KI/I_2$ solution, etch rate $\sim 1\,\mu\mathrm{m\,min^{-1}}$).

- Removing the photoresist using remover 1165.

Bibliography

[1] H. J. Goldsmid, *Introcuction to Thermoelectricity* (Springer, 2010).

[2] R. He, G. Schierning, and K. Nielsch, Advanced Materials Technologies **3**, 1700256 (2018).

[3] D. M. Rowe and C. M. Bhandari, *modern thermoelectrics* (Holt-Technology, 1983).

[4] B. Sales, in *Encyclopedia of Materials: Science and Technology*, edited by K. H. J. Buschow *et al.* (Elsevier, 2001), pp. 9179–9185.

[5] G. Schierning *et al.*, Translational Materials Research **2**, 025001 (2015).

[6] A. Shakouri and Yan Zhang, IEEE Transactions on Components and Packaging Technologies **28**, 65 (2005).

[7] J. Garcia *et al.*, ECS Journal of Solid State Science and Technology **6**, N3022 (2017).

[8] C. Watkins, B. Shen, and R. Venkatasubramanian, ICT 2005. 24th International Conference on Thermoelectrics, 2005. 265 (2005).

[9] Y. Yang, X.-J. Wei, and J. Liu, Journal of Physics D: Applied Physics **40**, 5790 (2007).

[10] A. Lay-Ekuakille, G. Vendramin, A. Trotta, and G. Mazzotta, in *2009 IEEE International Workshop on Medical Measurements and Applications* (IEEE, 2009), pp. 1–4.

[11] G. Li *et al.*, Nature Electronics **1**, 555 (2018).

[12] N. Su *et al.*, Journal of Micromechanics and Microengineering **28**, 125002 (2018).

[13] J. P. Rojas *et al.*, ECS Journal of Solid State Science and Technology **6**, N3036 (2017).

[14] V. Leonov and R. J. M. Vullers, Journal of Renewable and Sustainable Energy **1**, 062701 (2009).

[15] S. J. Kim, J. H. We, and B. J. Cho, Energy & Environmental Science **7**, 1959 (2014).

[16] H. Bottner *et al.*, Journal of Microelectromechanical Systems **13**, 414 (2004).

[17] U. Birkholz, R. Fettig, and J. Rosenzweig, Sensors and Actuators **12**, 179 (1987).

[18] M. Kishi *et al.*, in *XVI ICT '97. Proceedings ICT'97. 16th International Conference on Thermoelectrics (Cat. No.97TH8291)* (IEEE, 1997), pp. 653–656.

[19] J.-P. Fleurial *et al.*, in *XVI ICT '97. Proceedings ICT'97. 16th International Conference on Thermoelectrics (Cat. No.97TH8291)* (IEEE, 1997), pp. 641–645.

[20] M. F. P. Wagner *et al.*, Physica status solidi (a) **213**, 610 (2016).

[21] F. Völklein, H. Reith, and A. Meier, physica status solidi (a) **210**, 106 (2013).

[22] V. Linseis *et al.*, Review of Scientific Instruments **89**, 015110 (2018).

[23] Zhixi Bian, Yan Zhang, H. Schmidt, and A. Shakouri, in *ICT 2005. 24th International Conference on Thermoelectrics, 2005.* (IEEE, 2005), Vol. 2005, pp. 76–78.

[24] R. Singh *et al.*, MRS Proceedings **886**, 0886 (2005).

[25] M. Muñoz Rojo *et al.*, International Journal of Thermal Sciences **89**, 193 (2015).

[26] H. Wendt and G. Kreysa, *Electrochemical Engineering* (Springer Berlin Heidelberg, 1999).

[27] J. Xie, C. Lee, M.-F. Wang, and J. M. Tsai, Microsystem Technologies **17**, 77 (2011).

[28] A. Sikora *et al.*, Review of Scientific Instruments **83**, 054902 (2012).

[29] V. Linseis *et al.*, physica status solidi (a) **215**, 1700930 (2018).

[30] F. Völklein, Thin Solid Films **188**, 27 (1990).

[31] C. Goupil, Journal of Applied Physics **106**, 104907 (2009).

[32] H. B. Callen, Physical Review **73**, 1349 (1948).

[33] A. Feldhoff, Energy Harvesting and Systems **2**, 5 (2015).

[34] C. Goupil *et al.*, Entropy **13**, 1481 (2011).

[35] G. J. Snyder and E. S. Toberer, Nature Materials **7**, 105 (2008).

[36] T. Tritt, *Encyclopedia of Materials: Science and Technology* (Elsevier, 2002), pp. 1–11.

[37] A. Bulusu and D. Walker, Superlattices and Microstructures **44**, 1 (2008).

[38] A. Polozine, S. Sirotinskaya, and L. Schaeffer, Materials Research **17**, 1260 (2014).

[39] T. M. Tritt, Annual Review of Materials Research **41**, 433 (2011).

[40] B. Karmakar, K. Rademann, and A. L. Stepanov, *Glass Nanocomposites* (Elsevier, 2016).

[41] M. Zebarjadi *et al.*, Energy Environ. Sci. **5**, 5147 (2012).

[42] L. D. Hicks and M. S. Dresselhaus, Physical Review B **47**, 12727 (1993).

[43] M. Jawaid, A. Ahmad, and D. Lokhat, *Graphene-Based Nanotechnologies for Energy and Environment* (Elsevier, 2019).

[44] T. M. Tritt, *Thermal Conductivity, Physics of Solids and Liquids* (Springer US, 2004).

[45] P. Liu and G. Chen, *Porous Materials* (Elsevier, 2014).

[46] H. Zhang, *Building Materials in Civil Engineering* (Woodhead Publishing, 2011).

[47] W. Kim, Journal of Materials Chemistry C **3**, 10336 (2015).

[48] G. A. Slack, *CRC Handbook of Thermoelectrics (ed. Rowe, M.)* (CRC Press, 1995), pp. 407–440.

[49] F. J. DiSalvo, Science **285**, 703 (1999).

[50] G. Fraisse, J. Ramousse, D. Sgorlon, and C. Goupil, Energy Conversion and Management **65**, 351 (2013).

[51] R. R. Heikes;, J. Roland W Ure, and S. J. Angello, *Thermoelectricity : science and engineering* (Interscience Publishers, 1961).

[52] H. J. Goldsmid and R. W. Douglas, British Journal of Applied Physics **5**, 386 (1954).

[53] M. S. Dresselhaus *et al.*, Advanced Materials **19**, 1043 (2007).

[54] B. Poudel *et al.*, Science **320**, 634 (2008).

[55] K. F. Hsu, Science **303**, 818 (2004).

[56] E. Skrabek and D. Trimmer, in *CRC Handbook of Thermoelectrics*, edited by D. Rowe (CRC, 1995), pp. 267–275.

[57] C. Uher, in *Recent Trends in Thermoelectric Materials Research I*, Vol. 69 of *Semiconductors and Semimetals*, edited by T. M. Tritt (Elsevier, 2001), pp. 139–253.

[58] G. S. Nolas, J. Poon, and M. Kanatzidis, MRS Bulletin **31**, 199 (2006).

[59] C. Wood, Reports on Progress in Physics **51**, 459 (1988).

[60] X. Yan *et al.*, Nano Letters **11**, 556 (2011).

[61] G. Joshi *et al.*, Advanced Energy Materials **1**, 643 (2011).

[62] A. F. Ioffe, *Semiconductor thermoelements and thermoelectric cooling* (Infosearch Ltd, 1957).

[63] M. Zebarjadi, Applied Physics Letters **106**, 203506 (2015).

[64] D. Vashaee *et al.*, Microscale Thermophysical Engineering **9**, 99 (2005).

[65] W. Seifert, V. Pluschke, and N. F. Hinsche, Journal of Physics: Condensed Matter **26**, 255803 (2014).

[66] M. Parker, Nature Electronics **2**, 211 (2019).

[67] M. Adams, M. Verosky, M. Zebarjadi, and J. Heremans, Physical Review Applied **11**, 054008 (2019).

[68] R. Ghodssi and P. Lin, *MEMS Materials and Processes Handbook*, Vol. 1 of *MEMS Reference Shelf* (Springer US, 2011).

[69] Y. Rheem, B.-Y. Yoo, W. P. Beyermann, and N. V. Myung, Nanotechnology **18**, 125204 (2007).

[70] J. García *et al.*, physica status solidi (a) **211**, 1041 (2014).

[71] V. Vega *et al.*, Nanotechnology **23**, 465709 (2012).

[72] P. Cojocaru, L. Magagnin, E. Gómez, and E. Vallés, Journal of Alloys and Compounds **503**, 454 (2010).

[73] M. Vazquez, *Magnetic Nano- and Microwires* (Elsevier, 2015).

[74] T. Böhnert *et al.*, Applied Physics Letters **103**, 092407 (2013).

[75] H. Bryngelsson *et al.*, Chemistry of Materials **19**, 1170 (2007).

[76] T. S. Arthur, N. Singh, and M. Matsui, Electrochemistry Communications **16**, 103 (2012).

[77] M. H. Yang and I. W. Sun, Journal of Applied Electrochemistry **33**, 1077 (2003).

[78] T. Manago, S. Ishida, H. Geka, and I. Shibasaki, Journal of the Vacuum Society of Japan **57**, 259 (2014).

[79] P. Fan *et al.*, Journal of Electronic Materials **44**, 630 (2015).

[80] G. E. Smith and R. Wolfe, Journal of Applied Physics **33**, 841 (1962).

[81] H. P. Nguyen *et al.*, Journal of the Electrochemical Society **160**, 75 (2013).

[82] Y. Zhang *et al.*, Advanced Materials **14**, 1227 (2002).

[83] J. Heremans *et al.*, Physical Review B **61**, 2921 (2000).

[84] D. Li *et al.*, Applied Physics Letters **83**, 2934 (2003).

[85] W. Ahmed and M. J. Jackson, *Emerging Nanotechnologies for Manufacturing* (Elsevier, 2015), pp. i–iii.

[86] J. De Boer and C. A. Van Blitterswijk, *Tissue Engineering* (Elsevier, 2015).

[87] S. Franssila and S. Tuomikoski, in *Handbook of Silicon Based MEMS Materials and Technologies*, *Micro and Nano Technologies*, edited by V. Lindroos, M. Tilli, A. Lehto, and T. Motooka (Elsevier, 2010), pp. 333–348.

[88] J. M. Quero, F. Perdigones, and C. Aracil, in *Smart Sensors and MEMs (Second Edition)*, *Woodhead Publishing Series in Electronic and Optical Materials*, second edi ed., edited by S. Nihtianov and A. Luque (Woodhead Publishing, 2018), pp. 291–311.

[89] K. Subramani and W. Ahmed, *Emerging Nanotechnologies in Dentistry* (Elsevier, 2012).

[90] S. M. Bhagyaraj, O. S. Oluwafemi, N. Kalarikkal, and S. Thomas, *Synthesis of Inorganic Nanomaterials* (Elsevier, 2018).

[91] B. S. Yilbas, A. Al-Sharafi, and H. Ali, *Self-Cleaning of Surfaces and Water Droplet Mobility* (Elsevier, 2019).

[92] R. K. Singh and R. Sharma, International Journal of Science and Research (IJSR) **2**, 135 (2013).

[93] J. P. Singh *et al.*, in *Advanced Applications in Manufacturing Enginering*, edited by M. Ram and J. P. Davim (Elsevier, 2019), pp. 53–77.

[94] R. Cirelli, G. Watson, and O. Nalamasu, in *Encyclopedia of Materials: Science and Technology*, edited by K. H. J. Buschow *et al.* (Elsevier, 2001), pp. 6441–6448.

[95] R. Jose Varghese *et al.*, in *Nanomaterials for Solar Cell Applications*, edited by S. Thomas *et al.* (Elsevier, 2019), pp. 75–95.

[96] X. J. Li and Y. Zhou, *Microfluidic devices for biomedical applications* (Woodhead Publishing, 2013), p. 684.

[97] M. Henini, Microelectronics Journal **31**, 219 (2000).

[98] K. O. Ukoba, A. C. Eloka-Eboka, and F. L. Inambao, Renewable and Sustainable Energy Reviews **82**, 2900 (2018).

[99] D. M. Mattox, *Handbook of Physical Vapor Deposition (PVD) Processing* (Elsevier, 2010).

[100] A. Boudrioua, M. Chakaroun, and A. Fischer, *Contemporary Physics* (ISTE Press - Elsevier, 2016), No. 4, pp. 423–424.

[101] J. X.J. Zhang and K. Hoshino, *Molecular Sensors and Nanodevices* (Elsevier, 2019).

[102] N.-T. Nguyen, *Micromixers* (Elsevier, 2012).

[103] P. M. Martin, *Handbook of Deposition Technologies for Films and Coatings* (Elsevier, 2010).

[104] M. Ohring, *Materials Science of Thin Films* (Elsevier, 2002).

[105] K. Seshan, *Handbook of thin-film deposition processes and techniques* (William Andrew, 2001).

[106] A. Tiwari, *Handbook of Antimicrobial Coatings* (Elsevier, 2018).

[107] A. Nakajima, Q. D. Khosru, T. Yoshimoto, and S. Yokoyama, Microelectronics Reliability **42**, 1823 (2002).

[108] J. Sheng *et al.*, Journal of Vacuum Science & Technology A **36**, 060801 (2018).

[109] K. Grigoras *et al.*, Journal of Physics: Conference Series **61**, 369 (2007).

[110] J. Bachmann *et al.*, Angewandte Chemie International Edition **47**, 6177 (2008).

[111] V. Barati *et al.*, Advanced Electronic Materials **6**, 1901288 (2020).

[112] R. Kohli and K. L. Mittal, *Developments in Surface Contamination and Cleaning* (Elsevier, 2015).

[113] U. Abidin, B. Y. Majlis, and J. Yunas, Jurnal Teknologi **74**, 137 (2015).

[114] G. Nageswaran, L. Jothi, and S. Jagannathan, in *Non-Thermal Plasma Technology for Polymeric Materials*, edited by S. Thomas *et al.* (Elsevier, 2019), pp. 95–127.

[115] A. Sarangan, in *Fundamentals and Applications of Nanophotonics*, edited by J. W. Haus (Elsevier, 2016), pp. 149–184.

[116] H. R. Luckarift, P. Atanassov, and G. R. Johnson, *Enzymatic Fuel Cells* (John Wiley & Sons, Inc., 2014).

[117] J. V. Macpherson, N. Simjee, and P. R. Unwin, Electrochimica Acta **47**, 29 (2001).

[118] S.-y. Tan, Ph.D. thesis, 2017.

[119] R. K. Franklin, Ph.D. thesis, Michigan, 2010.

[120] L. Wilkens, Diploma thesis, Dresden University of Technology, 2020.

[121] J. Martin, Journal of Research of the National Institute of Standards and Technology **117**, 168 (2012).

[122] S. Mortazavinatanzi, A. Rezaniakolaei, and L. Rosendahl, Sensors **18**, 989 (2018).

[123] Y. Tian *et al.*, Nano Lett **12**, 6492 (2012).

[124] V. M. Kozlov, V. Agrigento, G. Mussati, and L. Peraldo Bicelli, Journal of Alloys and Compounds **288**, 255 (1999).

[125] C. Wang, Y. Du, and Z. Zhou, Electroanalysis **14**, 849 (2002).

[126] F. Golgovici, A. Cojocaru, L. Anicai, and T. Visan, Materials Chemistry and Physics **126**, 700 (2011).

[127] T. C. Chasapis *et al.*, APL Materials **3**, 1 (2015).

[128] Z. M. Gibbs, H.-S. Kim, H. Wang, and G. J. Snyder, Applied Physics Letters **106**, 022112 (2015).

[129] R. Enright *et al.*, ECS Transactions **69**, 37 (2015).

[130] Y. Ezzahri *et al.*, Microelectronics Journal **39**, 981 (2008).

[131] M. T. Dunham *et al.*, Energy **93**, 2006 (2015).

[132] M. T. Dunham *et al.*, Advanced Materials Technologies **3**, 1700383 (2018).

[133] M. Gomez, R. Reid, B. Ohara, and H. Lee, Journal of Applied Physics **113**, 174908 (2013).

[134] R. Enright *et al.*, ECS Journal of Solid State Science and Technology **6**, N3103 (2017).

[135] D. A. Lara Ramos *et al.*, Advanced Sustainable Systems **3**, 1800093 (2019).

[136] D. A. Lara Ramos, Ph.D. thesis, Dresden University of Technology, 2020.

Vita

Vida Barati received her B.Sc and M.Sc degree in Physics from University of Isfahan in Iran. During her master at Isfahan university, she analyzed the thin film properties using WIEN2K simulation based on Density Functional Theory (DFT). In 2014 she started her second master study in Technical University of Braunschweig. She Joined Fraunhofer Institute for Surface Engineering and Thin Films IST in Braunschweig in the group „Highly Ionized Plasmas and PECVD“ for her master thesis. Her research focused on the electrical and optical characterization of technical plasma in sputter deposition techniques.

In 2017, she joined the Thermoelectric group of Dr. Gabi Schierning at the Leibniz Institute for Solid State and Materials Research (IFW) in Dresden as material scientist. Her research interests include the development and fabrication of micro-modules, material characterization and thermoelectric device modeling. In the course of her PhD at Dresden University of Technology, she has developed a transport device using micro-structuring fabrication to study the characterization of micro-scaled thermoelectric thick films which are prepared by electrochemical deposition technique.

Scientific Output

Publications

- **V. Barati**, J. Garcia, K. Geishendorf, L. Schnatmann, M. Lammel, A. Kunzmann, N. Pérez, G. Li, G. Schierning, K. Nielsch and H. Reith, *Thermoelectric Characterization Platform for Electrochemically Deposited Materials*, Advanced Electronic Materials. **6**, 1901288 (2020).

- D. Lara Ramos, **V. Barati**, J. Garcia, H. Reith, G. Li, N. Pérez, G. Schierning and K. Nielsch, *Design Guidelines for Micro-Thermoelectric Devices by Finite Element Analysis*, Advanced Sustainable Systems, **3**, 1800093 (2019).

- G. Li, J. Garcia, D. Lara Ramos, **V. Barati**, N. Pérez, I. Soldatov, H. Reith, G. Schierning and K. Nielsch, *Integrated Micro-Thermoelectric Coolers with Rapid Response Time and High Device Reliability*, Nature Electronics. **1**, 555-561 (2018).

Conferences

- **V. Barati**, J. Garcia, K. Geishendorf, L. Schnatmann, M. Lammel, A. Kunzmann, N. Pérez, G. Li, G. Schierning, K. Nielsch and H. Reith, *Development of a Full In-Plane zT-Characterization Platform for Electrodeposited Materials*, MRS 2019 Fall Meeting, Boston, USA (Oral presentation).

- **V. Barati**, J. Garcia, K. Geishendorf, L. Schnatmann, M. Lammel, A. Kunzmann, N. Pérez, G. Li, G. Schierning, K. Nielsch and H. Reith, *Thermoelectric Characterization Platform for Electrochemical Deposited Thick Films*, PowerMEMS 2019, Kraków, Poland (Oral presentation).

- G. Li, J. Garcia, D. Lara Ramos, **V. Barati**, N. Pérez, I. Soldatov, H. Reith, G. Schierning and K. Nielsch, *Integrated Micro-Thermoelectric Coolers with Free-Standing Design and Robust Device Performance*, MRS 2019 Spring Meeting, Boston, USA (Oral presentation).

- G. Li, J. Garcia, T. Sieger, L. Schnatmann, D. Lara Ramos, **V. Barati**, N. Pérez, H. Reith, G. Schierning and K. Nielsch, *Integrated Micro-Thermoelectric Coolers with Free-Standing Design and Robust Device Performance*, AIMES 2018, Cancun, Mexico (Oral presentation).

- **V. Barati**, J. Garcia, G. Li, H. Reith, G. Schierning and K. Nielsch, *Development of a Full In-plane ZT-Measurement Platform for Electrodeposited Materials*, MSE 2018, Darmstadt, Germany (Poster).

- D. Lara Ramos, **V. Barati**, G. Schierning, H. Reith and K. Nielsch, *Performance Simulation of Micro-Thermoelectric Coolers*, DPG 2018, Berlin, Germany (Oral presentation).

- **V. Barati**, H. Reith, G. Li, D. Lara Ramos, G. Schierning and K. Nielsch, *Multiphysics Simulation of Micro-Thermoelectric Generators Based on Power Factor Optimized Materials*, Comsol conference 2017, Rotterdam, Netherlands (Poster).